CHARACTERIZATION OF THE MECHANICAL BEHAVIOR OF A TWILL DUTCH WOVEN WIRE MESH

by

STEVEN M. KRAFT

A thesis submitted in partial fulfillment of the
requirements for the Honors in the Major Program in
Mechanical Engineering in the College of
Engineering and Computer Science and in The
Burnett Honors College at the University of Central
Florida
Orlando, Florida

Fall Term 2010

Thesis Chair: Dr. Ali P. Gordon

ABSTRACT

The mechanics of a woven wire mesh material are investigated to characterize the elasto-plastic behavior of this class of materials under tensile conditions. The study focuses on a representative 316L stainless steel (316L SS) 325x2300 twill-dutch woven wire mesh typically used as a fine filtration media in applications such as water reclamation, air filtration, and as a key component in swab wands used in conjunction with explosive trace detection (ETD) equipment. Mechanical experiments and a 3-D finite element model (FEM) are employed to study the macro-scale and meso-scale mechanical behavior of the woven wire mesh under uniaxial tensile conditions. A parametric study of the orientation dependence of the mechanical response of this material has been carried out, relating material properties such as elastic modulus, yield strength, etc. to material orientation. Ratcheting type tensile tests are also performed in a similar orientation study, and an elementary damage model is presented for the woven wire mesh based on continuum damage mechanics (CDM). The meso-scale behavior of the wire mesh is studied via the finite element method, and observations are made relating wire scale conditions to macro-scale material behavior.

ACKNOWLEDGEMENTS

I would like to sincerely thank Dr. Gordon for his motivation and guidance in the completion of this thesis. I would also like express thanks to the other committee members, Dr. Gou and Dr. Chen, for their time and help. Also, the members of the Mechanics of Materials Research Group are greatly appreciated for their assistance with this endeavor.

TABLE OF CONTENTS

Introduction……………………..…………………………………………………… 1

Literature Review ....……………………………... 2

The Woven Wire Mesh.......................................………………………. 4

Tensile Experiments...…………………………………………………………… 4

Single Wide Specimens.……………...7

Double Wide Specimens…………………………………………………9

Pre-conditioned Samples….……………………………………………...10

Tensile Behavior…………………………………………………………........ 11

AR Properties………………………………………………….……….. 11

Pre-processed Properties…..…………………….…..………………. 17

The Affect of Heat Treatment ……………………….……….…….…19

Homogenous Orthotropic Modeling…………..………………………………..23

Elastic Modeling……..…………………….……………………………… 24

Elasto-Plastic Modeling (Hill Analogy)…….……………………….…… 26

Voce Hardening Model…………………..……………………………...30

Fractographic Analysis..........……………………………………………… 33

Single Wide (AR)……………………………….………..………….. 33

Double Wide (AR)……………………...…………………………….. 37

Damage Modeling…….……………………………………………………….. 40

Ratcheting Experiments…………………………………………….… 40

Continuum Damage Model…………………………………………... 43

Numerical Modeling…………….……..………………………………...…..……. 47

Model Development……………………………………………………47

Boundary Conditions Main Axes………………………………….. 49

Boundary Conditions Off-axis……………………………………... 52

FEM Results Main Axes…………………………………………… 53

FEM Results Off-Axis……………………………………………….55

Plastic Strain Development………………………………………....59

Future Work……………………………………………………………………... 62

Conclusions……………………………………………………………………… 63

Appendix………..……………………………………………………………….. 65

References 149

LIST OF FIGURES

Figure 1.1
Schematic representation of 316L SS woven wire mesh 5

Figure 1.2
SEM images of 316L SS woven wire mesh 6

Figure 2.1
Time-lapse photography of CRE tensile test 7

Figure 2.2
Sketch of test specimen 8

Figure 3.1
Mechanical response of main axes of 316L SS woven wire mesh. 13

Figure 3.2
Orientation dependence of mechanical response of 316L woven wire mesh . . . 14

Figure 3.3
Main axes mechanical response of pre-processed 316L SS woven wire mesh . .18

Figure 3.4
Furnace setup used to heat treat specimens. 20

Figure 3.5
Effects of heat treatment on various 316L SS woven wire mesh specimens. . . . 21

Figure 4.1
Normalized elastic of woven mesh modulus with respect to orientation 24

Figure 4.2
Normalized yield strength of woven mesh with respect to orientation 28

Figure 4.3
Voce hardening model at various material orientations 31

Figure 5.1
Fracture surface images of single wide 316L SS woven wire mesh 34

Figure 5.2
Fracture surface images of double wide 316L SS woven wire mesh 39

Figure 6.1
Response of double wide samples subject to ratcheting tensile tests 41

Figure 6.2
Hysteresis loops of 316L SS woven wire mesh at various orientations 42

Figure 6.3
Elastic modulus evolution of double wide samples subject to ratcheting 44

Figure 6.4
Actual and correlated elastic modulus evolution of double wide samples. 46

Figure 7.1
MKIN Hardening models used to simulate hardening behavior of mesh wires . . 49

Figure 7.2
FEM mesh and boundary conditions used to simulate 316L SS woven mesh. . . .51

Figure 7.3
Off-axis mesh and boundary conditions. 52

Figure 7.4
Main axes load-displacement response of numerical model. 53

Figure 7.5
Main axes numerical stress-strain response (wires and macro-assumption). 55

Figure 7.6
Off-axis load-displacement response of numerical model. 56

Figure 7.7
Off-axis numerical stress-strain response (wires and macro-assumption). 58

Figure 7.8
Equivalent plastic strain contours of main axes. 60

LIST OF TABLES

Table 1.1
Material properties of 316L SS at room temperature. 6

Table 3.1
Normalized mechanical properties of SS 316L woven mesh in warp direction. . .12

Table 3.2
Orientation dependence of normalized material properties. 15

Table 3.3
Toughness and unloading characteristics of SS 316L woven wire mesh 16

Table 3.4
Normalized main axes properties of pre-processed samples 17

Table 3.5
Normalized mechanical properties of heat treated AR specimens 22

Table 4.1
Normalized elastic constants from orientation function for woven wire mesh . . . 25

Table 4.2
Normalized Hill Analogy parameters. 28

Table 4.3
Voce hardening model parameters for woven wire mesh. 32

Table 6.1
Elastic modulus evolution model parameters. 45

Table 7.1
Mechanical properties of wires used for FEM constitutive model. 49

Chapter 1: Introduction

Composite material mechanics is a thriving research field, stemming from the need for lightweight and high-strength materials selected for numerous cutting edge applications. The study of composites is generally classified into three scales: the micro, meso, and macro-scale. The micro-scale considers microstructural details such as surface defects or micro-cracks, and is not dealt with in the current study. The meso-scale is comprised of some representative volume element (typically one full weave period for fabrics) that captures component level interaction, while the macro-scale is representative of specimen sized sample behavior. Until recent advancements in numerical modeling techniques (i.e., homogenous plates and bricks), this research was restricted to idealized simple structures and somewhat limited mechanical tests (e.g. uniaxial tensile). More recently, analyses of the mechanical behavior of intricate composites have been performed in great detail using the finite element method and other numerical techniques. There are several approaches that have been presented by various authors who introduce models for this class of materials. Commonly employed are finite element models based on the representation of composites with user-defined constitutive models developed from idealizations of the meso-scale behavior [1, 2]. Geometrically accurate meso-scale finite element models are also used, typically for studying various layer interactions within the composite [3-6]. While the existing models have shown good agreement with experimental data, they are somewhat limited in their scope, as they tend to greatly simplify the composite geometry, or in the case of woven materials, only deal with the relatively simple geometries of plain and twill weave fabrics. This type of modeling is typically incapable of capturing the complete response of the material, ignoring such factors as the microstructural mechanisms leading to failure, interactions between components, and material evolution.

1.1 Literature Review

Pierce first addressed the modeling of woven textiles in 1936 [7] by proposing a simple geometric model for a plain weave fabric that formed the basis of several mechanical models in future works. The geometry consisted of round weft wires, orthogonal to the round warp wires and tangential at the interface. The weft wires were assumed to always be in plane, and were linear between the warps. These assumptions prove somewhat simplistic, not allowing for any crimping of the weft wires out of plane. The geometry of Pierce has been used in several cases to develop numerical models for the study of fabric behavior, most notably in the case of Tarfoui and co-authors [4]. Their work employed the Pierce geometric model in a 'fundamental cell' FE model. This model was used to facilitate damage prediction in the form of yarn breakage. Similar to the Pierce model, Kawabata [8] proposed a meso-scale model in 1964 that made use of a simplified geometry to study the biaxial deformation of plain weave fabrics. He treated the fabric yarns as simple beam like structures, imparting loads on each other at a single cross over point in the plane of the weave. This work was extended as King and co-workers [1] made use of Kawabata’s geometric model to formulate a continuum constitutive model for woven fabrics which considerably simplifies the load paths in the meso-structure. The approach, while an idealization, still proves very accurate for modeling in-plane loading. King and co-authors utilized a modified Kawabata geometry, adding axial and rotational springs at the contact points to simulate wire interaction. This model presents a means to predict macro-scale behavior based on the weave geometry and yarn (or wire) materials through a simplification that treats the weave as a homogenized anisotropic body. Such simplification of fabric geometry is common throughout the literature [1, 2, 9], but is typically made after significant numerical modeling or mechanical testing has been performed to formulate the material response, as is the case in the work presented here. After an exhaustive literature search, no models have been found that simulate the wire scale response of such a tortuously dense fabric at the meso-scale as is proposed in the current study; furthermore, little attention has been paid to the elasto-plastic region of the load-deflection curve. Presumably, this is due to the difficulty in developing a stable numerical model capable of handling the inherently non-linear contact equations used to model frictional wire contact.

Several mechanical testing methods for fabrics are present in the literature. The ASTM standard D4964 (2008) gives guidelines for the tension testing of elastic fabrics. The standard specifies a constant rate of extension (CRE) type test is to be used. The most common forms of testing are uniaxial and biaxial tension tests, typically performed at various material orientations. Kumazawa and co-workers [10] performed biaxial tests on plane stress cruciform specimens, and uniaxial tension tests on strip specimens. The use of cruciform (e.g. t-shaped) test specimens for biaxial testing of fabrics is fairly common in the literature, as it was also used by Kawabata [8], among others. Zheng and colleagues [11] proposed a novel testing method for fabrics, which employed a multi-axis circular tensile tester capable of measuring the mechanical properties of various fabrics in multiple directions at once. In order to validate their tester, they also performed uniaxial and cruciform biaxial tests on their fabric specimens. Perhaps the most sophisticated experimental setup present in the literature is proposed by Cavallaro and co-workers [3].

Their testing mechanism, referred to as a 'combined multi-axial tension and shear test fixture,' is capable of providing stiffness results both in shear and in multi-axial tension tests.

This paper presents research conducted to characterize the mechanical behavior of 325x2300 316L SS woven wire mesh subject to uniaxial tensile conditions. Data from CRE experiments on as received, pre-processed, and heat-treated specimens is presented, and various mechanical properties of the material are classified. An orientation study of the mechanical properties is performed, and models are proposed. The Voce hardening model [12] is employed to characterize the elasto-plastic region of the tensile test results. Ratcheting type tensile test data is presented and analyzed, and an orientation dependent continuum damage model is proposed. Finally, 3D FEM is employed to investigate the meso-scale response of the woven mesh.

1.2 The Woven Wire Mesh

The woven wire mesh has a long history of use as a filtration media in industry. Its ability to withstand relatively large pressures while still maintaining extremely high particle retention rates makes it an excellent choice for water reclamation applications. Most recently, this class of materials has been employed in explosive trace detection (ETD) devices, where its ability to sustain repeated thermal shock under high stress is key. The twill-dutch woven specimen of interest is an extremely dense and tightly woven fabric, with nominal and absolute pour sizes of 2 and 7 microns, respectfully. Twill refers to the over-two, under-two weaving of the weft wires with respect to the warp wires, while the term dutch implies that the weft wires are smaller in diameter (0.001in or 0.0254mm) than the warp wires (0.0015in or 0.0381mm). The weave geometry, as shown in Fig. 1.1a, then dictates that the overall thickness of the mesh is approximately 0.0035in (0.0889mm). Approximate crimp radius of curvature values are also provided in Fig.1.1a, with ρ_1, the radius in the *t*-weft plane, equal to 0.002in (0.051mm), and ρ_2, the radius in the warp-weft plane, equal to 0.005in (0.127mm). The given Wire diameters are as

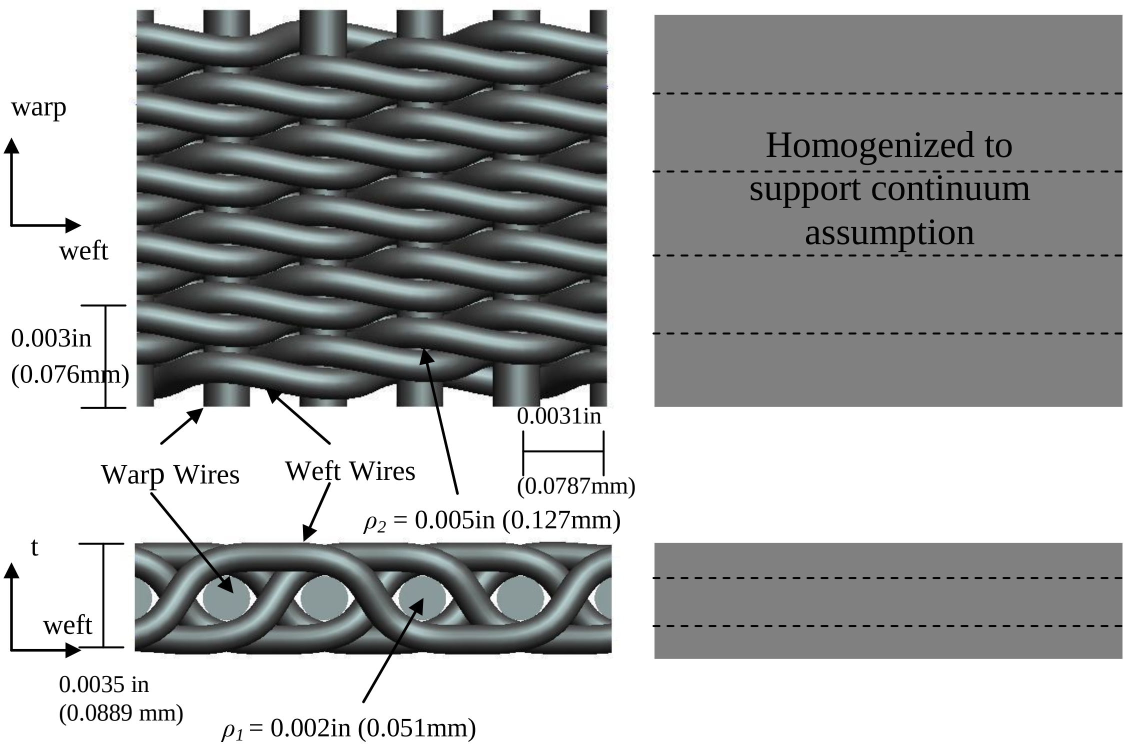

Figure 1.1: (a) Schematic representation of 316L stainless steel 325x2300 woven wire (b) Continuum representation of woven wire mesh.

reported by the manufacturer, and may vary within their tolerance limits. The weave count of the mesh selected for the current study is 2300 weft (or shute) wires by 325 warp (or toe) wires per inch (25.4mm).

The wire material in the representative woven mesh is 316L SS, chosen for its corrosion resistance, toughness, resistance to temperature variation, and strength. The material properties of AISI for this material are provided in Table 1.1 [13].

Table 1.1: Material properties of Stainless steel 316L wire at room temperature [13]

Units	Elastic Modulus, E	Yield Strength, s_y	Ultimate Tensile Strength, UTS	Density, ρ	Elongation (%)	Poisson's Ratio, ν
SI	193 GPa	205 MPa	520 MPa	0.008 g/mm^3	40	0.28
English	28.0 Msi	29.7 ksi	75.4 ksi	0.289 lbf/in^3	40	0.28

It should be noted, however, that the material properties of the actual wires making up the woven mesh may strongly differ from unprocessed 316L SS. A significant amount of processing during drawing and weaving causes considerable cold working of the wires, undoubtedly affecting their properties to some degree. Evidence of this may be observed from scanning electron microscopy (SEM) images taken of the sample specimens in Fig. 1.2. It is clearly shown that the weaving process causes areas of residual deformation in as-received samples. For the current study, residual deformation and stresses are ignored, and wires are assumed to have homogenous properties.

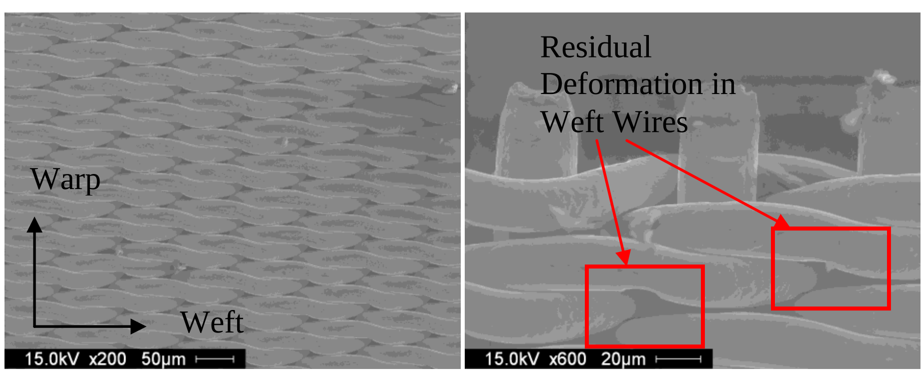

Figure 1.2: Scanning electron microscope images of the 316L stainless steel 325x2300 woven wire mesh showing residual deformation caused by the weaving process.

Chapter 2: Tensile Experiments

The ASTM standard D4964 (2008) provides guidelines for the mechanical testing performed on the woven wire mesh. The mechanical response of the woven wire mesh was determined by means of constant rate of extension (CRE) tensile testing at a rate of 0.01in/min (0.254mm/min) for all cases. Mechanical properties such as stiffness, yield strength, ultimate tensile strength, toughness, rupture strength, and elongation to failure could all be determined from one test. An electromechanical universal testing machine (MTS Insight 5) was applied for this endeavor. Several series of experiments were carried out until samples completely ruptured, as shown in Fig. 2.1.

Figure 2.1: Time-lapse photography of CRE tensile test conducted on 316L stainless steel 325x2300 mesh specimens in the warp (0°) orientation.

2.1 Single Wide Specimens

The single wide test specimens were incised to the typical dog-bone shape according to the specimen drawing shown in Fig. 2.2. The specimen shape was iteratively designed like a conventional test specimen (ASTM E8, 2004) so that failure occurred between the grips and away from the filleted sections of the sample. The results proved exceptionally reproducible in a vast majority of the experiments, with failure typically occurring away from the filleted grip ends as intended. Test specimens were fixed into place with a set of screw vice grips rated at 1.1kip (5kN). Each specimen featured a wave grip appropriate for testing thin and potentially difficult to grasp materials (e.g.

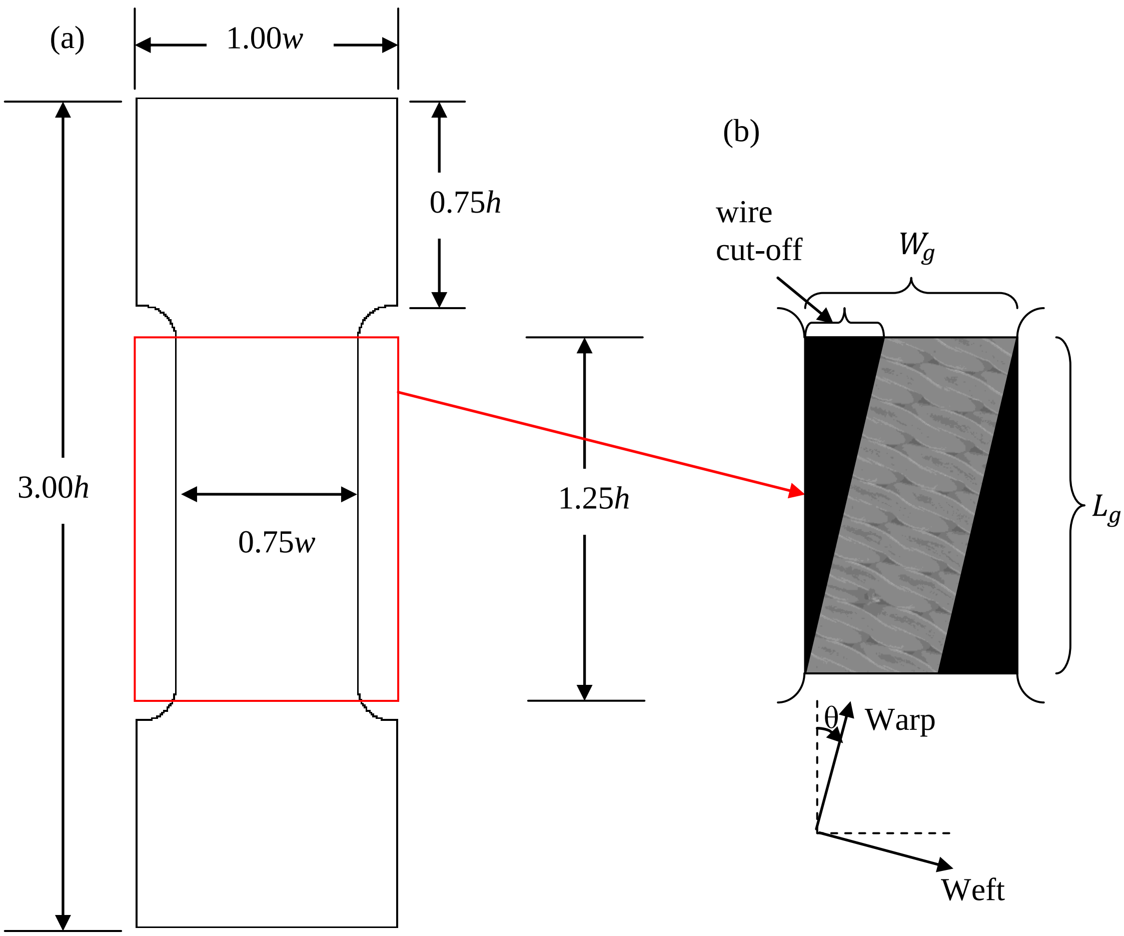

Figure 2.2: (a) Sketch of the incised test specimen used for tensile experiments of the 316L stainless steel 325x2300 woven wire mesh; w = 1.00in (25.4mm) for single wide and 2.00in (50.8mm) for double wide specimens, h = 1.00in (25.4mm) for all specimens. (b) Gauge section of the tensile test specimens.

bituminous, biomaterials, or geo-textiles). The mechanical grips (Test Resources model G86G), shown in Fig. 2.1, were aligned to impart axial loading without twist to the sample.

The orientation dependence of the material was investigated by conducting identical CRE experiments on samples that differed by orientation. Specimens were incised from the mesh sheets at intermediate orientations between the warp (0°) and weft (90°) axes in increments of 15°. In this manner, the mechanical properties of the warp and weft axes serve as a benchmark for the off-axis orientations.

2.2 Double Wide Specimens

As the woven wire mesh is incised at orientations increasingly off the main material axes (i.e., 30°, 45°, 60°), a certain degree of wire "cut-off" is unavoidable [10]. Consequently, several wires cannot fully participate in carrying the applied load during an off-axis tensile test, as is illustrated in Fig. 2.2b. This generates a unique end effect that may impact the material properties of the specimen. The affect of this end condition on the mechanical response of the woven wire mesh was investigated by incising the double wide test specimens. These specimens were tested in a similar orientation test series through resilience type tensile experiments. The double wide specimens were subjected to alternating ratcheting cycles during the resilience experiments. These tests provided load-deflection information similar to the single wide CRE type tensile experiments, hence conventional mechanical data could be obtained, as well as insight into the damage evolution and hysteresis of the 316L SS woven wire mesh. In order to quantify the effectiveness of the double wide samples in alleviating wire cut-off, an equation relating the shank-to-shank wire count, N', to the orientation angle, θ, ranging from 0° to 90°, is required, e.g.

$$N_w' = max\{0, \ \ N_w[W_g - L_g tan(\theta)]\} \tag{1a}$$

$$N_s' = max\{0, \ \ N_s[W_g - L_g tan(90° - \theta)]\} \tag{1b}$$

Here, L_g is the specimen gauge length, W_g is the specimen gauge width, N_w' is the shank-to-shank warp wire count after incision, N_s' is the shank-to-shank shute (or weft) wire count after incision, N_w is the original warp wire count pre-incision, and N_s is the original shute (or weft) wire count pre-incision. Using this relation, the degree of wire cut-off upon incision may be analytically determined. It can be shown that increasing the width of the sample effectively reduces the number of affected wires. For example, 30° oriented samples of the current study have fully active warp and weft counts of 9 and 0 for single wide, and 253 and 0 for double wide samples respectively.

2.3 Pre-conditioned Samples

Several material samples were provided by L3 Communications, a manufacturer of ETD equipment, so that the effectiveness of several proprietary thermal and chemical pre-treatments could be tested. Provided were four different pre-processed versions of the 325x23000 316L SS woven wire mesh material, denoted as BL, B3, PP, and AI in this paper. The pre-processed materials were incised into single wide specimens that varied by orientation from 0° (warp) through 90° (weft) in 15° intervals. They were then tested via CRE tensile tests in the same manner as the un-processed specimens. To gain additional insight into the effects of heat treatment on the material properties of the woven mesh, several specimens of each material class (AR, AI, PP, BL, B3) were heat treated at 600°F for either 100 or 200 seconds, and then left to cool at room conditions. These specimens were incised to the single wide dimensions at the main material orientations (warp and weft), and were tested using the CRE method described previously.

Chapter 3: Tensile Behavior

3.1 As Received (AR) Tensile Material Properties

The main weave directions, referred to as the warp (θ = 0°) and the weft (θ = 90°) as illustrated in Fig. 1, serve as clear points of reference for the classification of the tensile behavior of the 325x2300 316L SS woven wire mesh. The main orientations represent the only cases where pure tensile conditions can be produced via uni-axial tensile tests on the woven mesh due to the onset of shear-coupling effects in off-axis tests [14], hence acting as benchmarks for the off-axis experiments. In order to analyze the variability of the tensile data that was to be collected, ten CRE experiments were initially performed in the warp (0°) orientation. These CRE experiments are represented by test specimens AR-001 through AR-010, and the significant results of these tests, including yield strength, ultimate tensile strength, etc. are presented in Table 3.1. Individual tests results for all specimens are included in the appendix. Values from experiments are normalized here to help emphasize variation, with A_0 = 0.00248in^2 (1.60mm^2), k_0 = 2327lb/in (407.5kN/m), S_{y0} = 11.4ksi (78.6MPa), UTS_0 = 12.7ksi (87.6MPa), S_{f0} = 11.9ksi (82.0MPa), and ε_{fo} = 0.084in (2.13mm). Note that the cross-sectional area, A_o, represents the homogenized continuum assumption shown in Fig. 1.1b. The highest degree of standard deviation observed in the normalized data was in the elongation to failure, with an acceptable value of 0.12. Yield strength and stiffness also show notable normalized standard deviations, with values of 0.04, and 0.10 respectfully.

__Table 3.1__: Normalized Mechanical properties of 316L SS Woven Wire Mesh in warp direction

Specimen ID	Cross-Sectional Area, A/A_0	Stiffness, k/k_o	Yield Strength, S_y/S_{yo}	Ultimate Strength, UTS/UTS_o	Fracture Stress, S_f/S_{fo}	Elongation, ϵ_f/ϵ_{fo}
AR-001	1.00	1.00	0.95	1.00	1.00	1.00
AR-002	1.01	0.96	0.89	0.97	1.00	0.92
AR-003	1.01	1.08	0.98	0.98	1.00	1.04
AR-004	0.99	1.17	1.00	1.03	1.00	1.13
AR-005	0.99	1.25	0.96	1.01	1.01	0.83
AR-006	0.99	1.05	0.96	1.03	0.98	1.13
AR-007	0.99	1.24	0.97	1.01	0.98	1.04
AR-008	1.00	0.99	1.01	1.01	0.99	1.11
AR-009	0.99	1.17	0.98	1.04	1.00	1.08
AR-010	1.00	1.05	1.02	1.03	0.98	1.25

These values are considered within statistical error limits for mechanical testing of this class of materials, and so it was justified to proceed with further testing of the material without multiple test duplications.

The mechanical response of the most representative warp (0°) sample (AR-003), and the weft (90°) sample (AR-016) are presented in Fig. 3.1a. Points δ_A and δ_B, shown in the figure, are key points to be studied using FEM. It is clear that the weft (90°) orientation possesses superior strength and stiffness with respect to the warp (0°) orientation, and that it also undergoes more substantial work hardening. The failure characteristics of the two main orientations vary significantly, with the weft (90°) orientation failing abruptly and thoroughly upon reaching its ultimate tensile strength, and the warp (0°) orientation displaying more ductile behavior with a gradual unloading.

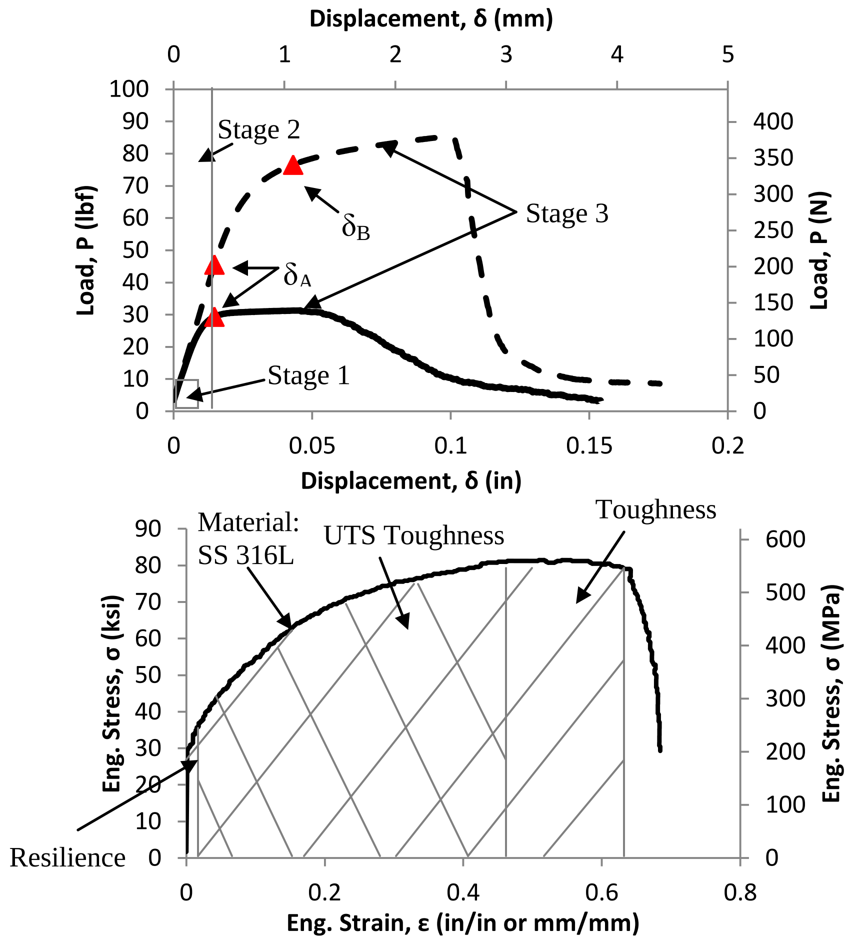

Figure 3.1: (a) Mechanical response of main weave axes of 325x2300 316L stainless steel woven wire mesh subject to constant rate extension tensile testing $\dot{\delta} = 0.01\frac{in}{min}$ $(0.254\frac{mm}{min})$. (b) Typical stress-strain curve for 316L SS [13] showing key toughness zones used to analyze the behavior of the woven wire mesh.

Analysis of the material in the weft (90°) orientation reveals some details about the nature of the mechanical response of woven materials in general. Figure 3.1a illustrates that the material undergoes three stages of loading when placed in tension. Stage 1 corresponds to tightening and potential sliding occurring between the adjacent and orthogonal wires, and is considered a non-linear and non-recoverable stage, as frictional forces would prevent the mesh from recovering sliding and tightening displacements. Stage 2 represents the elastic portion of the loading phase, during which wire deformation is dominated initially by crimp interchange, and subsequently by wire tensioning. Crimp interchange, studied in detail by Cavallaro and co-workers [3], is the phenomenon in which the pre-crimped weft wires attempt to straighten, an in effect cause the warp wires to become crimped. Stage 3 represents the elastic-plastic transition, followed by the non-linear strain-hardening of the material.

The tensile response of the 325x2300 316L stainless steel woven wire mesh varies significantly with orientation. Parameters such as stiffness, yield strength, ultimate strength, toughness, and elongation to rupture are all highly dependent on orientation. Figure 3.2 provides the orientation dependence of the mechanical response of the mesh when subject to displacement controlled tensile testing. Maximum stiffness, yield strength, and ultimate strength are observed in the weft (90°) direction at 2.88kip/in (504.0kN/m), 23.0ksi (158.6MPa) and 34.4ksi (237.2MPa) respectively.

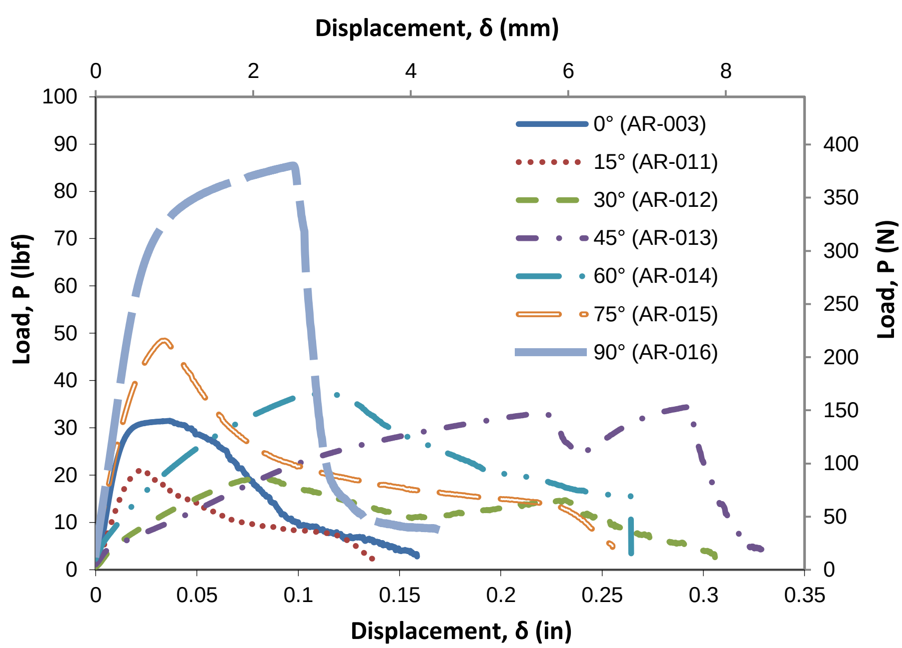

Figure 3.2: Orientation dependence of the mechanical response of 325x2300 316L stainless steel woven wire mesh subject to CRE tensile testing $\dot{\delta} = 0.01\frac{in}{min}$ $(0.254\frac{mm}{min})$.

Minimum yield strength occurs in the 45° orientation at 1.8ksi (12.4MPa); however, this orientation shows exceptional toughness of 2.35ksi (16.2MPa). Minimum ultimate strength is observed in the 30° orientation, with a value of 7.66ksi (52.8MPa). Stage 1 loading becomes more pronounced as the material orientation approaches 45°, where shearing effects cause the weft wires to rotate slightly on their contact points with the warp wires. Most orientations display predominantly linear behavior during stage 2 loading; however, the 30° and 60° orientations display distinctly non-linear behavior. The warp (0°) direction displays a local maxima for yield strength and ultimate strength through 45°, but with significantly less toughness, 885.7psi (6.11MPa) than the weft (90°) direction. The warp (0°) orientation also shows the least elongation to fracture, and very little potential for work hardening. The 45° orientation shows the largest elongation to fracture, and undergoes a much larger amount of work hardening than any other orientation. Two orientations, 30° and 45°, show multiple yield points. The appearance of this phenomenon in multiple tests suggests that it is not an inconsistency in the data resulting from a poor test or end condition. The yield strength, stiffness, and elastic modulus reported for these orientations reflect the initial observed yield points. Table 3.2 provides normalized mechanical properties such as yield strength, ultimate tensile

Table 3.2: *Orientation dependence of normalized material properties of 316L SS Woven Wire Mesh*

Specimen ID	Orientation, θ (deg)	Cross-Sectional Area, A/A_o	Stiffness, k/k_o	Yield Strength, S_y/S_{yo}	Ultimate Strength, UTS/UTS_o	Fracture Stress, S_f/S_{fo}	Elongation, ϵ_f/ϵ_{fo}
AR-011	15	1.00	0.56	0.66	0.67	0.68	0.98
AR-012	30	1.02	0.12	0.60	0.60	0.60	3.78
AR-013	45	1.02	0.24	0.16	1.07	0.92	4.55
AR-014	60	1.02	0.20	0.96	1.16	1.21	3.30
AR-015	75	1.01	0.82	1.39	1.52	1.27	1.26
AR-016	90	1.00	1.24	2.02	2.71	2.48	1.62

strength, stiffness, and elongation to failure of 325x2300 stainless steel woven wire mesh with respect to material orientation, where the normalization values are as in Table 3.1. The reported properties may be deduced directly from Figs. 3.1 and 3.2 as macro-scale characteristics of the material.

More in-depth analyses of the material response are also performed, with properties such as resilience, toughness, and the unloading slope of each orientation being investigated. The unloading slope was analyzed as a measure of brittleness of the fracture, which indicates possible concentration of material evolution. The 60° orientation shows the highest resilience, while the 45° orientation shows the least. The weft (90°) direction shows the highest degree of toughness, with the lowest toughness occurring in the 15° orientation. The weft (90°) orientation shows the most brittle failure, with a very steep unloading slope, and the 30° orientation possesses the most gradual unloading. These normalized results are presented numerically for each orientation in Table 3.3, where u_{ro} = 81.5*psi* (0.562*MPa*), u_{utso} = 396.2*psi* (2.73*MPa*), u_{fo} = 885.7*psi* (6.11*MPa*), and k_{uo} = 503.4*lb/in* (88.16*kN/m*). The various toughness values reported here are defined by Fig. 5b.

Table 3.3: *Normalized Toughness and Unloading Characteristics of 316L SS Woven Wire Mesh*

Sample ID	Orientation, θ (°)	Resilience, u_r/u_{ro}	UTS Toughness, u_{uts}/u_{utso}	Toughness, u_f/u_{fo}	Unloading Slope, k_u/k_{uo}
AR-003	0	1.00	1.00	1.00	-1.00
AR-011	15	0.73	0.242	0.554	-0.461
AR-012	30	2.81	0.808	1.33	-0.223
AR-013	45	0.11	3.77	2.66	-0.957
AR-014	60	4.29	2.34	2.31	-0.413
AR-015	75	2.24	0.923	2.04	-1.19
AR-016	90	3.54	5.59	3.05	-8.77

3.2 Pre-processed Material Properties

The mechanical response of the provided pre-processed samples shows that this material is responsive to heat treatment and other pre-processing methods aimed at enhancing the material properties. Heat treatment is an ideal method of processing in this class of materials, as it effectively relaxes residual stresses caused by the drawing and weaving of the wires into the mesh, as evidenced by Fig. 1.2. The relaxation of these stresses reduces the amount of initial damage present in the mesh, thereby enhancing properties such as stiffness and strength. This is evidenced by the tensile response of the pre-processed materials, which display markedly improved characteristics. Figure 3.3 shows the mechanical response of the main material orientations for the pre-processed samples (AI, PP, BL, and B3), with respect to the AR samples. It is noted that the pre-processing techniques are proprietary, and so the discussion of the effectiveness of the various methods is limited to a discussion of the respective load-displacement displacement curves. Table 3.4 provides the normalized material properties for the main axes CRE tensile tests on the pre-processed material samples.

Table 3.4: *Normalized main axes properties of pre-processed 325x2300 SS316L woven wire mesh*

Specimen ID	Orientation θ (deg)	Cross-Sectional Area, A/A_o	Stiffness, k/k_o	Yield Strength, S_y/S_{yo}	Ultimate Strength, UTS/UTS_o	Fracture Stress, S_f/S_{fo}	Elongation, ϵ_f/ϵ_{fo}
PP-007	0°	0.935	0.788	1.05	1.06	0.987	0.583
PP-016	90°	0.950	0.986	2.17	2.71	1.34	0.726
AI-005	0°	0.992	0.992	1.10	1.15	1.04	1.047
AI-016	90°	1.06	1.50	2.20	3.04	3.23	1.095
BL-002	0°	1.07	1.659	1.52	1.676	1.38	1.73
BL-016	90°	1.08	1.437	2.11	2.65	2.82	0.928
B3-005	0°	1.09	1.02	1.30	1.30	0.991	1.423
B3-016	90°	1.05	1.51	2.067	2.81	3.00	0.904

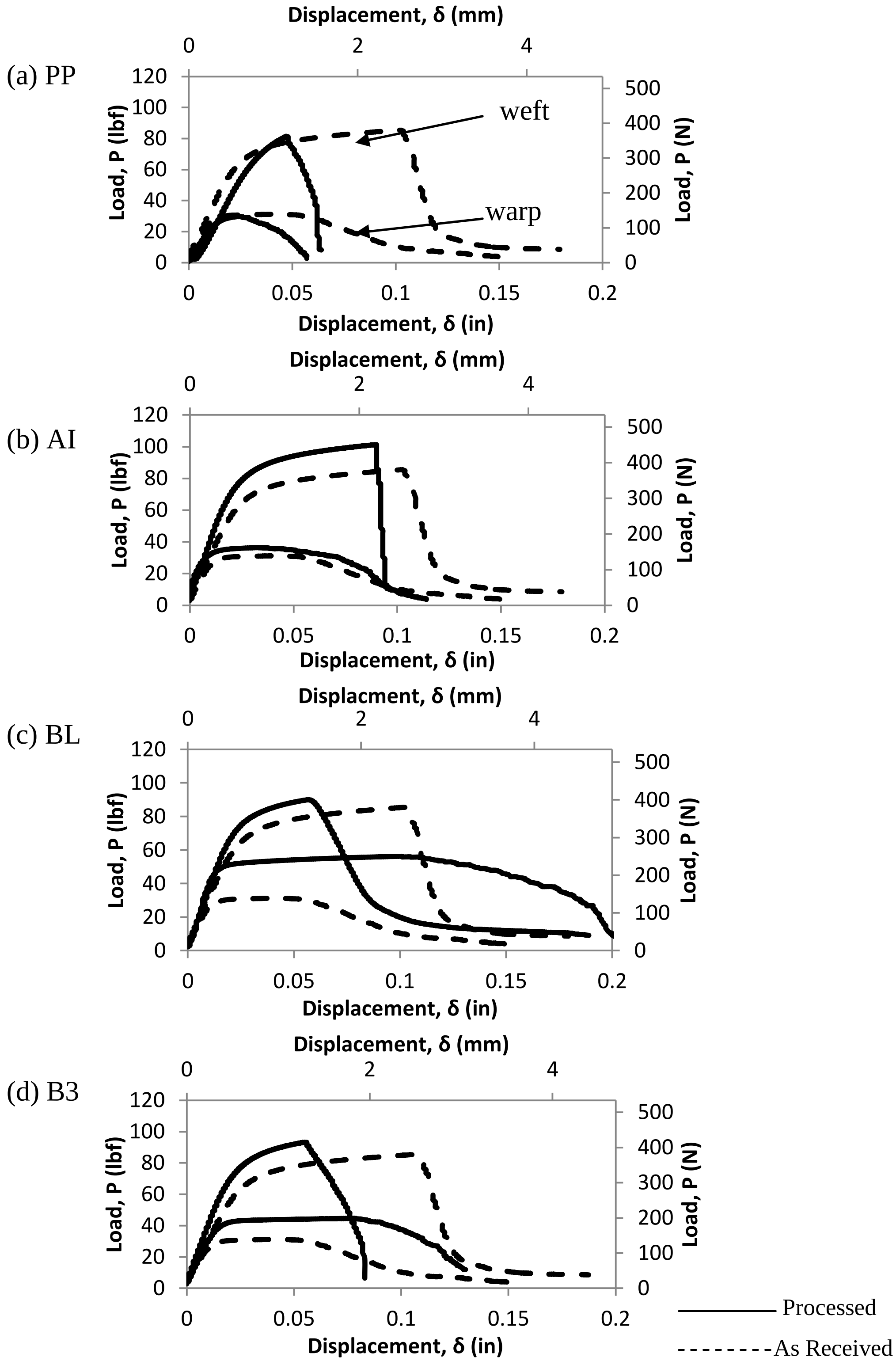

Figure 3.3: Main axes mechanical response of 325x2300 SS 316L woven wire mesh subject to CRE tensile testing after various pre-processing applications, where (a) PP, (b) AI, (c) BL, and (d) B3

It is observed that the most effective pre-treatment process, in terms of increasing stiffness and yield strength, is the BL process. The process produces stiffness in the warp (0°) direction of 3861.7*lb/in* (676.*3kN/m),* and 3344.9*lb/in* (585.8*kN/m*) in the weft (90°) direction. Yield strength values for BL are 17.*34ksi* (119.6*MPa*) for the warp (0°) direction, and 24.09*ksi* (166.1*MP*) in the weft (90°) direction. As seen in Table 3.4 and Fig. 3.3, the PP process proves largely ineffective at enhancing material properties, with significant weakening observed in the weft (90°) orientation, and no notable strength or stiffness increases observed in the warp (0°) direction. It is also noted that the PP process reduces toughness and elongation to rupture in both warp (0°) and weft (90°) cases, leading to the conclusion that this process should be avoided during mesh production. The highest elongation to rupture in the warp (0°) orientation was observed in the BL specimens at 0.188*in* (4.77*mm*), while the weft (90°) specimens were all adversely affected by the heat treatment, displaying relatively low elongations to rupture. The highest ultimate strength in the warp (0°) orientation is again observed in the BL processed samples at 21.3*ksi* (146.9*MPa*), while the AI specimen displays the highest weft (90°) orientation ultimate strength at 25.17*ksi* (173.5*MPa*). Note that the BL warp (0°) ultimate strength is nearly double that of the untreated AR samples. In general, it is concluded that, in terms of strength and stiffness enhancement, the AI treatment is the most promising for weft (90°) dominant applications, and the BL treatment is the superior process for warp (0°) dominant applications.

3.3 The Affects of Heat Treatment

In an effort to further investigate the affect of heat treatment on the material properties of the woven wire mesh, samples were heated in a furnace at 600°F for 100

Figure 3.4: Furnace setup used to apply 600°F temperatures to the 325x2300 SS 316L woven wire mesh samples for either 100 seconds or 200 seconds.

seconds and for 200 seconds. These specimens represent s ample numbers (017) through (020) for each respective material classification (AR, AI, BL, B3, and PP). The furnace setup used to conduct the heat treatment on the 325x2300 SS316L woven wire mesh samples is displayed in Fig. 3.4.These treatments have varying impacts on material properties, with the degree of change dependant on the pre-processing of the samples. For example, as illustrated in Fig. 3.5, the un-processed AR samples show a significant degree of strengthening and stiffening in both the warp and weft axes when subjected to a thermal load for 100 seconds, whereas the BL samples display only a marginal increase in stiffness, and no statistically relevant change in strength. For this reason, the discussion of heat treated specimens must be limited to the previously untreated AR specimens, shown in Fig. 3.5a

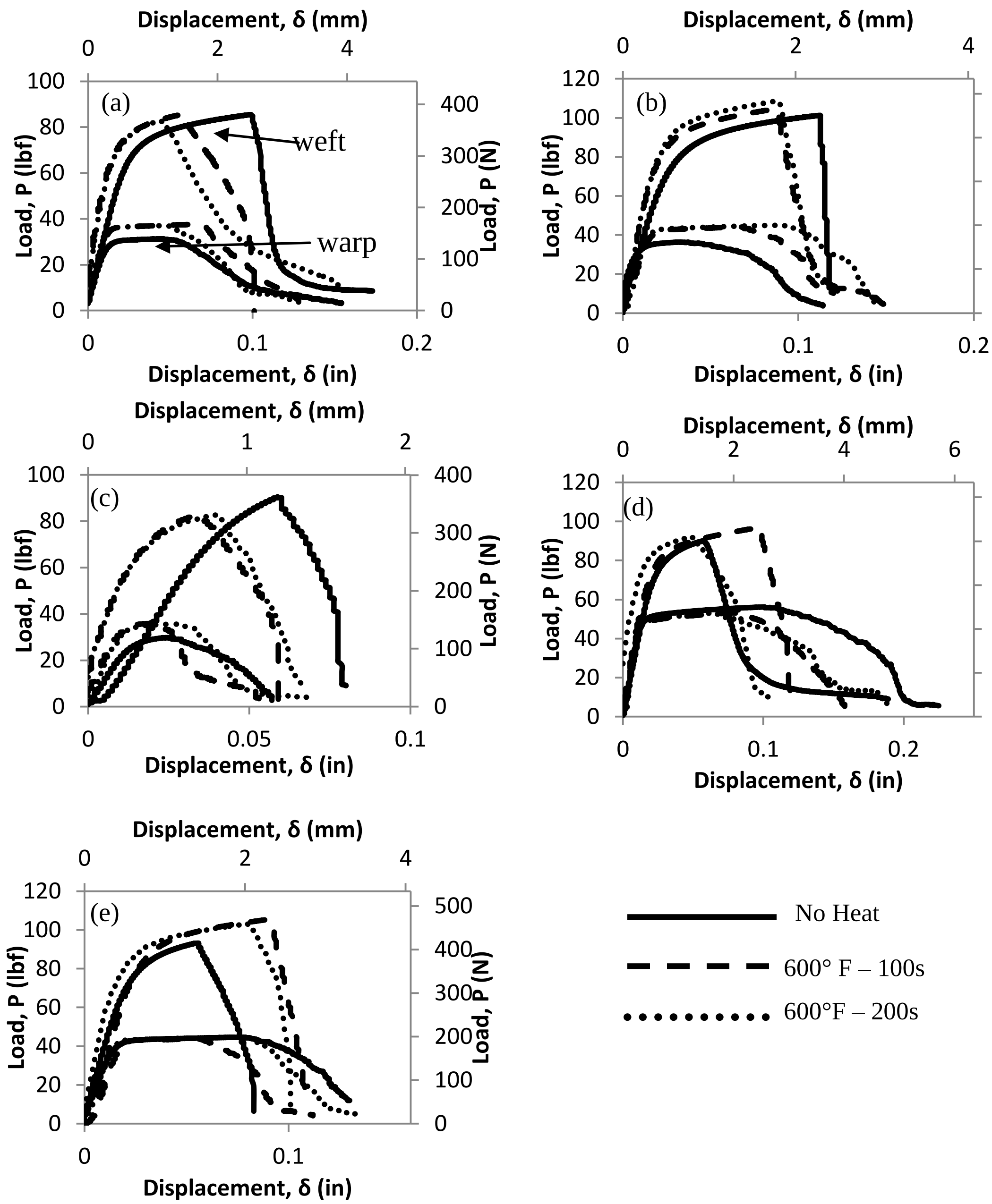

Figure 3.5: The affect of heat treatment on various 325x2300 SS316L woven wire mesh samples, where (a) AR, (b) AI, (c) PP, (d) BL, and (e) B3.

Table 3.5: *Normalized material properties for heat treated AR SS316L woven wire mesh samples*

Specimen ID	Orientation, θ (deg)	Heating Time, s	Stiffness, k/k_o	Yield Strength, S_y/S_{yo}	Ultimate Strength, UTS/UTS_o	Fracture Stress, S_f/S_{fo}	Elongation, ϵ_f/ϵ_{fo}
AR-017	0	100	1.01	1.16	1.14	1.19	1.11
AR-018	90	100	1.01	1.68	2.11	2.67	2.21
AR-019	0	200	1.04	1.15	1.12	1.13	0.98
AR-020	90	200	1.01	1.70	2.16	2.61	2.71

It is observed in Fig. 3.5a that heat treatment improved elasto-plastic performance of the AR specimens in the main material axes, however toughness and elongation to rupture are reduced as a result. Heat treatment markedly increases yield strength of the as received material in both the warp (0) and weft (90) direction, with increases of 7.8% and 10.2% over the untreated samples, respectively. It is also observed that material stiffness is increased significantly after heat treatment, with values of 2691.4*lb/in* (471.3*N/m)* in the warp and 3902.9*lb/in* (683.*5N/m*) in the weft (90) after treatment for 100 seconds, gains of 32.2% and31.4% respectively. Heat treated material properties, normalized as in Table 3.1, are summarized in tabular form by Table 3.5. Investigation reveals that there is little to gain by increasing the heat treatment time from 100 to 200 seconds, which in fact reduces fracture stress and elongation to rupture in the warp (0) orientation. The most significant material characteristic change is observed in the elongation to failure for the weft AR samples, with failure occurring at roughly half the displacement of the non heat treated samples. The reduction in ductility may be explained by the heat treatment process, in which the specimens were removed from the furnace and allowed to cool at room temperature. The low mass and small cross-section of the wires allows the cooling process to happen quite rapidly, even at room conditions, resulting in increased strength but reduced ductility in the weft wires.

Chapter 4: Homogenous Orthotropic Modeling

The mechanical response of a woven wire mesh at the meso-scale is multifaceted and complex, with factors such as crimp interchange, wire sliding, wire binding, and wire tensioning all occurring simultaneously and dependently. Comprehensive mechanical analysis at the wire level quickly becomes unwieldy, and so an assumption that allows for the analysis of the material at the macro level is ideal. The assumption of homogeneity enables these materials to be modeled with a simplified orthotropic constitutive model. An orthotropic material may be defined as any material that possesses two perpendicular planes of symmetry in which the properties of the material are independent of orientation. Most woven wire mesh materials possess two distinct and perpendicular weaving directions, referred to as the warp and the weft. The respective wire directions often possess their own distinct material properties due to differences in wire arrangement, size, density, processing, etc. Taking advantage of this wire configuration allows the assumption that woven meshes behave as thin orthotropic sheets under plane stress, resulting in simple elastic constitutive equations, i.e.,

$$\begin{bmatrix} \epsilon_x \\ \epsilon_y \\ \gamma_{xy} \end{bmatrix} = \begin{bmatrix} \frac{1}{E_x} & \frac{-\nu_{yx}}{E_y} & 0 \\ \frac{-\nu_{xy}}{E_x} & \frac{1}{E_y} & 0 \\ 0 & 0 & \frac{1}{G_{xy}} \end{bmatrix} \begin{bmatrix} \sigma_x \\ \sigma_y \\ \tau_{xy} \end{bmatrix} \tag{2}$$

Here E_x and E_y are the elastic moduli in the *x* and *y* directions respectfully, and G_{xy} is the shear modulus. Of the two Poisson's ratios, ν_{xy} and ν_{yx}, one is dependant due to symmetry of the compliance tensor.

4.1 Elastic Modeling

The elastic modulus and yield strength of the 316L SS woven wire mesh show strong dependence on material orientation, with the maxima of the given material property at the 0° and 90° orientations, and the minima occurring somewhere in-between. By transforming the constitutive equations for an orthotropic thin sheet, it can be shown [14] that the elastic modulus of such a material follows a trigonometric relationship, i.e.,

$$E_\theta = \left[\frac{1}{E_1} cos^4\theta + \left(\frac{1}{G_{12}} - \frac{\nu_{12}}{E_1}\right) sin^2\theta cos^2\theta + \frac{1}{E_2} sin^4\theta\right]^{-1} \qquad (3)$$

Using G_{12} and ν_{12} as curve fitting parameters, Eq. (4) serves as an orientation model for the elastic modulus of the 316L SS woven wire mesh. Figure 4.1 illustrates the orientation-dependence of the elastic modulus of the representative material along with the distribution predicted by Eq. (3), referred to as the 'elastic modulus orientation function' (EMOF).

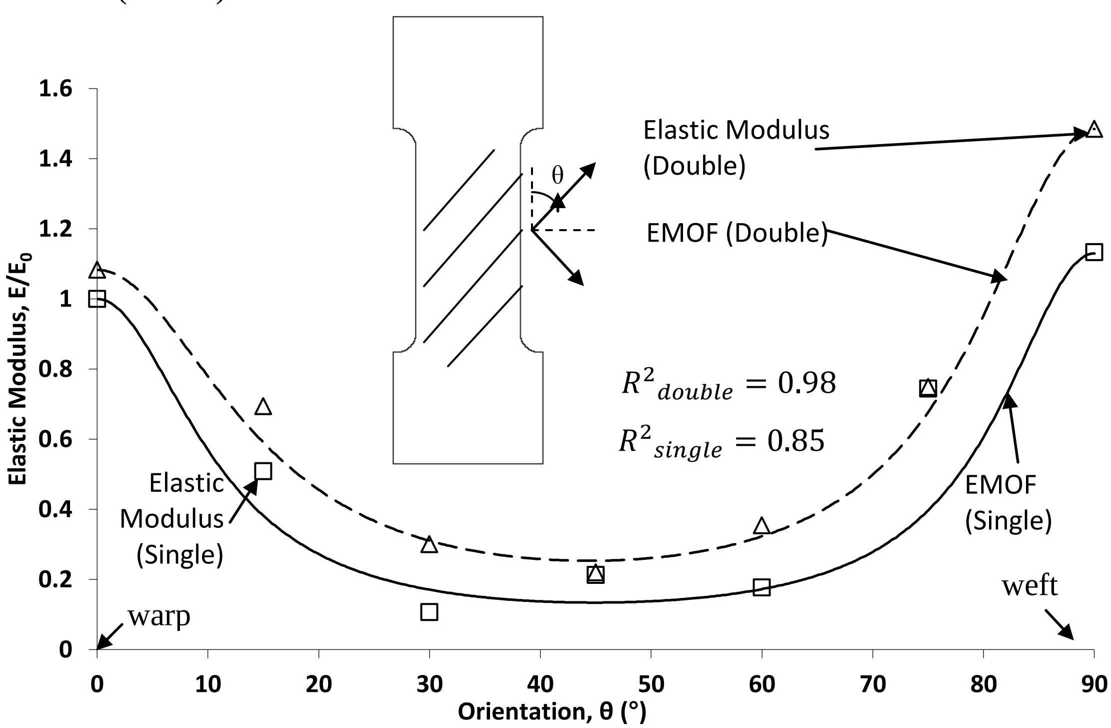

Figure 4.1: Double and single wide elastic modulus dependence on orientation for SS316L 325x2300 woven wire mesh plotted with respect to the elastic modulus orientation function for each case.

The experimental results strongly support the model, with R^2 values of 0.85 and 0.98 for the single and double wide data, respectively. The slight "bump" in the single wide elastic modulus at the 45° orientation may be attributed to the fact that the shear stiffness of this material is considerably higher than similar woven fabrics due to its extremely tight weft wire draw-down. Table 4.1 provides the values used in the EMOF to produce the curve fits for the elastic modulus. Here, $E_1$and E_2 represent the warp (0°) and weft (90°) orientation elastic moduli respectfully, E_o represents the elastic moduli for the single wide warp (0°) used to normalize the data (1.28Msi or 8.83GPa), ν_{12} represents the regression modeled Poisson's Ratio, and G_{12} represents the modeled shear modulus. Future work is planned to improve this elastic model with the inclusion of shear coupling effects.

Double wide specimens produced moduli values that are generally higher than their single wide equivalents. The 30° orientation double wide elastic modulus shows the maximum percent difference with the single wide at 98.4%. Variation in the off-axis double wide elastic moduli could potentially be attributed to the relatively small aspect ratio of the double wide samples. It has been shown [15] that orthotropic specimens which exhibit shear coupling may be affected by adverse boundary conditions if clamped at both ends, as is the case in this study. Such clamped end conditions produce bending moments and shear forces that may distort the sample, creating a non-uniform stress distribution that impacts test results.

Table 4.1: *Normalized EMOF constants for 325x2300 316L SS woven wire mesh*

	Warp Elastic Modulus, E_1/E_0	Weft Elastic Modulus, E_2/E_0	Poisson's Ratio, ν_{12}	Shear Modulus, G_{12}/E_0
Single Wide	1.000	1.130	0.350	0.035
Double Wide	1.083	1.485	0.350	0.068

Short and wide specimens are more adversely affected by these end conditions than longer and narrower ones because the majority of the gauge length is not sufficiently removed from the boundary to mitigate the effects [16]. The degree to which the boundary conditions may affect the double wide off-axis modulus values is unclear, but it is noted that several of the orientations (0°, 45°, and 75°) produced results within error limits with respect to the single wide samples. Future work is planned to investigate the impact of shear coupling on the observed off-axis material properties for 316L SS woven wire mesh.

4.2 Elasto-Plastic Modeling

Hill's failure criterion [17], is widely used for anisotropic, orthotropic, and transversely-isotropic solids. The theory is based on Distortion Energy Theory, and can be shown to reduce in the case of isotropy. The criterion relates the overall yield strength of the material to the principal directions through the use of several curve fitting parameters, resulting in a second order polynomial, e.g.

$$F(\sigma_y - \sigma_z)^2 + G(\sigma_z - \sigma_x)^2 + H(\sigma_x - \sigma_y)^2 + 2L\tau_{yz}^2 + 2M\tau_{zx}^2 + 2N\tau_{xy}^2 = 1 \qquad (4)$$

The terms F, G, H, N, M, and L are determined experimentally through an orientation study of the tensile yield strength of the material. This relation may be reduced for the plane stress case, where only F, G, H, and N are needed. Two possible methods may be used to identify these four constants through mechanical testing. The first method is a direct approach in which the definitions of the parameters are employed. For example, under uniaxial tension in the x direction, G and H strongly determine the response at yield, while uniaxial tension in the y direction is dominated by H and F. In cases of pure shear, N strongly influences the yield response, and in cases of equibiaxial tension in x

and *y*, the yield response is governed by *G* and *F*. The execution of these four experiments represents one method of characterizing the plane stress response of an orthotropic material. It should be noted, however, that is difficult to accurately evaluate the shear response of thin materials, as a lack of out-of-plane strength can easily lead to the formation of wrinkles. To avoid this difficulty, another set of experiments may be performed in which the material is subjected to uniaxial tension in the principal orientations, and at several intermediate orientations [14]. A regression analysis with the observed yield stresses at each orientation then produces the required constants.

The Hill analogy [17] was employed in an effort to model the orientation dependence of yield strength for the 316L SS woven wire mesh. The yield criterion proved adequate as a model to formulate the failure (defined as global yielding) of the material with respect to orientation, yielding R^2 values of 0.83 and 0.85 when applied to the single and double wide data, respectively. Although the developed model does not take into account the formulation of wire damage, nor the mode of wire failure, this model does allow for very useful macro-level strength predictions. To develop this model, a set of experimentally determined Hill parameters were derived through regression analysis such that they both satisfy the orthotropic Hill equation, and provide an optimal level of curve fit to the experimental data. It is noted that the Hill analogy, in its present form, is incapable of accurately modeling the observed fluctuation in the yield strength of the material (particularly in the 30°, 45°, and 60° off-axis orientations). Furthermore, if the secondary yield points of the 30° and 45° orientations are taken as the material yield strengths, a "double bump" develops in the data that could be attributed to shear coupling, which has not been dealt with in this model. It is also noted that the orientation model predicts minimum yield strength at about the 35° orientation, whereas experiments have shown minimum yield strength in the 45° orientation. The optimal Hill analogy parameters for the representative material are provided in Table 4.2, and the resulting orientation model is plotted in conjunction with the normalized experimental data in Fig. 4.2. The similarity of the two Hill analogy curves (single and double wide) provides strong evidence that the double wide specimens are sufficiently wide to capture the behavior of the material, and that further specimen widening will not appreciably affect the test results.

***Table 4.2**: Experimentally determined Hill's Analogy parameters for 316L SS woven wire mesh*

Parameter	G [1/*ksi*^{2}] or [1/*MPa*^{2}]	F [1/*ksi*^{2}] or [1/*MPa*^{2}]	N [1/*ksi*^{2}] or [1/*MPa*^{2}]	H [1/*ksi*^{2}] or [1/*MPa*^{2}]
Single Wide	0.770	1.410	-0.980	-0.530
Double Wide	0.550	1.230	-0.767	-0.346

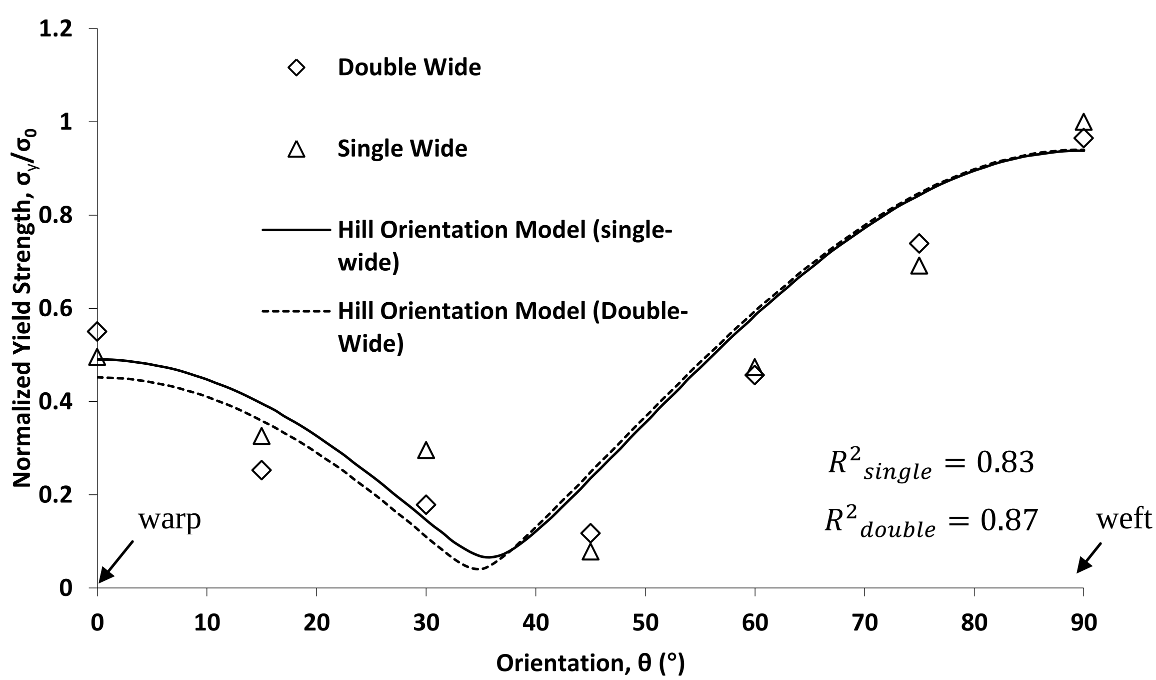

Figure 4.2: Orientation dependence of the yield strength of 325x2300 woven wire mesh

The orientation dependence of the yield strength of this material possesses an atypical degree of 'waviness', suggesting that the tight weave geometry may be a hindrance to shear deformation, providing enhanced shear properties not observed in comparable materials. Shear jamming and tightening occur quickly, in effect adding increased stiffness and strength to the material at high shear angles. This behavior is not observed in less densely woven fabrics, which have relatively small shear stiffness, and tend to have a more uniform yield strength orientation dependence. Figure 4.2 shows the dependence of the normalized yield strength of the 316L SS woven wire mesh on material orientation, with σ_0= 23.0ksi (158.6MPa). Both the 30° and 45° orientations possess secondary yield points, and the values reported for yield strength reflect the more conservative value. Systematic characterization of the mechanisms influencing the observed 'waviness' in the yield strength of this material with respect to orientation is left for future study.

The percent difference of single and double wide yield strengths is much higher in the warp dominant orientations than in the weft dominant orientations. The double wide yield strength observed in the warp (0°) orientation is within 10% of the mean single wide warp (0°) yield strength. It has been previously shown that single wide warp (0°) samples (AR-001 through AR-010) display a considerable amount of variation in their yield strengths, and so significant double wide strength variation in the warp dominant orientations (i.e., 0° through 30°) is not unfounded. Strength variability may be explained by the unloading behavior observed in these orientations. The gradual unloading slope observed in the warp (0°) orientation, shown in Fig. 3.1 and quantified in Table 3.3, implies a dispersed fracture process zone, leading to inconsistent yielding of the woven wire mesh in warp dominant orientations. As the orientation moves beyond 45° and becomes weft dominate, the degree of scattering goes from a maximum of 49.5% at 30°, to less than 5% at 90°; considered well within statistical error limits for this type of testing.

4.3 Voce Hardening Model

In order to aid in the classification of the elasto-plastic behavior of 316L SS woven wire mesh, the strain hardening behavior of the material at each orientation was modeled via a Voce hardening relationship, i.e.,

$$P_h = P_y + R_0\left(\frac{\delta_p}{L_0}\right) + R_\infty\left[1 - e^{-b\left(\frac{\delta_p}{L_0}\right)}\right] \tag{5}$$

The current formulation is a slightly modified version from the original model [12]. Rather than stress versus plastic strain, load versus plastic displacement is modeled. The model contains three parameters that are determined through inspection of the tensile test results. For example, R_∞, the strain hardening coefficient, is the difference between the proportional limit and yield strength of the respective material. In addition, R_0, the stiffness coefficient, controls the hardening rate, and *b*, the strain hardening exponent, influences the elasto-plastic transition curvature. In addition to these terms, P_y is the observed proportional limit, L_o is the specimen gauge length, P_h is the modeled plastic load, and δ_p is the plastic deformation. Regression analysis was performed to develop the optimal parameter value for each orientation, and these hardening parameters are provided in Table 4.3. Figure 4.3 provides the modified Voce hardening model plots in

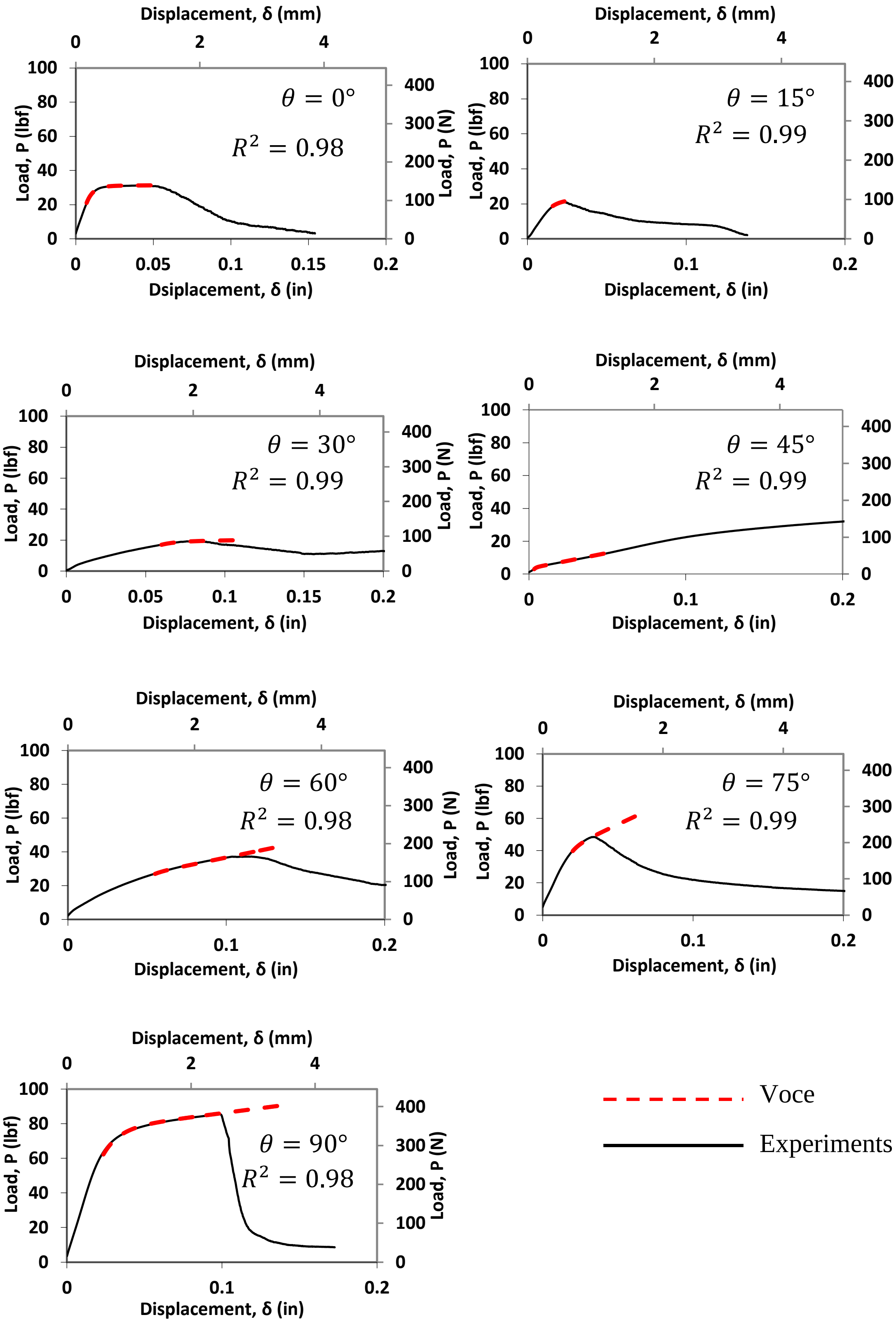

Figure 4.3: Modified Voce hardening models applied to 316L SS woven wire mesh specimens at various orientations, with R^2 values through ultimate tensile strength.

Table 4.3: *Voce Hardening Model Parameters for SS 316L Woven Wire Mesh (single wide)*

Orientation, $\boldsymbol{\theta}$ (°)	Stiffness Coefficient, R_0 [*lbf*] or [*N*]	Hardening Coefficient, R_∞ [*lbf*] or [*N*]	Hardening Exponent, *b*
0	9.00	10.0	290
15	10.0	4.00	180
30	20.0	2.20	135
45	238	1.00	1000
60	242	1.00	220
75	550	3.30	250
90	145	15.0	120

conjunction with the single wide tensile test results in the elasto-plastic region. The Voce model proves very capable of describing the hardening behavior through the ultimate tensile strength for this class of material, particularly at the main material orientations, as evidenced by the R^2 values reported in the figure, all of which are measured up to P_{uts}, the observed ultimate tensile load.

Chapter 5: Fractographic Analysis

5.1 Single Wide Specimens

The characteristics of the observed failure surfaces for the CRE-tested woven wire mesh single wide specimens were studied in an effort to gain insight into the failure mechanisms and local fracture evolution. Qualitative and quantitative observation of failure surfaces have been made by previous authors for this class of material [1, 18], and it has been shown to provide insight into wire and mesh behavior. This investigation revealed a strong dependence of fracture orientation and appearance on material orientation. Observations were made from detailed inspection of the failure surfaces post fracture for each material orientation tested, with focus on the degree of wire pull-out (fraying), number of fractures, waviness of the fracture surfaces, orientation of the fracture with respect to loading, and the direction of fracture propagation. Figure 5.1 shows the failure surface of each orientation in both wide and close views, along with respective fracture angles, θ_s, with respect to the loading axis.

The warp (0°) orientation fractured with a considerable degree of fraying and fracture surface waviness. Failure occurs in the warp wires only, with very little if any load being transferred to the weft. As the warp wires deform and eventually fail, frictional forces between the warp wires and the orthogonal weft wires force the weft wires to "pull-out" of the weave, causing the observed fraying. This orientation produced several areas of fracture, all of them with considerable waviness and distribution. This indicates that the evolution of plasticity is well distributed within the warp wires of the mesh, and that failure on the macro-level may be considered independent of position in

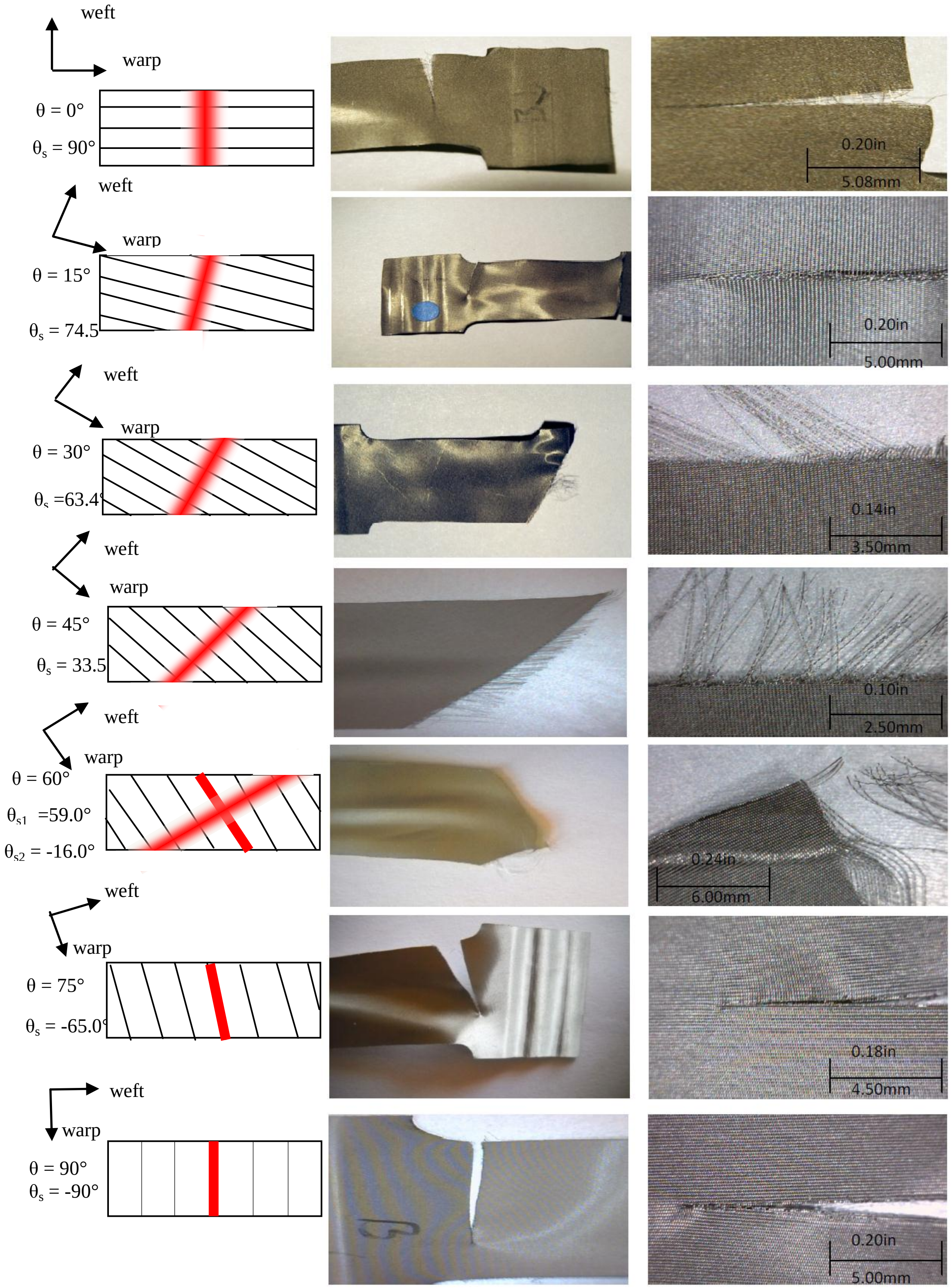

Figure 5.1: Fracture images of AR single wide 316L SS woven wire mesh at various orientations.

the warp direction. The initial observed fracture began at the edge of the sample and progressed inward as adjacent warp wires failed and unloaded, forcing neighboring wires to accept more load. Ultimately, a uniform strain evolution in the warp wires allows for a relatively slow unloading of the material, with failure occurring in the warp wires, and evolving orthogonal to the loading direction.

Failure in the weft (90°) orientation is much more concentrated than the warp (0°) case. No wire fraying is observed, and fracture propagates through the material quickly and in a straight path. Fracture occurred completely and instantly in two locations on the sample, both with identical features. The appearance of this failure surface indicates that the material evolved uniformly, but in a concentrated location of wire contact. Again, the failure surface is orthogonal to the loading direction, and the fracture initiates at the edge of the sample.

Intermediate orientations show combinations of the failure mechanisms associated with the warp (0°) and the weft (90°). Shear coupling of the off-axis specimens leads to the formation of shear stresses in the uniaxially loaded samples [14], and indication of this can be observed from the high degree of weft wire fray in 30°, 45°, and 60° samples. This phenomenon also produces a small degree of sample waviness attributed to shear forces that cause the wires to rotate slightly about their contact points. Also observed was a tendency for the failure orientation to differ somewhat from the orthogonal orientations found in the warp and weft. The 60° orientation marks a clear transition in the dominant mesh behavior, showing two distinct failure planes, each indicative of either a warp or a weft dominant wire failure. It is noted that observed transition to weft dominate failure characteristics at the 60° orientation is supported by Eq. (1), which calls for the weft wires to become active in the loading at 59.1°. The exact point of transition is of great interest to future study, and may serve as a benchmark for users of this material to develop the optimum material orientation for their respective application. Multiple but identical failure surfaces formed in the 15° and 75° orientations, each with two fractures on opposite ends of the sample. The remaining off-axis orientation displayed only one failure surface.

Results of fractographic analysis leads to the conclusion that there are two modes of mechanical rupture for this class of material. The mode of fracture is highly dependent on the orientation of the woven wire mesh with respect to the loading axis, and can be classified as either warp dominant (fraying) type fracture, or weft dominant (concentrated) type fracture. The two modes can be characterized by the size and waviness of the observed fracture surface, as well as the degree of wire pull-out upon fracture, and the location of the process zone. Fraying type fracture indicates that failure ultimately occurred in the warp wires, and typically is accompanied by a largely distributed material process zone and a wavy rupture surface. The distributed fracture surfaces indicates that strain development is dispersed throughout the structure, while wire fraying indicates that frictional forces are significant enough to pull wires out of the weave upon rupture. Concentrated type failure occurs only in orientations where the weft wires are dominant in gauge to gauge wire count. This indicates that the observed sharp and clean fracture zones at 60°, 75° and 90° (weft) orientations are a result of fracture in the weft wires. This rupture mode shows no wire fray, and no waviness, stemming from the concentration of strain development at points of contact between warp and weft wires.

Wire contact zones generate high localized stresses, ultimately leading to the observed localized rupture in weft type failure.

5.2 Double Wide Specimens

In a similar manner to the single wide specimens, double wide specimens were inspected post-rupture to classify their fracture characteristics. Properties such as fracture location, the degree of wire fray, the orientation of the fracture, and the degree of concentration of the process zone were analyzed for each orientation. Comparisons to the single wide specimens also provides insight into the degree that wire cut off and specimen aspect ratio affect the fracture surface. Images of the double wide fracture surfaces are presented in Fig. 5.2, where all symbols are as in Fig. 5.1.

Inspection of the fractured specimens in the main material orientations reveals very little difference from the behavior observed in the single wide specimens. In both the warp and the weft axes, fracture occurs perpendicular to the loading direction. The warp (0°) orientation displays a frayed fracture zone, again the result of weft wire pull-out. The rupture is somewhat more concentrated in the double wide specimen, however mesh rupture does occur in two distinctly different places on the weave; in the filleted section of the sample, as well at the boundary of the wave grips. It is suspected that if the specimen failed in the gauge section as intended, a more distributed process zone would have resulted. It is also noted that failure into the grips, both in single and double wide samples, could be arresting the propagation of the initial rupture, causing the secondary loading and yielding observed in Fig. 3.2 at the 30° and 45° orientations. The weft (90°) orientation displays fracture surfaces very similar to the single wide observations. Fracture is very straight and concentrated, and no wire fray is observed. Again fracture occurs in two places, each propagating from opposite sides of the specimen, but with nearly identical properties. This leads to the conclusion that, as in the single wide specimens, plasticity is concentrated in areas of contact with the orthogonal warp wires, leading to concentrated zones of fracture. Again, fracture of the double wide weft (90°) sample occurs close to the filleted region.

Off-axis specimens also failed quite similarly to their single wide counterparts, with only a few exceptions. The double wide specimens display wire fray through the 45° orientation, and have more dispersed rupture zones. Starting at 60°, the fracture surface begins to take on the characteristics of weft dominant fracture, showing no wire fray and very sharp fracture surfaces. It is noted that the transitional fracture observed at 60° in the single wide specimens is not seen in the double wide specimens. Contrary to this, transition is observed in the 45° orientation, where a very small weft dominant fracture is observed along with a more pronounced weft dominate fracture. This indicates that, as predicted by Eq. (1b), the weft wires are involved in the uniaxial loading of the double wide specimens at a lower incision angles than the single wide specimens. The fracture orientation for the double wide specimens tends to follow the orientation of the specimen similar to the single wide results, i.e., at 15° material orientation, the orientation of the fracture is at nearly 75° from the loading direction. The largest deviation from this behavior was observed in the 30° orientation, where the fracture occurs at an angle of 67.4° from the loading direction.

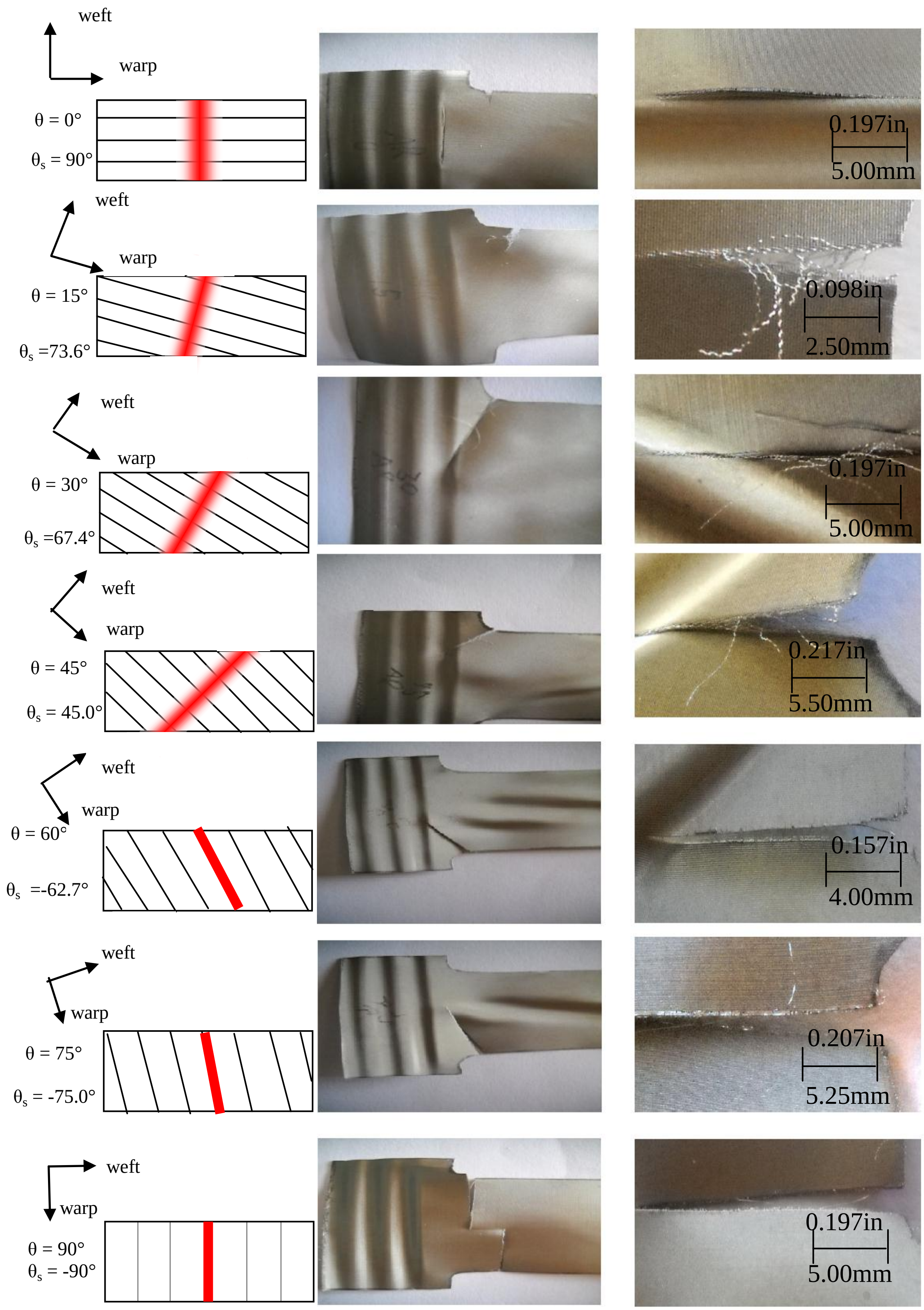

Figure 5.2: Fracture images of AR double wide 316L SS woven wire mesh at various orientations.

Chapter 6: Damage Modeling

6.1 Ratcheting Experiments

Ratcheting experiments on the double wide AR test specimens provide high resolution data regarding the change in stiffness of the material as it was loaded and unloaded in a series of several ratcheting cycles. Load-displacement data was collected for each cycle, shown in Fig. 6.1. The various double wide responses show good agreement with the single wide curves in terms of loading and unloading slopes, and general curve shape, with only notable difference in appearance being the lack of secondary yielding at all orientations. The ratcheting cycle displacement rate was controlled for both loading and unloading phases in an effort to mitigate any rate dependant effects on the mechanical response, i.e.,

$$\delta(t) = 0.00032t + \left[\frac{0.012}{a}\left[(t+7) - a\left\lfloor\frac{(t+7)}{a} + \frac{1}{2}\right\rfloor\right](-1)^{\left\lfloor\frac{(t+7)}{a} - \frac{1}{2}\right\rfloor}\right] + 0.005 \qquad (6)$$

Here, $\delta(t)$ represents a math model of the applied ratcheting cycle, where a = 7.75 represents half of one period, t is measured in seconds, and δ is provided in inches.

Investigation of the double wide ratcheting test results reveals that hysteresis loops develop during each ratcheting cycle. Hysteresis present in the elastic region indicates energy losses in the material not attributable to plasticity, providing some insight into the degree of non-recoverable wire sliding and frictional rubbing that occurs in stage 1 loading. To quantify the energy losses present in these loops, trapezoidal integration was performed at load cycles before yield, at half of the ultimate strength, and at the ultimate tensile strength for warp (0°), weft (90°), and 45° orientations, i.e.,

$$E_h = \int_a^b L(\delta)_{\delta:\, a\to b} - L(\delta)_{\delta:\, b\to a}\, d\delta \qquad (7)$$

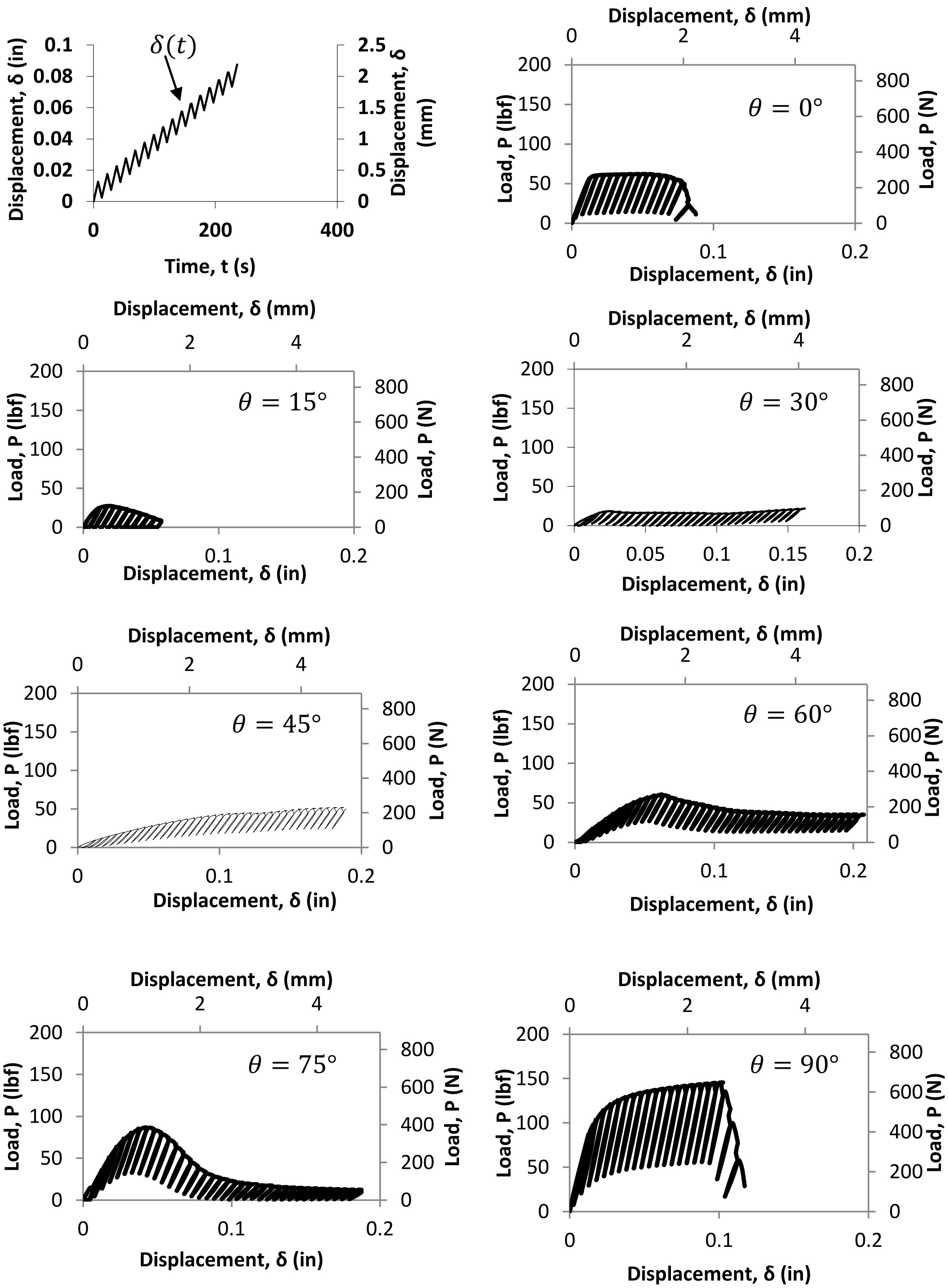

Figure 6.1: Mechanical response of 325x2300 316L SS woven wire mesh under ratcheting type tensile testing at various orientations.

Here, E_h is the hysteresis energy, and $L(\delta)$ is the load versus displacement response over a ratcheting cycle from point a to point b as indicated on Fig. 6.2b. As shown in Fig. 6.2, maximum hysteresis energies were observed in initial cycles of each orientation, with the weft (90°) having the largest energy at 4.4×10^{-3} ft-lb (5.9×10^{-3} J). Little difference was observed between the initial hysteresis energies of the 45° and the warp (0°) orientation, each with losses of 9.1×10^{-3} ft-lb (1.2×10^{-3} J). In general, as the material evolves in each orientation, frictional hysteresis is replaced by plasticity, and the observed hysteresis energy decreases. Minimum values occurred at the ultimate strength for each orientation, again with the weft (90°) displaying the largest energy loss of 2.2×10^{-3}ft-lb (2.9×10^{-3} J). The 45° orientation possessed hysteresis energy of 2.5×10^{-4} ft-lb (3.3×10^{-4} J), while the warp (0°) orientation remained more constant, displaying an energy loss of 7.5×10^{-4} ft-lb (1.0×10^{-3} J). These results indicate that the energy lost during elastic loading is significantly higher in the weft (90°) direction of this material than in the warp (0°) direction (131.25% difference at initial stage), illustrating how the degree of frictional wire interaction varies between the main weave orientations.

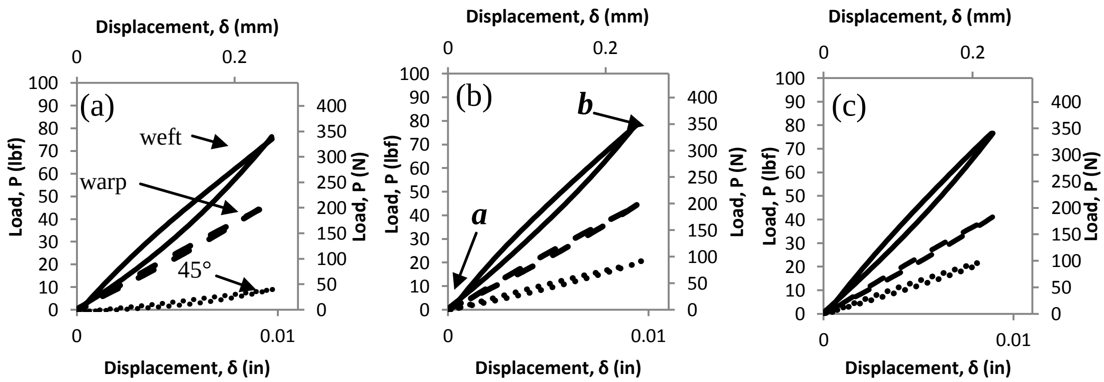

Figure 6.2: Hysteresis loops of 316L SS woven wire mesh as various orientations. (a) Initial cycle, (b) half of UTS cycle, (c) UTS cycle.

6.2 Continuum Damage Model

The use of ratcheting type tensile tests on the double wide samples allowed for the formulation of a damage model for the 325x2300 316L SS woven wire mesh based on the degradation of its elastic modulus. Damage is a physical form associated with the irreversible accumulation of microstructural defects in the material. It affects mechanical properties, specifically the elastic modulus, and so may be defined as the change in elastic modulus due to the onset of plastic strain. This can be observed as changes in the stiffness of the mesh sample as the test progresses through ratcheting cycles, ultimately ending in the failure of the specimen. Figure 6.3 illustrates the evolution of the elastic modulus throughout the loading cycles in each material orientation. A damage model was sought in an effort to eventually develop a failure criterion for the 325x2300 316L SS woven wire mesh based on Continuum Damage Mechanics (CDM). Such a model has been developed based on the fundamental isotopic damage theory, which requires the introduction of a damage variable *D*, defined by the change in elastic modulus after plastic deformation by

$$D_\theta = 1 - \frac{E_{D\theta}}{E'_\theta} \tag{8}$$

Here, $E_{D\theta}$ is defined as the damaged elastic modulus for each respective orientation and E'_θ is the initial elastic modulus for each respective orientation. The independent treatment of each orientation simplifies the damage modeling by alleviating the need for an orthotropic model, and so only the elastic modulus in the orientation in question need be considered. The damaged modulus, $E_{D\theta}$, was modeled for each orientation via a curve fit to the experimental data producing a function dependent on the plastic displacement,

$\delta_{pl}(t)$, the observed undamaged elastic modulus, E'_{θ}, and several curve fitting parameters, e.g.

$$E_{D\theta} = E'_{\theta} - \frac{m}{e^{c\delta_{pl}(t)}}\delta_{pl}(t) + E_m\left[1 - e^{-b\delta_{pl}(t)}\right] \tag{9}$$

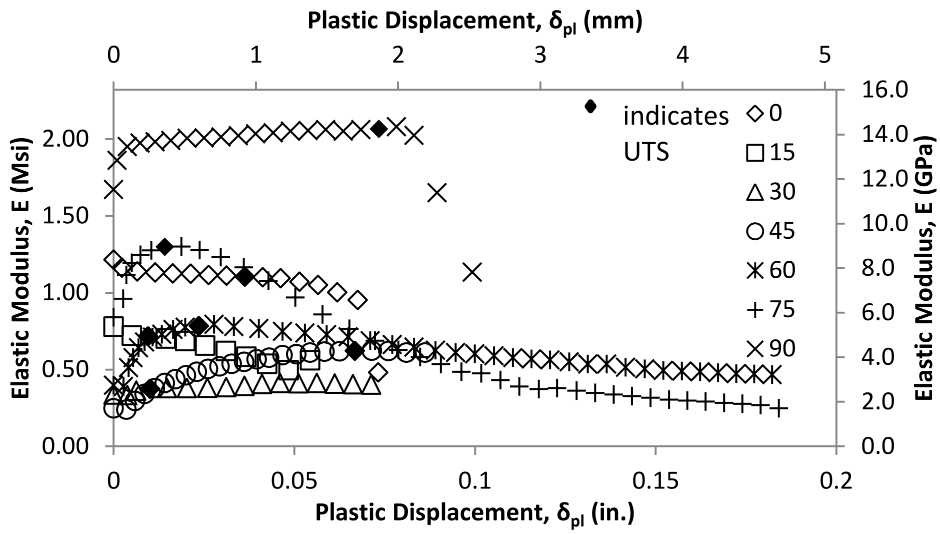

Figure 6.3: Evolution of the elastic modulus of double wide 325x2300 SS 316L woven wire mesh subject to ratchet type tensile testing.

To provide consistency and synergy to this relationship, the damage formulation was designed after Eq. (5) and the Voce model. Here, E_m, the modulus coefficient, represents the difference in elastic moduli from the initial value, E'_{θ}, to the first inflection point of the model. Also, *m* and *c*, the slope coefficient and exponent respectively, are curve-fitting parameters that control the rate of elastic moduli change after the first inflection point, while *b*, the modulus exponent, influences the initial curvature of the model. The reliance model was fit to data normalized by the initial elastic modulus for each respective orientation, such that E'_{θ} = 1 for every orientation. As shown in Fig. 6.4, this model proves quite capable of capturing the gamut of behaviors of the elastic modulus of this material throughout its entire evolution, and when using the parameter values given in Table 8, provides good damage results when compared to experimental data. It must be noted that the resiliency model presented as Eq. (9) is highly limited in its scope, and cannot be assumed valid in general cases of loading, nor with displacement rate other than that defined by Eq. (6). Future work is planned to develop this model into a more general constitutive based formulation, and to alter the parameters to allow the model to be a function of plastic strain rather than plastic displacement. With further development, the designer could potentially use Eq. (9), along with a generic displacement history, to predict conditions conferring optimal performance of the woven wire mesh. Future testing required to develop this model further may include both in phase and out of phase biaxial ratcheting.

Investigation of the elastic moduli trends shown in Figs. 6.3 and 6.4 reveal an unusual increase in elastic moduli through ratcheting cycles for several weft dominant orientations. This indicates a significant amount of material stiffening, particularly in the 45°, 60°, and 75° orientations, leading to the observation that cycling the material slightly into the plastic range ($P < P_{UTS}$) could be used as a potential strengthening mechanism for the woven wire mesh at these orientations. This stiffening behavior produces negative damage values when Eq. (9) is employed in its current form, but it is noted that the conventional definition of damage is satisfied with this method.

Table 6.1: *Elastic modulus degradation model parameters for 316L woven wire mesh*

Orientation, θ (°)	Slope Coefficient, *m*	Modulus Coefficient, E_m [*ksi*] or [*MPa*]	Modulus exponent, *b* [1/*in*] or [1/*mm*]	Slope Exponent, *c* [1/*in*] or [1/*mm*]
0	0.003	-0.100	150	-104
15	1.00	-0.100	100	-36.0
30	-36.0	-0.200	225	29.5
45	-88.0	-0.350	500	17.2
60	7.00	1.150	160	1.50
75	28.0	1.200	100	5.60
90	0.00001	0.220	300	-133

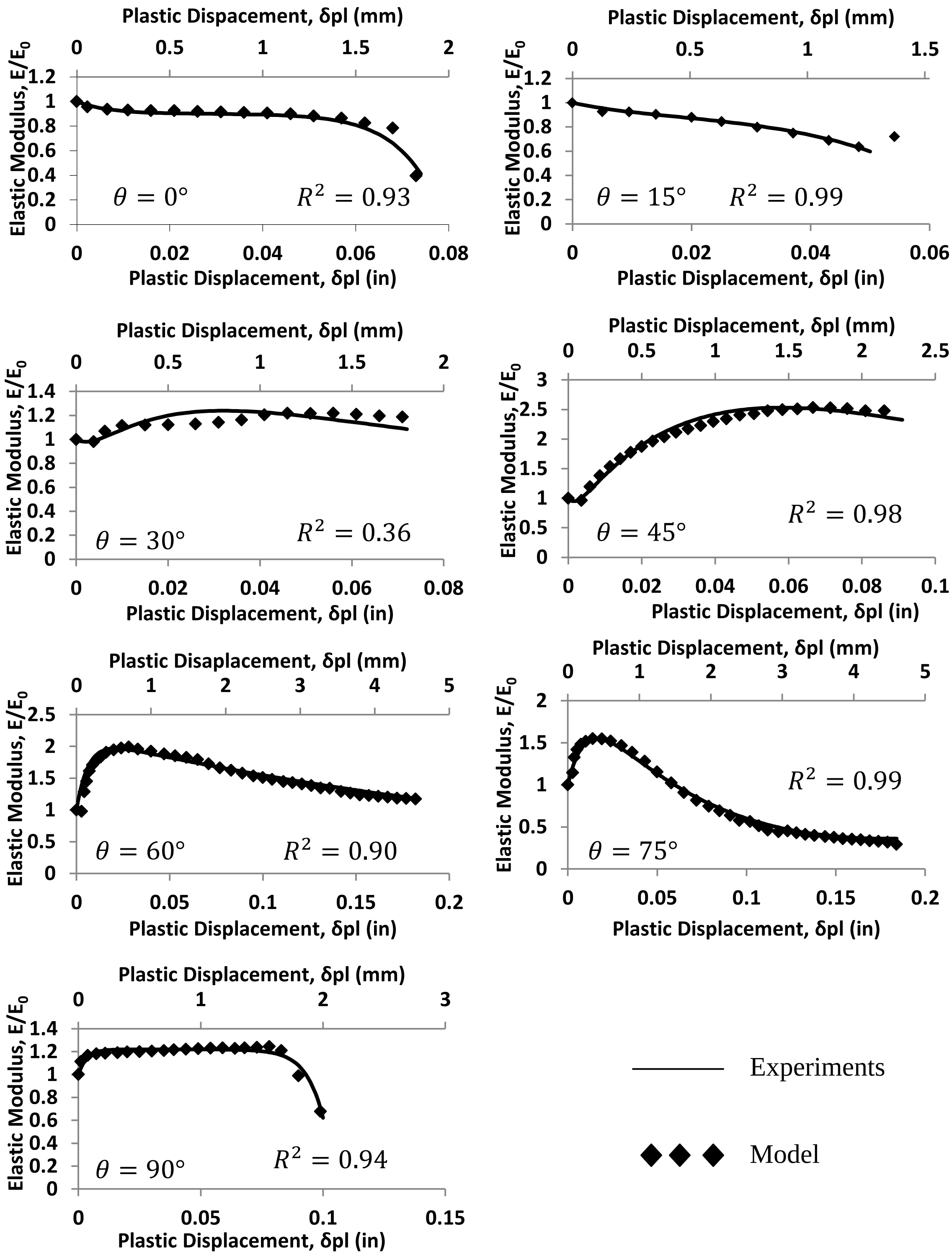

Figure 6.4: Actual and correlated elastic modulus evolution for 325x2300 316L SS woven wire mesh at various orientations.

Chapter 7: Numerical Modeling

The use of the finite element method to study this class of materials is ideal in that it gives the ability to correlate the meso-scale stress or strain distributions to the macro-scale behavior of the woven mesh. Numerical simulations were conducted using 3D finite elements with full contact definitions in order to obtain the highest amount of accuracy and resolution possible. While painstaking in practice, the definition of realistic frictional contact elements to handle the wire contact rather than idealized node to node springs or rigid elements provides for a fully functioning model capable of handling any combination of in-plane loading. Numerical simulations were carried out to compare the development of stress on the meso-scale (individual wires), to the stress calculated using the homogenized continuum assumption, and contour plots are provided showing how plastic strain accumulates in the main axes of the weave.

7.1 Model Development

The woven wire mesh was modeled using ANSYS multi-physics FE software. The rendering used to generate the finite element mesh is shown in Fig. 1.1a. With the model satisfactorily defined, the geometry was meshed using ANSYS Workbench, which provided a sufficiently sophisticated GUI based FEM environment to carry out the simulations. The simulations where performed in a number of steps, first arriving at an optimal mesh that aided both convergence and stress distribution continuity. The initial mesh consisted of 20 node hexahedron elements (SOLID186), as well as sufficient 3D contact elements (TARGE170 and CONTA175). The overall node count was 28,769. An augmented Lagrange contact formulation was utilized to help stabilize the contact model, with adjustments being made to the contact stiffness to aid in convergence. The contact parameters used in the model included a static friction coefficient, contact stiffness factor, and a scoping region used to determine if contact was taking place (pinball region). Two different contact definitions were utilized; one to define warp to weft wire contact, and the other to define weft to weft wire contact. Weft to weft contact was assumed to have more relative wire sliding than normal force, and so required a small contact stiffness factor and friction coefficient to obtain convergence, with values of 0.01 and 0.02, respectively. Warp to weft contact was defined with a stiffness coefficient of 0.70, and a more realistic friction coefficient of 0.50. ANSYS was allowed to automatically determine the optimal pinball region for the contact, and was allowed to turn symmetrical contact regions off in an effort to reduce contact chatter and aid convergence. Reduction in contact stiffness results in the need to increase the stiffness of the constitutive matrix employed by the numerical model. The resulting multi linear kinematic hardening (MKIN) model used for each wire (warp and weft) is therefore not indicative of the actual wire properties, but is instead tailored to match the CRE tensile test results from warp (0°) and weft (90°) orientations. Figure 7.1 illustrates the plastic strain hardening response employed in the FEM for the woven wire mesh. The material properties given to each wire in the model are provided in Table 7.1. Note the difference between the warp and weft material properties used in the model, with the weft wires being given far more strength and stiffness to fit the CRE test results, as well as differences between model properties and the published properties for 316L SS in Table 1.1.

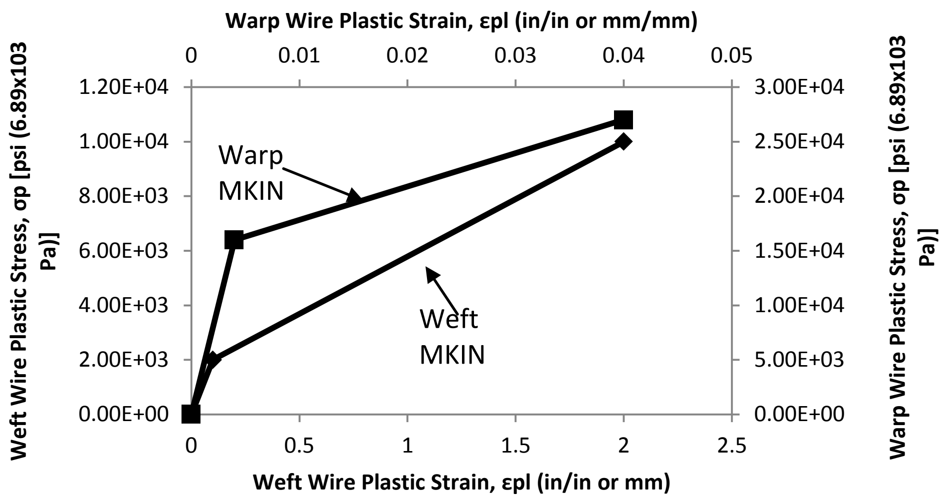

Figure 7.1: Multi-linear kinematic hardening models used to simulate the hardening behavior of the warp wires and the weft wires for the 316L SS Woven Wire Mesh.

Table 7.1: *Material properties of warp and weft wires as defined in FEM constitutive model*

Property		Elastic Modulus, E	Yield Strength, S_y	Ultimate Tensile Strength, *UTS*	Density, ρ	Poisson's Ratio, v
Warp	SI	51.7 GPa	400 MPa	586 MPa	0.008 g/mm^3	0.3
	English	7.5 Msi	58.0 ksi	85.0 ksi	0.289 lbf/in^3	0.3
Weft	SI	448 GPa	1720 MPa	1709 MPa	0.008 g/mm^3	0.3
	English	65 Msi	250 ksi	260 ksi	0.289 lbf/in^3	0.3

7.2 Boundary Conditions

7.2.1 Main Axes

With the intent of the simulations being to mimic the tensile testing to the highest degree possible, a set of boundary conditions were generated to handle both 0° and 90° simulations, in which no shear displacement components were present. Loading was applied to the FEM via incremental linear displacements, much like the CRE tensile experiments. The magnitude of the applied displacements, and the model results, are related to the experimental samples via simple geometric relationships, i.e.,

$$F_c = F_{sim}\left(\frac{W_{exp}}{W_{sim}}\right) \tag{10}$$

$$D_c = D_{sim}\left(\frac{L_{exp}}{L_{sim}}\right) \tag{11}$$

Each relation is used to scale simulation results to the experimental results, where F_c and D_c are the scaled simulation force and displacement, F_{sim} and D_{sim} are the force and displacement from the model, L_{sim} is the length of the model in the loading direction, W_{sim} is the width of the model orthogonal to the loading direction, and L_{exp} and W_{exp} correspond to the gauge length and width of the test specimens, respectfully. The use of displacements helps to ensure model stability, and that the simulations results are easily comparable to the experimental results. Figure 7.2 shows the boundary conditions applied to the model in the weft (90°) orientation, and by rotating the geometry 90°, the boundary conditions utilized on the warp (0°) direction simulations can be ascertained. Note that the frictionless supports act as symmetry constraints, and allow for full realization of Poisson’s effect and wire tightening at the end locations, providing a realistic material response.

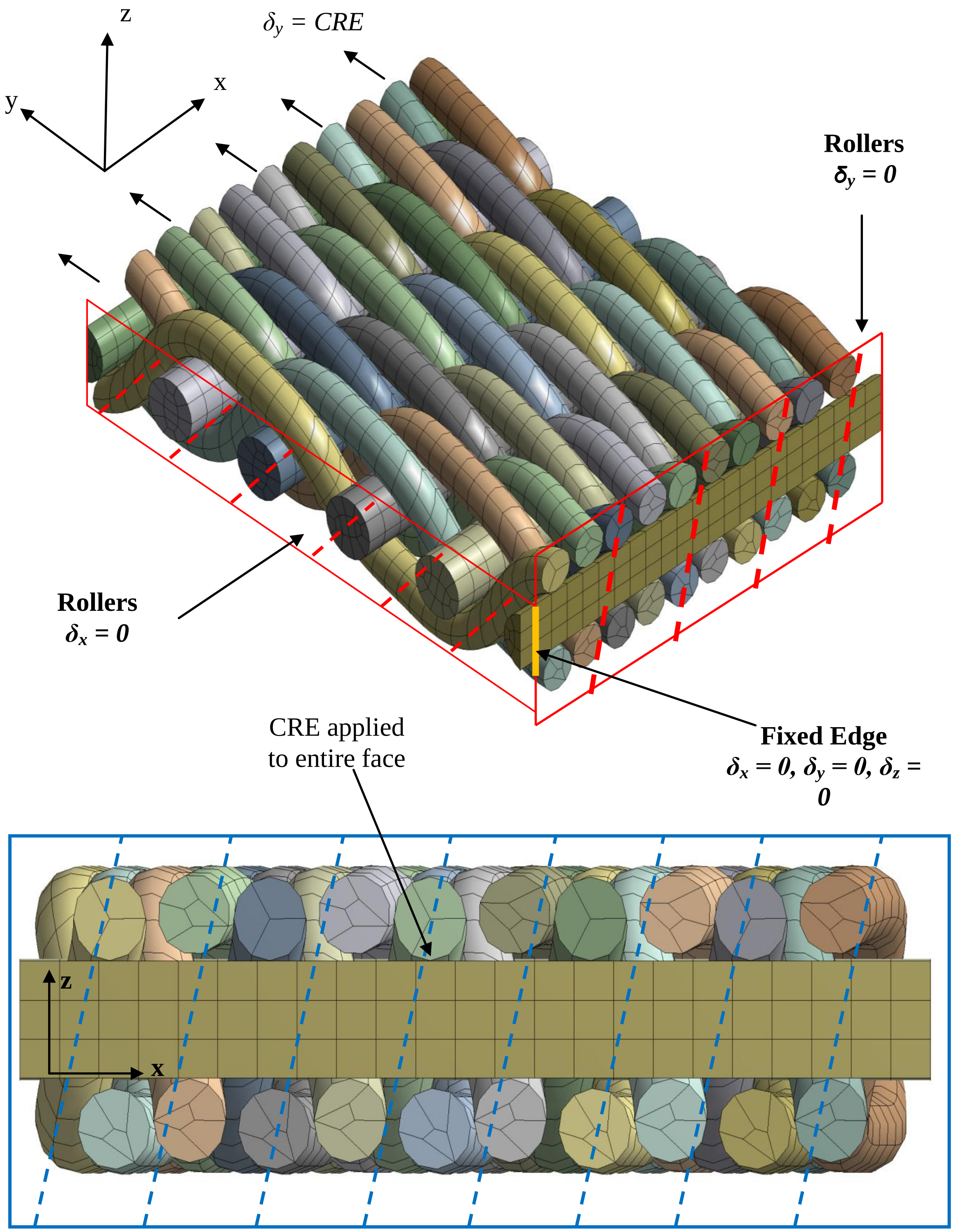

Figure 7.2: Finite element mesh of 3D CAD model used to facilitate the numerical modeling of the 316L SS woven wire mesh with boundary conditions used to simulate the tensile testing of the weft (90°) orientation sketched.

7.2.2 Off-Axis Boundary Conditions

Intermediate orientations were also simulated in an effort to fully characterize the meso-scale orthotropic behavior of the woven wire mesh. To accommodate this modeling without the need to formulate complex boundary conditions, the CAD geometry was simply cut into the proper orientation and then re-meshed. This method has many advantages that make it an ideal approach. The main advantage to physically rotating the model geometry is that simple frictionless supports, identical to the ones used to constrain the main axes models, can be employed. Also, this method requires significant pre-processing time for only half of the orientations, as the boundary conditions can simply be rotated 90° degrees to achieve the complimentary offset angle, i.e., the 15° model can also be used to simulate the 75° case by changing the displacement surface. An example of such a rotated model and the associated boundary conditions is illustrated in Fig. 7.3, which shows the 60° case.

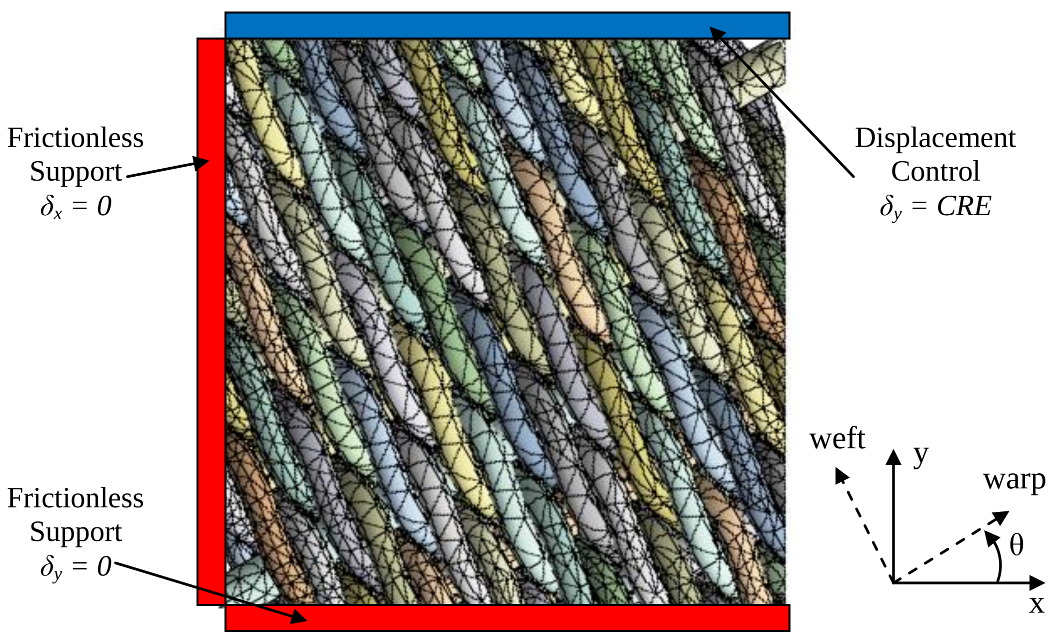

Figure 7.3: Off-axis boundary conditions and finite element mesh used to simulate 60° orientation

Note that mesh has been refined for the off-axis cases, and has been converted to non-linear tetrahedrons rather than hexahedral elements. This mesh exhibits better convergence and less stress oscillation in the off-axis cases than the hexahedral dominant mesh use in the main orientations. The node count in the refined mesh was 45,000 nodes.

7.3 FEM Results

7.3.1 Main Axes

Modeling efforts began in the main material orientations with the goal of optimizing the material model and perfecting the model inputs. Figure 7.4 shows the results of the main axes simulations with respect to the CRE tensile tests.

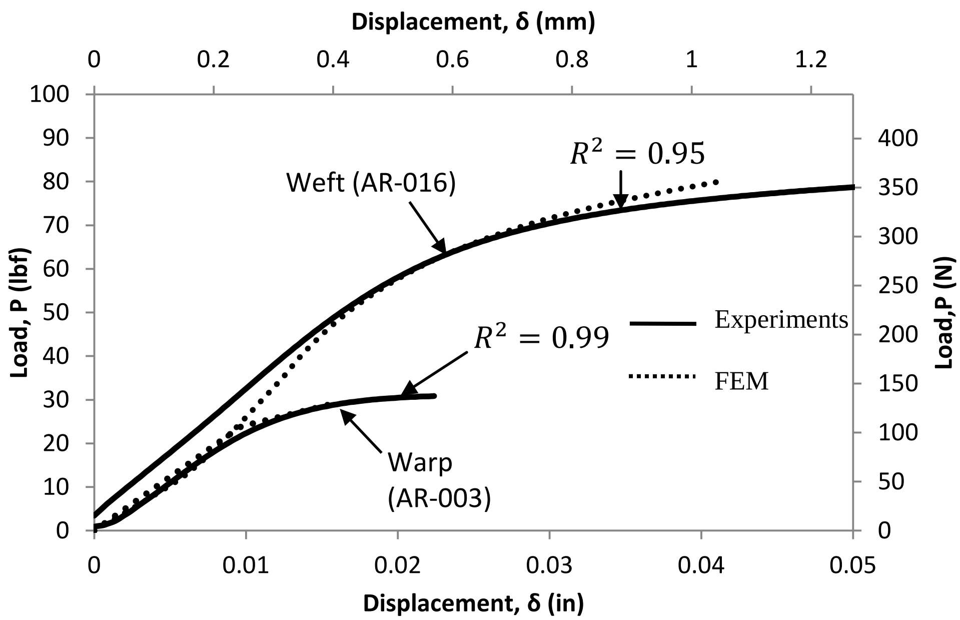

Figure 7.4: The elastic-plastic response of the Finite Element Model as compared to the mechanical response of the 325x2300 316L stainless steel woven wire mesh subject to tensile testing in the warp (0°) and weft (90°) orientations.

Error in stiffness and yield strength of the simulation results is less than 10% with respect to the single wide experiments. The greatest load prediction error occurs in the weft (90°) orientation in the linear-elastic region at 18%; however the critical elasto-plastic region shows error of less than 5%. These results validate the mechanical model used to simulate the woven wire mesh, and justify the use of contour plots to study meso-level material behavior.

To further investigate the relationship between meso-scale and macro-scale behavior, wire level stress-strain is compared to macro level stress-stain for the material. The macro-scale stress-strain response utilizes the homogenized continuum assumption, and is calculated by simply dividing the force reaction from Fig. 7.4 by the homogenized cross sectional area as defined by Fig. 1.1b. The strain is calculated as macro strain in all cases (meso-scale and macro-scale), again by simply diving the applied displacement by the initial model length. The wire scale stress state is somewhat complex, consisting of multiple components. To address this, the Von Mises state is used to compare the wires to the macro homogenized stress state, which only consists of a normal stress. Figure 7.5 shows the stress-strain response of the homogenized body, as compared with the stress-strain response of individual warp and weft wires. The wire stress values are taken from sections of nodes indicated by stress contour plots to be critical regions. Several nodal outputs were taken in the critical region of a centralized wire to avoid the effects of the boundaries. In this way, the stress curves reported indicate the progression of the maximum regions of stress within wires away from the boundaries. The critical regions, without exception, are areas of contact, typically where the highest degree of crimp interchange occurs between the wires. Investigation of Fig. 7.5 reveals that the orientation of the mesh highly influences the stress developed in either the warp or the weft wires. The macro-scale response in the main material orientations is dominated by the wire running in that direction, and tends to fall in-between the response of warp and the weft wires. It is noted that meso-scale stress results are highly dependent on the area in the wire chosen for analysis; however, regions were chosen consistently for each wire and orientation as described, allowing for the comparison of the results.

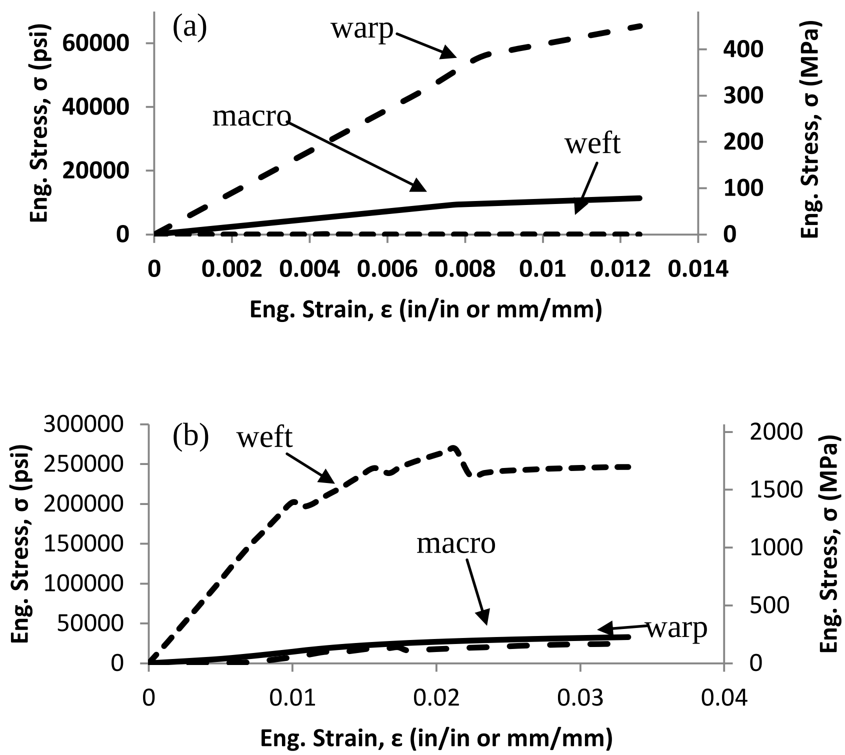

Figure 7.5: Numerical stress-strain response of (a) warp (0°) and (b) weft (90°) axes of 325x2300 SS 316L woven wire mesh showing meso-scale response in the warp and weft wires compared to the homogenized macro-scale response.

7.3.2 Off-Axes FEM Results

With the numerical model behaving satisfactorily in the main material orientations, and the material model adequately defined as provided in Table 7.1 and Fig. 7.1, simulations were able to proceed to the off-axis orientations. The geometry was cut and meshed as illustrated in Fig. 7.3, and controlled displacement simulations were executed in a similar fashion to the main material orientations. Macro-scale load – displacement curves, shown in Fig. 7.6, were collected for each orientation to quantify the goodness of fit for each simulation. The material re-orientation method used to model the off-axis loading modes proves an acceptable method, as evidenced by the exceptional R^2 values provided in the figure, all calculated through the extent of the numerical response.

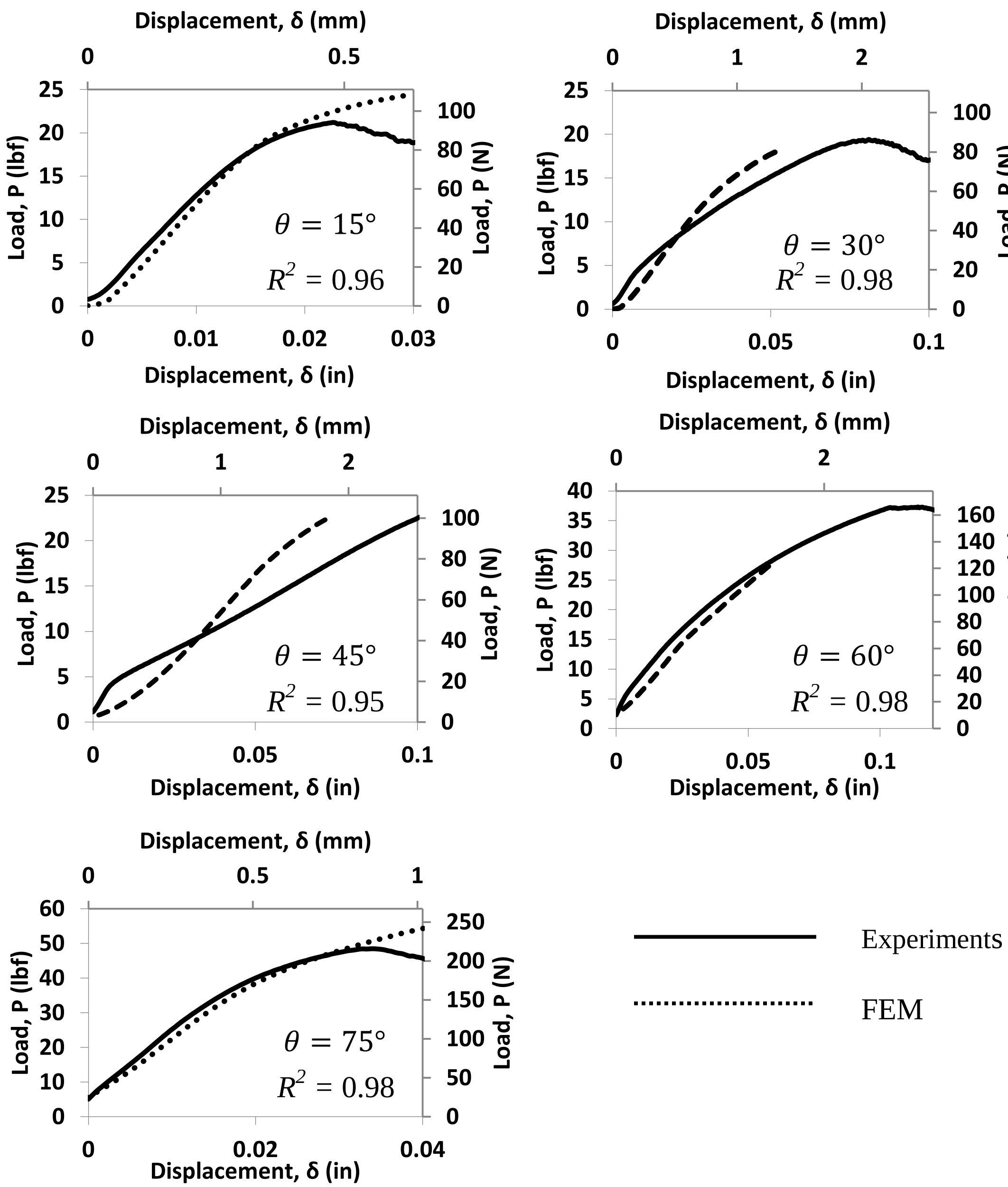

Figure 7.6: Macro-scale load - displacement curves from off-axis numerical simulation of 325x2300 SS316L woven wire mesh compared with experimental results

Of great interest to this study is evolution of warp and weft wire loading as the material is re-oriented through 90°. It is clear from the experimental results that as the material is rotated from the warp (0°) axis through 90° to the weft axis, the mechanical behavior changes quite drastically. This is a function of both the effects of shear coupling and wire rotations, and the differing material properties of the warp (0°) and weft (90°) wire directions. To investigate how mesh orientation affects the degree of loading assumed by the warp and weft wires, the Von Mises stresses in each wire type are compared to the macro-scale stress response using the homogenous continuum assumption, as was done in Fig.7.5.

Investigation of Fig. 7.7, which shows the macro-scale stress compared with the wire level equivalent stresses, reveals that indeed the wire loading is dependent on mesh orientation. It is observed that as the material is rotated away from the warp (0°) orientation, weft wire loading increases from near zero initially, and does not cause weft wire yielding until the 45° orientation. Yielding of the weft wires in the 45° orientation is supported by the double wide fractography observations, in which transition to weft dominant wire failure was observed at about 45°. From 60° through the weft (90°) axis, yielding primarily occurs in the weft wires, which achieve stresses much higher than the warp wires. It is also observed that wire loads remain low for significant strain levels in the 15°, 30°, 45°, and to a lesser extent the 60° orientations, due to wire rotations and relative sliding that occurs between the wires during stage 1 loading. The observed stress oscillations in some orientations during wire hardening indicates that additional mesh refinement may improve results; however, the recorded trends tend to follow the defined material model, and so this oscillation is assumed to be negligible for the purpose of this study.

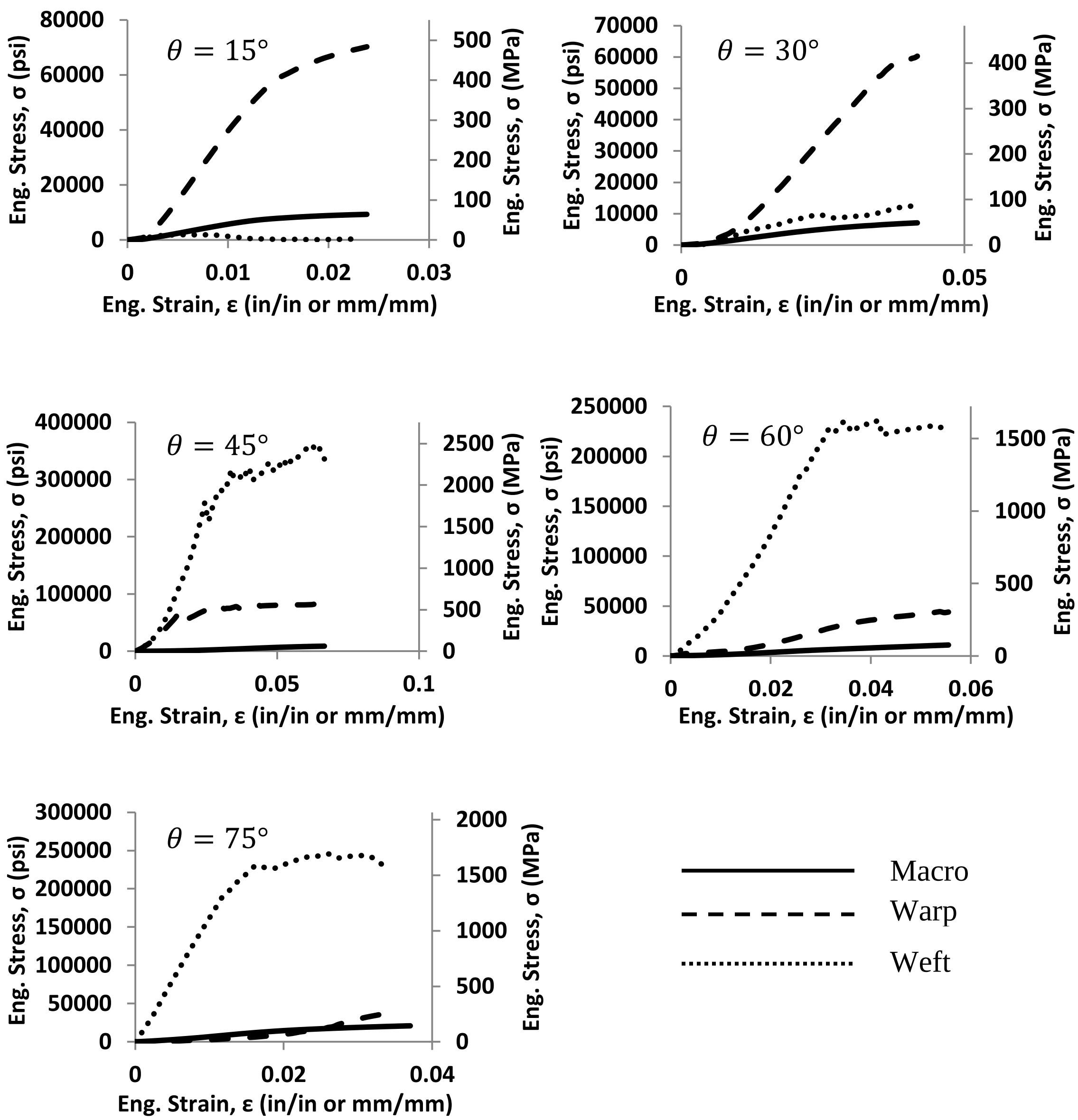

Figure 7.7: Numerical stress-strain response of off-axis oriented woven wire mesh showing meso-scale response in the warp and weft wires compared to the homogenized macro-scale response.

7.3.3 Plastic Strain Development in Main Axes

The exceptional fit of the load-displacement curves of the model with respect to the experimental data justifies the use of contour plots to investigate the development of plasticity in the wires. These efforts have been focused on the main material axes, which are representative of the two dominant fracture behaviors observed in the mesh. Modeling reveals that much of the load is indeed carried by the warp wires, even in the case of loading perpendicular to their running length, indicating that crimp interchange is a significant pathway for strain distribution throughout the wire mesh structure. Figure 7.8 provides contour plots of the plastic strain evolution of the main axes (warp and weft). These plots represent meso-scale plastic strains accumulated at key macro-level displacements, δ_A and δ_B, as indicated on Fig. 3.1a, effectively relating macro mesh behavior to meso wire behavior in the elasto-plastic region. Average plastic strain accumulation at these points is 0.0016 in/in (or mm/mm) for the warp (0°) orientation and 0.0021 in/in (or mm/mm) for the weft (90°) orientation at δ_A = 0.015in (0.381mm). At δ_B = 0.04 in (1.016mm), average plastic strain accumulation is 0.044 in/in (or mm/mm) in the weft (90°) orientation. These values are taken from centralized nodes of the mesh in order to mitigate boundary condition effects on the results. Plastic strain in the weft (90°) orientation tends to accumulate at the area of warp-weft contact, indicating that failure should occur along the warp wire orientation as observed in the experiments. The accumulation of plastic strain in the weft orientation also explains the uniform brittle-like failure that occurs immediately post ultimate tensile strength being achieved. The warp (0°) orientation develops strain in a much more uniform manner, distributed evenly over the warp wires only. Strain propagates as one would expect in a homogenous body, with

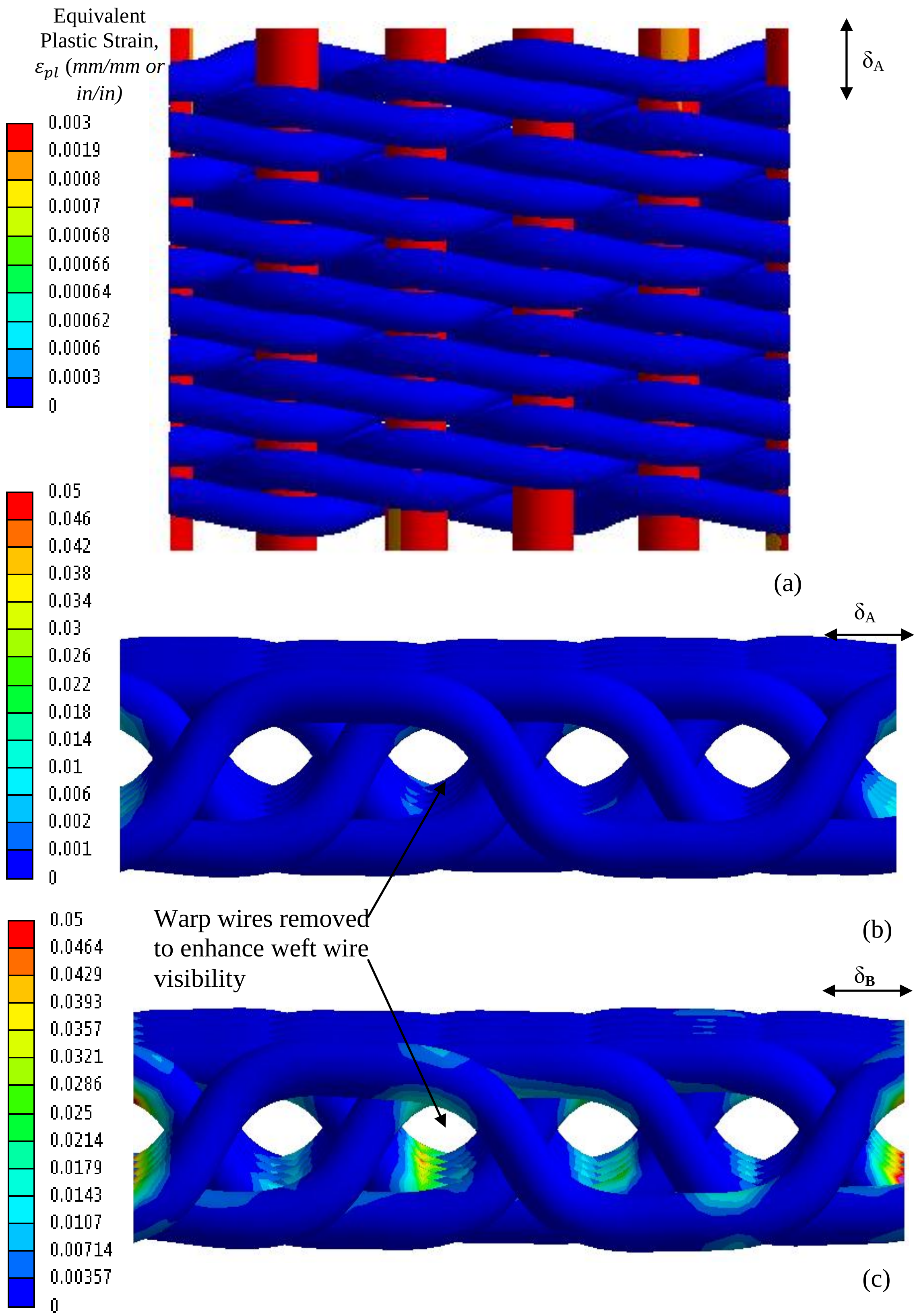

Figure 7.8: Equivalent plastic strain FEM contours of the 325x2300 316L SS woven wire mesh subject to tensile loading in the (a) warp (0°) directions, and (b-c) weft (90°) direction.

little gradient observed. This strain distribution also supports the gradual unloading observed for this orientation in CRE tests. Future modeling efforts are intended to expand the loading to general plane stress, including pure shear and bi-axial tension conditions.

Chapter 8: Future Work

A number of future experiments are planned to expand upon the work presented here. These future experiments include biaxial tension, biaxial tension with shear, and drape tests. The biaxial tension experiments will be conducted using a multiaxial test fixture designed and built by a senior design group at UCF. The tests fixture is capable of imparting a multitude of different load states on biaxial cruciform tests specimens using a conventional uniaxial testing machine. The test fixture design is provided below in Fig. 8.1. With this test fixture, it will be possible to subject the woven mesh material to the entire range of in plane loading modes, resulting in a more complete view of the mechanical behavior of this class of materials. Planned experiments also include biaxial ratcheting tests to help develop a better resilience model for this material. Also planned is a series of drape experiments which will be used to classify the drape coefficient of the woven wire mesh. The drape profile can be used to correlate several elastic properties, and will also serve as a gauge for the level of anisotropy of the material.

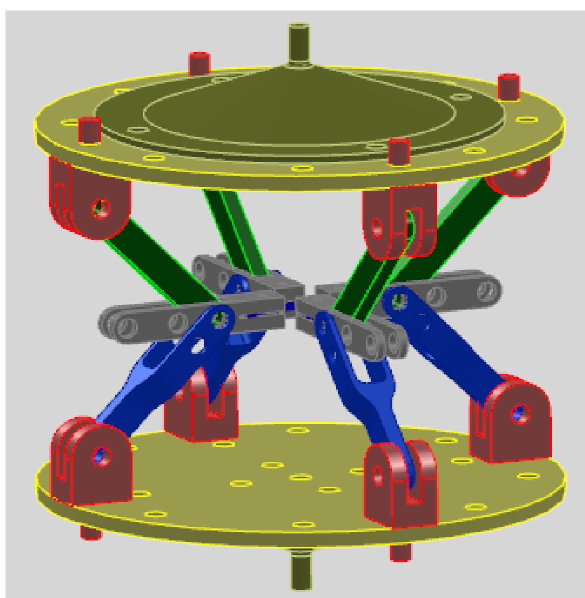

Figure 8.1: Multiaxial test fixture for biaxial and shear testing of fabrics.

Chapter 9: Conclusions

Extensive mechanical testing and material modeling has been carried out on a 325x2300 SS316L twill dutch woven wire mesh. Uniaxial tensile tests have been performed at various material orientations on several different material classes, providing high resolution data and a good understanding of the orthotropic material behavior of this material. In an effort to justify the macro-scale modeling of this material, several classic models gave been exercised with respect to the as-received (AR) mechanical data. Elastic, elasto-plastic, and hardening models have been applied to the material with excellent results. The orientation dependence of the elastic modulus has been shown to behave as expected for homogonous orthotropic materials. It has also been demonstrated that Hill's Analogy provides a reasonable model for the prediction of mesh yielding, and that the Voce hardening model provides excellent fit to the experimental results. These results suggest that classic macro-scale orthotropic modeling is sufficient to provide the designer with acceptable predictions of material behavior.

In an effort to investigate the macro-scale damage accumulation for this material subject to cycles of plastic deformation, a cumulative damage model was developed. Orientation dependant ratcheting type tensile tests were performed, and the progression of the material's elastic modulus through rupture was analyzed and modeled. The macro-scale damage model proved very capable of predicting the degradation in elastic modulus through rupture of this woven wire mesh material.

To further justify the use of macro-scale modeling to predict the behavior of this class of materials, a meso-scale finite element model was developed. This model incorporated wire scale representation of the woven mesh, with several weave periods included to help mitigate boundary effects. The response of the model in the main material orientations has been shown to closely follow the macro-scale response, indicating that wire scale behavior need not be considered when making macro-scale design considerations. The distribution of plastic strain was also studied via the finite element model, and it is demonstrated that the macro-scale mesh fracture behavior is related to meso-scale wire damage.

Based in the findings of this research, it is proposed that macro-scale modeling is a justifiable method to capture the mechanical behavior of this woven wire mesh material. The material behavior is in good agreement with elastic modeling, Hill's Analogy, and with Voce hardening. It is noted that the mechanical properties of this material are highly dependent on material orientation, with maxima tending to occur at the main axes.

APPENDIX

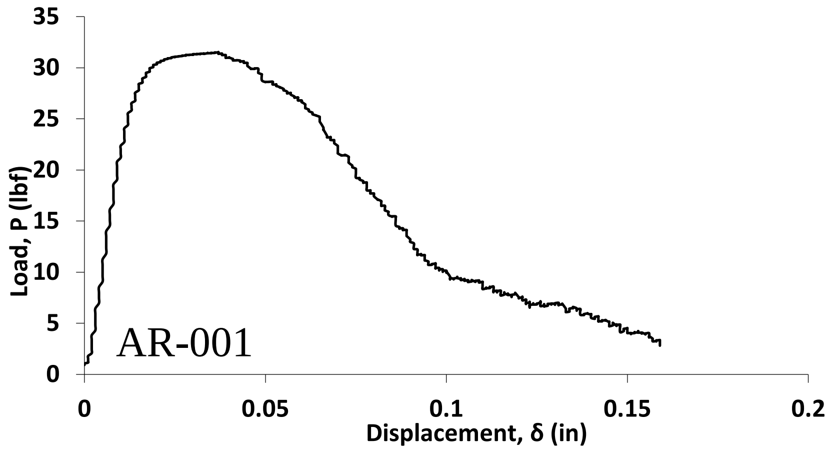

AR-001 Tensile Test Results

Stiffness (*lbf/in*)	2327
Yield Load (*lbf*)	26.8
Ultimate Load (*lbf*)	32.0

Specimen Details (AR-001)

Gauge Width, W_g (in)	Orientation, θ (°)	Pre-treatment Temperature, *T (°F)*	Heating Duration, *t* (s)	Cooling Environment	Fracture Location	Type	Process Zone
0.75	0 (warp)	N/A	N/A	N/A	*	*	*

**Specimen Lost*

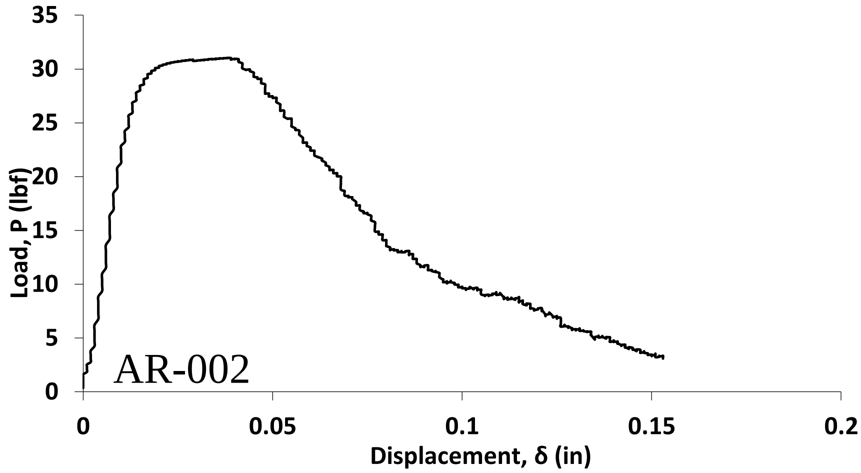

AR-002 Tensile Test Results

Stiffness (*lbf/in*)	2233
Yield Load (*lbf*)	25.0
Ultimate Load (*lbf*)	31.0

Specimen Details (AR-002)

Gauge Width, W_g (in)	Orientation, θ (°)	Pre-treatment Temperature, *T (°F)*	Heating Duration, *t* (s)	Cooling Environment	Fracture Location	Type	Process Zone
0.74	0 (warp)	N/A	N/A	N/A	Inside Gage	Side, 2 Places	Wide

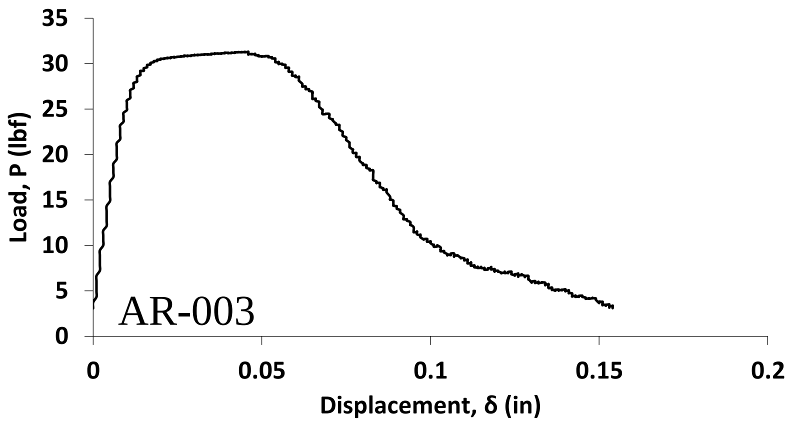

AR-003 Tensile Test Results	
Stiffness (*lbf/in*)	2513
Yield Load (*lbf*)	27.6
Ultimate Load (*lbf*)	31.3

Specimen Details (AR-003)

Gauge Width, W_g (in)	Orientation, θ (°)	Pre-treatment Temperature, *T (°F)*	Heating Duration, *t* (s)	Cooling Environment	Fracture Location	Type	Process Zone
0.74	0 (warp)	N/A	N/A	N/A	Inside Gage	Side and center, 2 Places	Wide

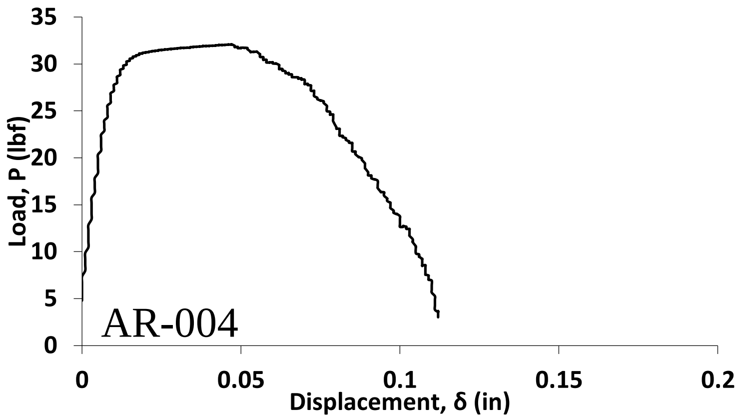

AR-004 Tensile Test Results

Stiffness (*lbf/in*)	2722
Yield Load (*lbf*)	28.2
Ultimate Load (*lbf*)	32.9

Specimen Details (AR-004)

Gauge Width, W_g (in)	Orientation, θ (°)	Pre-treatment Temperature, *T (°F)*	Heating Duration, *t* (s)	Cooling Environment	Fracture Location	Type	Process Zone
0.73	0 (warp)	N/A	N/A	N/A	Inside Gage	Side, 2 Places	Wide

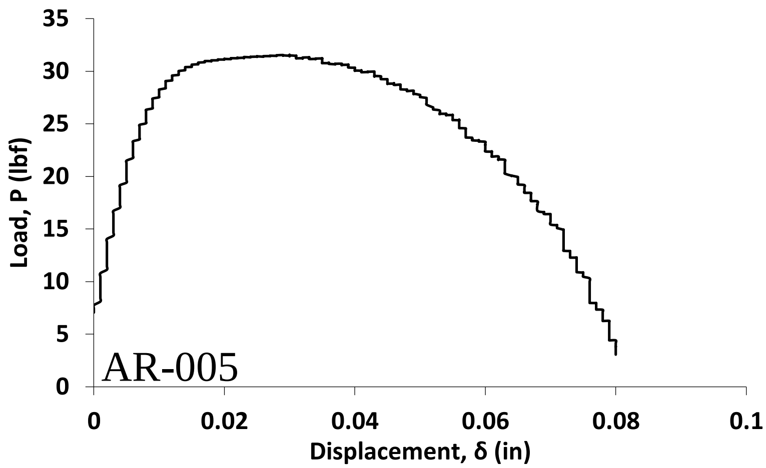

AR-005 Tensile Test Results

Stiffness (*lbf/in*)	2908
Yield Load (*lbf*)	27.0
Ultimate Load (*lbf*)	32.3

Specimen Details (AR-005)

Gauge Width, W_g (in)	Orientation, θ (°)	Pre-treatment Temperature, *T (°F)*	Heating Duration, *t* (s)	Cooling Environment	Fracture Location	Type	Process Zone
0.72	0 (warp)	N/A	N/A	N/A	At Shoulder	Side, 2 Places	Narrow

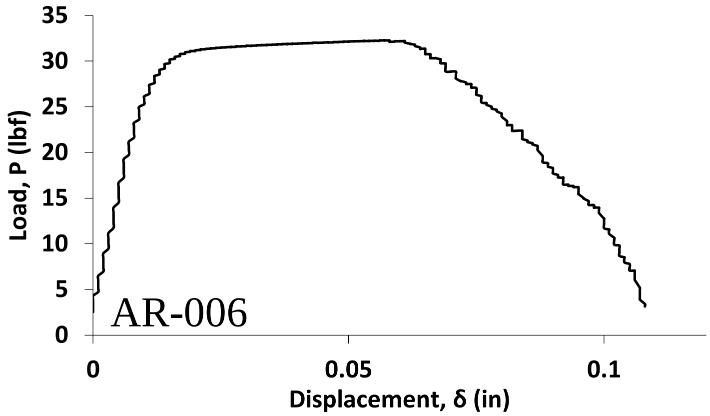

AR-006 Tensile Test Results

Stiffness (*lbf/in*)	2443
Yield Load (*lbf*)	26.9
Ultimate Load (*lbf*)	32.9

Specimen Details (AR-006)

Gauge Width, W_g (in)	Orientation, θ (°)	Pre-treatment Temperature, *T (°F)*	Heating Duration, *t* (s)	Cooling Environment	Fracture Location	Type	Process Zone
0.73	0 (warp)	N/A	N/A	N/A	Inside Gage	Side, 2 Places	Wide

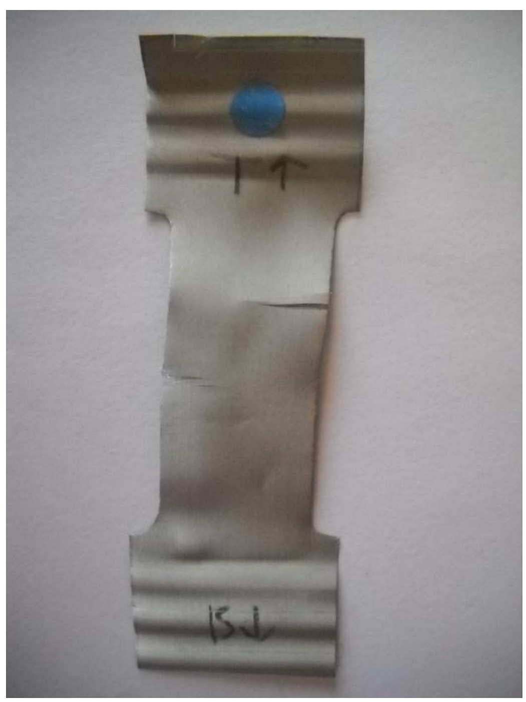

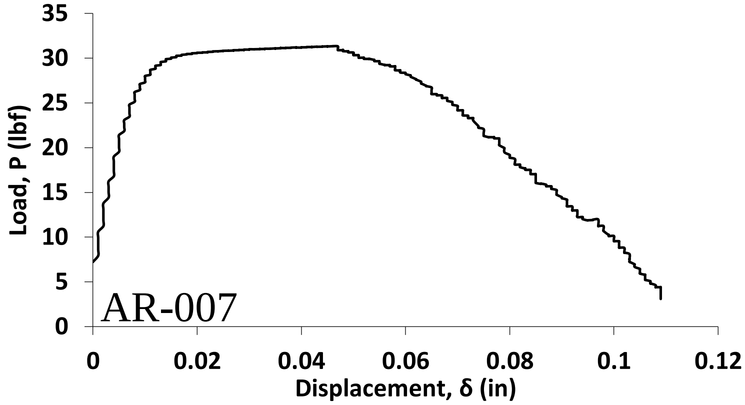

AR-007 Tensile Test Results

Stiffness (*lbf/in*)	2885
Yield Load (*lbf*)	27.3
Ultimate Load (*lbf*)	32.3

Specimen Details (AR-007)

Gauge Width, W_g (in)	Orientation, θ (°)	Pre-treatment Temperature, *T (°F)*	Heating Duration, *t* (s)	Cooling Environment	Fracture Location	Type	Process Zone
0.72	0 (warp)	N/A	N/A	N/A	Inside Gage	Side and center, 1 Place	Wide

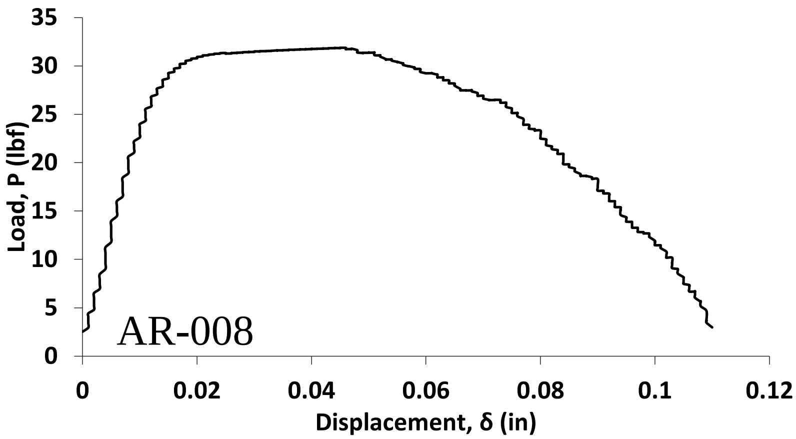

AR-008 Tensile Test Results

Stiffness (*lbf/in*)	2303
Yield Load (*lbf*)	28.5
Ultimate Load (*lbf*)	32.3

Specimen Details (AR-008)

Gauge Width, W_g (in)	Orientation, θ (°)	Pre-treatment Temperature, *T (°F)*	Heating Duration, *t* (s)	Cooling Environment	Fracture Location	Type	Process Zone
0.73	0 (warp)	N/A	N/A	N/A	Inside Gage	Side, 2 Places	Wide

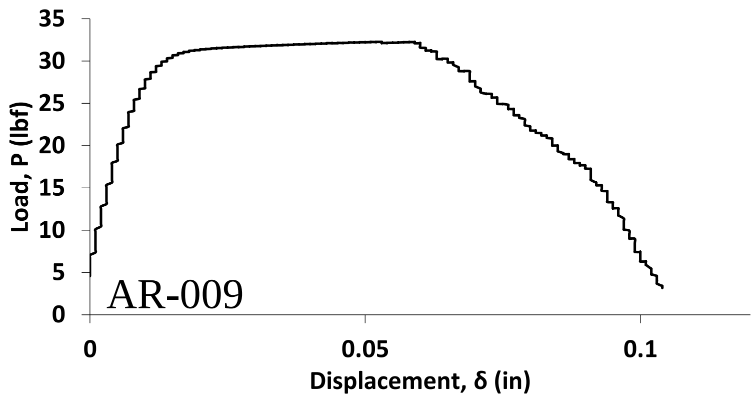

AR-009 Tensile Test Results

Stiffness (*lbf/in*)	2722
Yield Load (*lbf*)	27.6
Ultimate Load (*lbf*)	32.0

Specimen Details (AR-009)

Gauge Width, W_g (in)	Orientation, θ (°)	Pre-treatment Temperature, *T (°F)*	Heating Duration, *t* (s)	Cooling Environment	Fracture Location	Type	Process Zone
0.72	0 (warp)	N/A	N/A	N/A	Inside Gage	Side, 2 Places	Wide

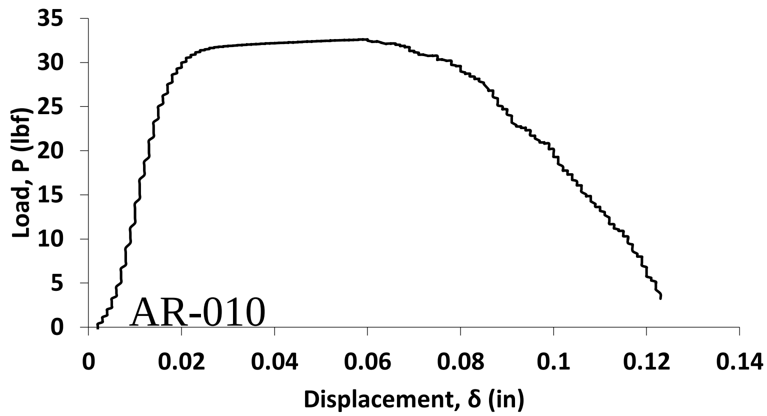

AR-010 Tensile Test Results

Stiffness (*lbf/in*)	2338
Yield Load (*lbf*)	28.7
Ultimate Load (*lbf*)	33.0

Specimen Details (AR-010)

Gauge Width, W_g (in)	Orientation, θ (°)	Pre-treatment Temperature, *T (°F)*	Heating Duration, *t* (s)	Cooling Environment	Fracture Location	Type	Process Zone
0.73	0 (warp)	N/A	N/A	N/A	Inside Gage	Side, 2 Places	Wide

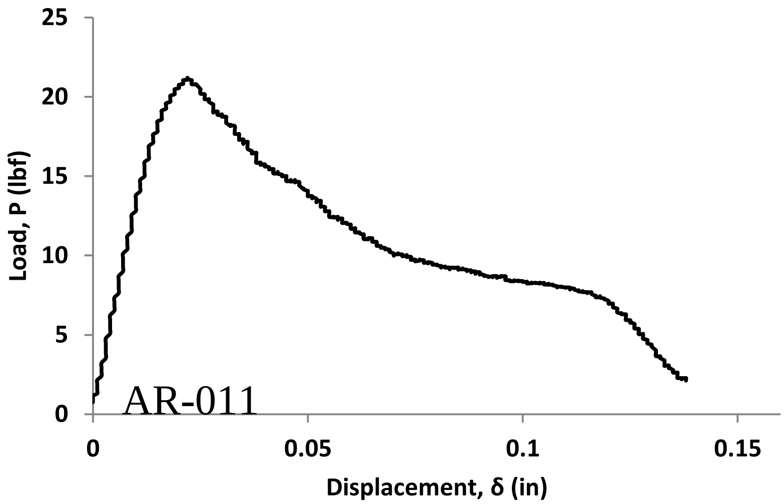

AR-011 Tensile Test Results	
Stiffness (*lbf/in*)	1303
Yield Load (*lbf*)	18.6
Ultimate Load (*lbf*)	21.4

Specimen Details (AR-011)

Gauge Width, $\boldsymbol{W_g}$ (in)	Orientation, θ (°)	Pre-treatment Temperature, *T (°F)*	Heating Duration, *t* (s)	Cooling Environment	Fracture Location	Type	Process Zone
0.73	15	N/A	N/A	N/A	At Shoulder	Side and Center, 2 Places	Narrow

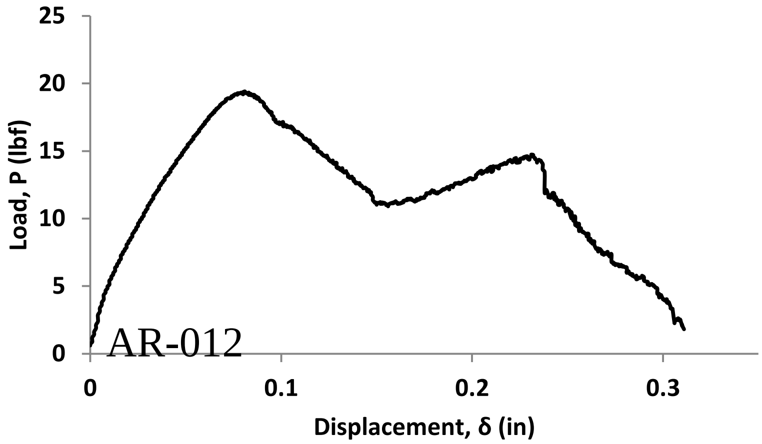

AR-012 Tensile Test Results

Stiffness (*lbf/in*)	280
Yield Load (*lbf*)	17.0
Ultimate Load (*lbf*)	19.2

Specimen Details (AR-012)

Gauge Width, W_g (in)	Orientation, θ (°)	Pre-treatment Temperature, *T (°F)*	Heating Duration, *t* (s)	Cooling Environment	Fracture Location	Type	Process Zone
0.75	30	N/A	N/A	N/A	Into Grips	Side, 1 Place	Narrow

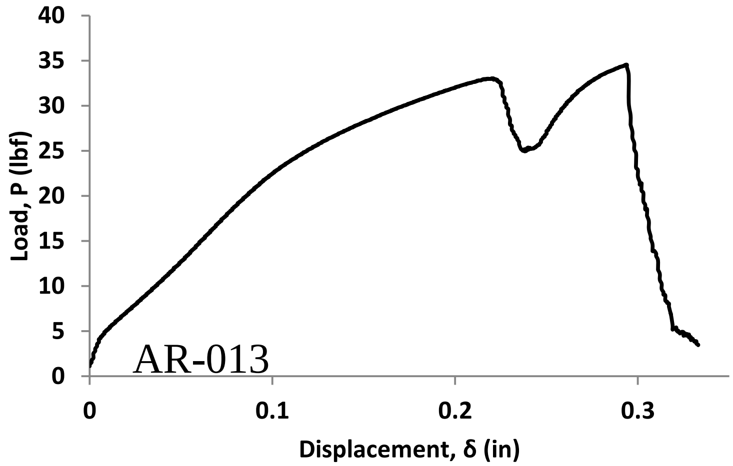

AR-013 Tensile Test Results

Stiffness (*lbf/in*)	558.5
Yield Load (*lbf*)	4.51
Ultimate Load (*lbf*)	34.2

Specimen Details (AR-013)

Gauge Width, W_g (in)	Orientation, θ (°)	Pre-treatment Temperature, *T (°F)*	Heating Duration, *t* (s)	Cooling Environment	Fracture Location	Type	Process Zone
0.75	45	N/A	N/A	N/A	Inside Gage/ Into Grips	Side, 2 Places	Narrow

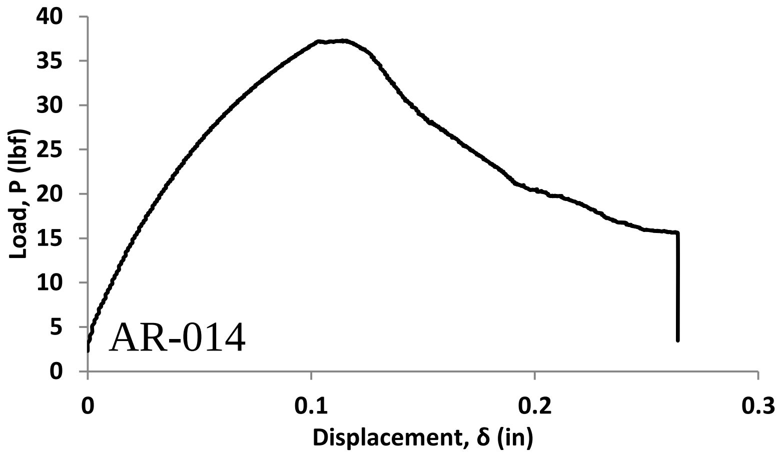

AR-014 Tensile Test Results

Stiffness (*lbf/in*)	465.4
Yield Load (*lbf*)	27.1
Ultimate Load (*lbf*)	37.1

Specimen Details (AR-014)

Gauge Width, W_g (in)	Orientation, θ (°)	Pre-treatment Temperature, *T (°F)*	Heating Duration, *t* (s)	Cooling Environment	Fracture Location	Type	Process Zone
0.75	60	N/A	N/A	N/A	Into Grips	Side, 2 Places	Narrow

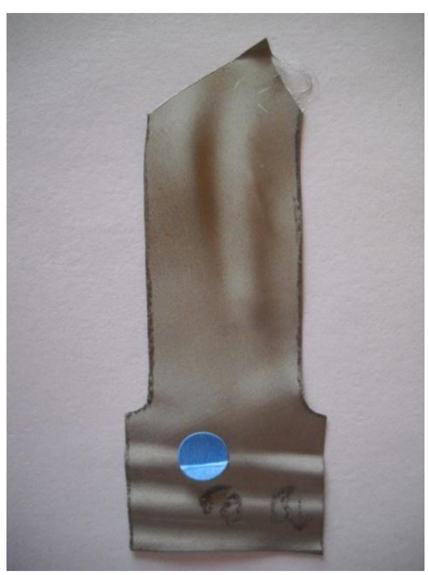

Note Failure Orientation Transition

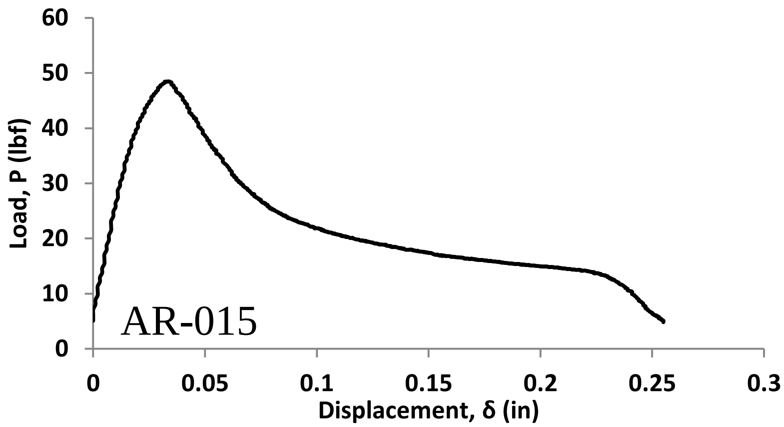

AR-015 Tensile Test Results

Stiffness (*lbf/in*)	1908
Yield Load (*lbf*)	39.2
Ultimate Load (*lbf*)	48.6

Specimen Details (AR-015)

Gauge Width, W_g (in)	Orientation, θ (°)	Pre-treatment Temperature, *T (°F)*	Heating Duration, *t* (s)	Cooling Environment	Fracture Location	Type	Process Zone
0.74	75	N/A	N/A	N/A	At Shoulder	Side, 2 Places	Narrow

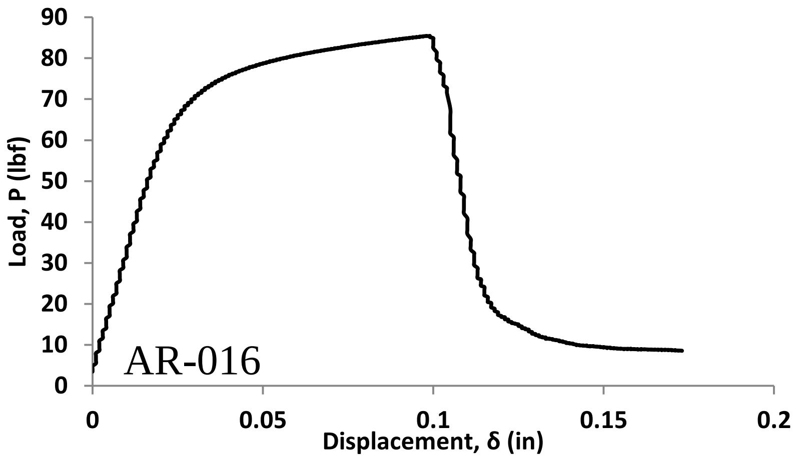

AR-016 Tensile Test Results

Stiffness (*lbf/in*)	2885
Yield Load (*lbf*)	56.9
Ultimate Load (*lbf*)	86.7

Specimen Details (AR-016)

Gauge Width, W_g (in)	Orientation, θ (°)	Pre-treatment Temperature, *T (°F)*	Heating Duration, *t* (s)	Cooling Environment	Fracture Location	Type	Process Zone
0.73	90 (weft)	N/A	N/A	N/A	At Shoulder	Side, 2 Places	Narrow

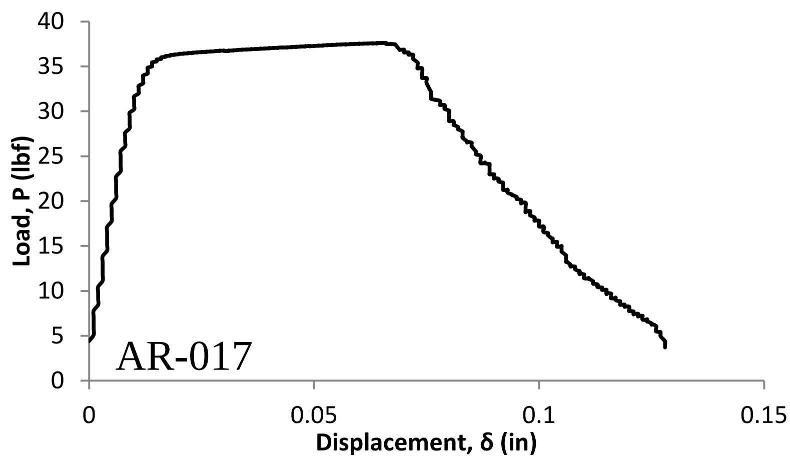

AR-017 Tensile Test Results

Stiffness (*lbf/in*)	2691
Yield Load (*lbf*)	32.5
Ultimate Load (*lbf*)	37.6

Specimen Details (AR-017)

Gauge Width, W_g (in)	Orientation, θ (°)	Pre-treatment Temperature, *T (°F)*	Heating Duration, *t* (s)	Cooling Environment	Fracture Location	Type	Process Zone
0.74	0 (warp)	600	100	Room Air	Inside Gage	Side, 2 Places	Wide/ Narrow

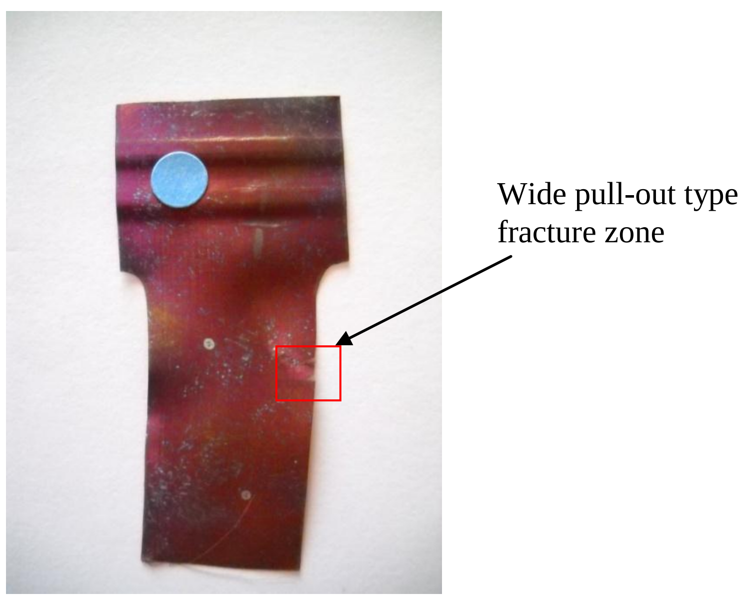

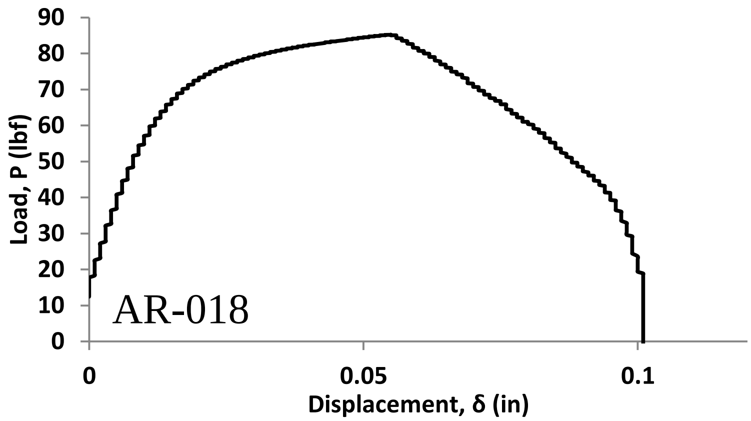

AR-018 Tensile Test Results	
Stiffness (*lbf/in*)	3903
Yield Load (*lbf*)	60.0
Ultimate Load (*lbf*)	84.7

Specimen Details (AR-018)

Gauge Width, $\boldsymbol{W_g}$ (in)	Orientation, θ (°)	Pre-treatment Temperature, *T (°F)*	Heating Duration, *t* (s)	Cooling Environment	Fracture Location	Type	Process Zone
0.74	90 (weft)	600	100	Room Air	Inside Gage	Side, 1 Place	Narrow - Jagged

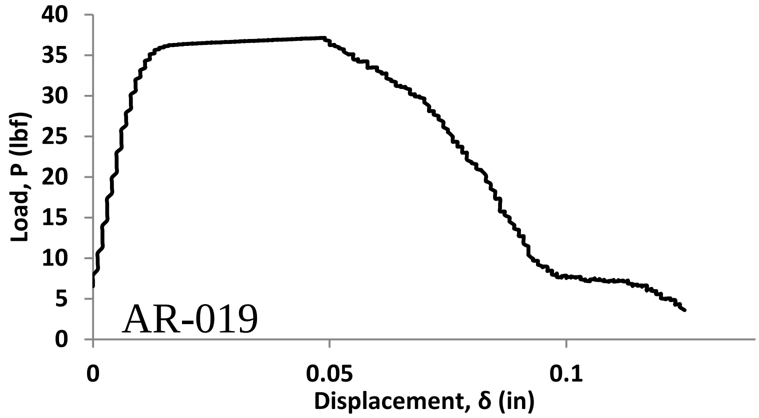

AR-19 Tensile Test Results

Stiffness (*lbf/in*)	2665
Yield Load (*lbf*)	33.1
Ultimate Load (*lbf*)	37.3

Specimen Details (AR-019)

Gauge Width, W_g (in)	Orientation, θ (°)	Pre-treatment Temperature, *T (°F)*	Heating Duration, *t* (s)	Cooling Environment	Fracture Location	Type	Process Zone
0.74	0 (warp)	600	200	Room Air	Inside Gage / At Shoulder	Side, 2 Places	Wide

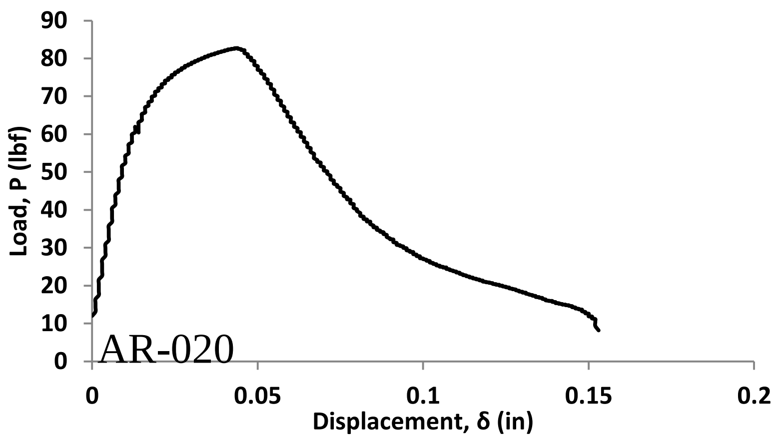

AR-020 Tensile Test Results

Stiffness (*lbf/in*)	3950
Yield Load (*lbf*)	61.5
Ultimate Load (*lbf*)	82.8

Specimen Details (AR-020)

Gauge Width, W_g (in)	Orientation, θ (°)	Pre-treatment Temperature, *T (°F)*	Heating Duration, *t* (s)	Cooling Environment	Fracture Location	Type	Process Zone
0.74	90 (weft)	600	200	Room Air	Inside Gage / At Shoulder	Side, 2 Places	Narrow

Appendix B: AI Tensile Test Results

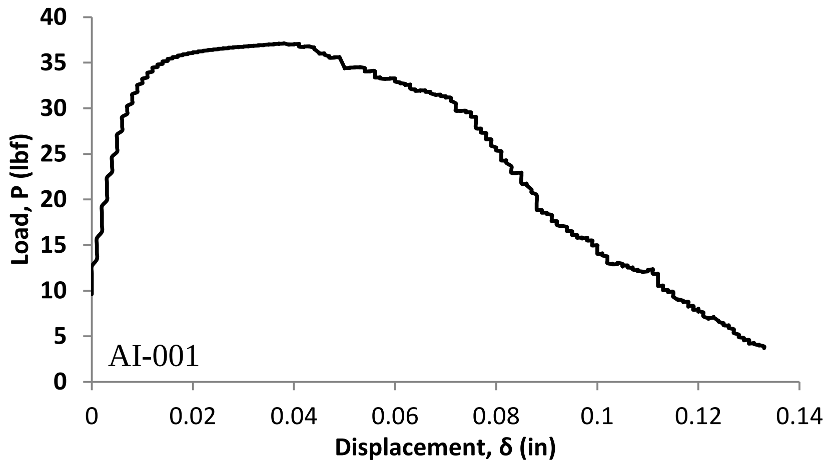

AI-001 Tensile Test Results

Stiffness (*lbf/in*)	2365
Yield Load (*lbf*)	32.3
Ultimate Load (*lbf*)	37.0

Specimen Details (AI-001)

Gauge Width, W_g (in)	Orientation, θ (°)	Pre-treatment Temperature, *T (°F)*	Heating Duration, *t* (s)	Cooling Environment	Fracture Location	Type	Process Zone
0.73	0 (warp)	N/A	N/A	N/A	Inside Gage	Side, 2 Places	wide

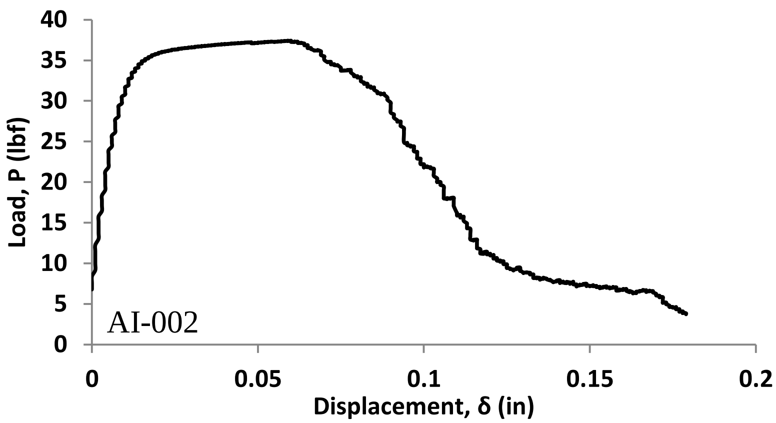

AI-002 Tensile Test Results

Stiffness (*lbf/in*)	2220
Yield Load (*lbf*)	31.8
Ultimate Load (*lbf*)	37.3

Specimen Details (AI-002)

Gauge Width, $\boldsymbol{W_g}$ (in)	Orientation, θ (°)	Pre-treatment Temperature, *T (°F)*	Heating Duration, *t* (s)	Cooling Environment	Fracture Location	Type	Process Zone
0.73	0 (warp)	N/A	N/A	N/A	Inside Gage/ Into Grips	Side and Center, 2 Places	wide

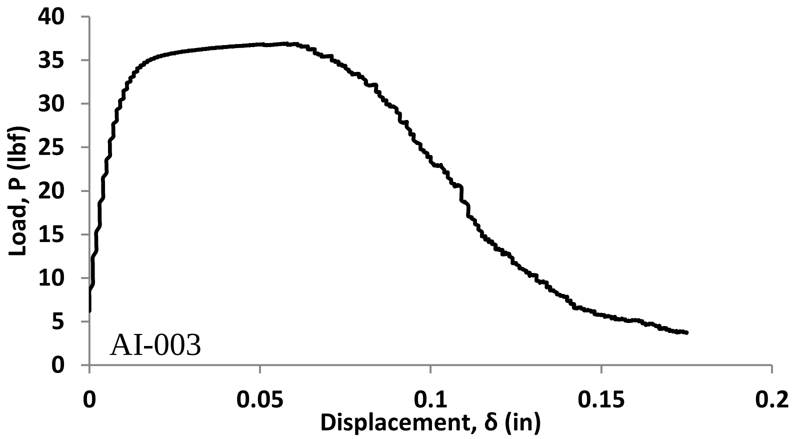

AI-003 Tensile Test Results

Stiffness (*lbf/in*)	2370
Yield Load (*lbf*)	31.6
Ultimate Load (*lbf*)	37.1

Specimen Details (AI-003)

Gauge Width, W_g (in)	Orientation, θ (°)	Pre-treatment Temperature, *T (°F)*	Heating Duration, *t* (s)	Cooling Environment	Fracture Location	Type	Process Zone
0.71	0 (warp)	N/A	N/A	N/A	Inside Gage / At Shoulder	Side and center, 3 Places	wide

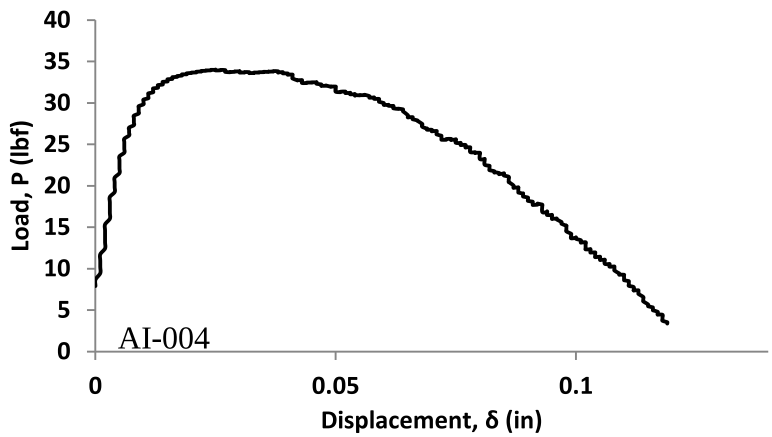

AI-004 Tensile Test Results

Stiffness (*lbf/in*)	2218
Yield Load (*lbf*)	30.0
Ultimate Load (*lbf*)	33.5

Specimen Details (AI-004)

Gauge Width, W_g (in)	Orientation, θ (°)	Pre-treatment Temperature, *T (°F)*	Heating Duration, *t* (s)	Cooling Environment	Fracture Location	Type	Process Zone
0.70	0 (warp)	N/A	N/A	N/A	Inside Gage / At Shoulder	Side, 2 Places	wide

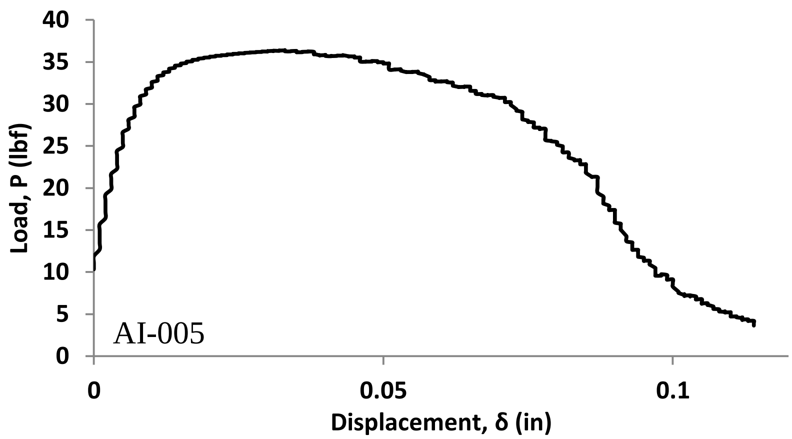

AI-005 Tensile Test Results

Stiffness (*lbf/in*)	2308
Yield Load (*lbf*)	31.3
Ultimate Load (*lbf*)	36.4

Specimen Details (AI-005)

Gauge Width, W_g (in)	Orientation, θ (°)	Pre-treatment Temperature, *T (°F)*	Heating Duration, *t* (s)	Cooling Environment	Fracture Location	Type	Process Zone
0.71	0 (warp)	N/A	N/A	N/A	Inside Gage	Side, 2 Places	wide

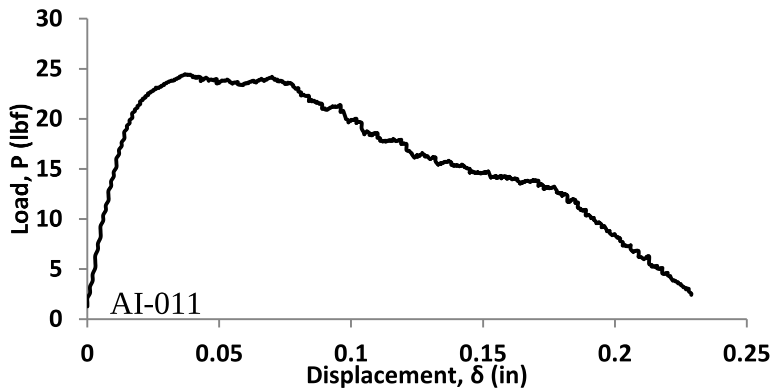

AI-011 Tensile Test Results

Stiffness (*lbf/in*)	1173
Yield Load (*lbf*)	19.3
Ultimate Load (*lbf*)	24.1

Specimen Details (AI-011)

Gauge Width, W_g (in)	Orientation, θ (°)	Pre-treatment Temperature, *T (°F)*	Heating Duration, *t* (s)	Cooling Environment	Fracture Location	Type	Process Zone
0.73	15	N/A	N/A	N/A	Into Grips	side, 2 Places	wide

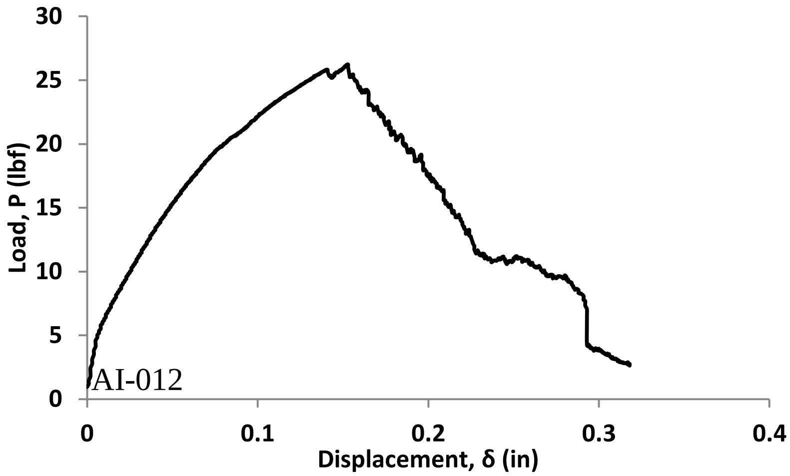

AI-012 Tensile Test Results

Stiffness (*lbf/in*)	215.2
Yield Load (*lbf*)	19.6
Ultimate Load (*lbf*)	26.0

Specimen Details (AI-012)

Gauge Width, W_g (in)	Orientation, θ (°)	Pre-treatment Temperature, *T (°F)*	Heating Duration, *t* (s)	Cooling Environment	Fracture Location	Type	Process Zone
0.72	30	N/A	N/A	N/A	Into Grips	Side, 1 Place	narrow

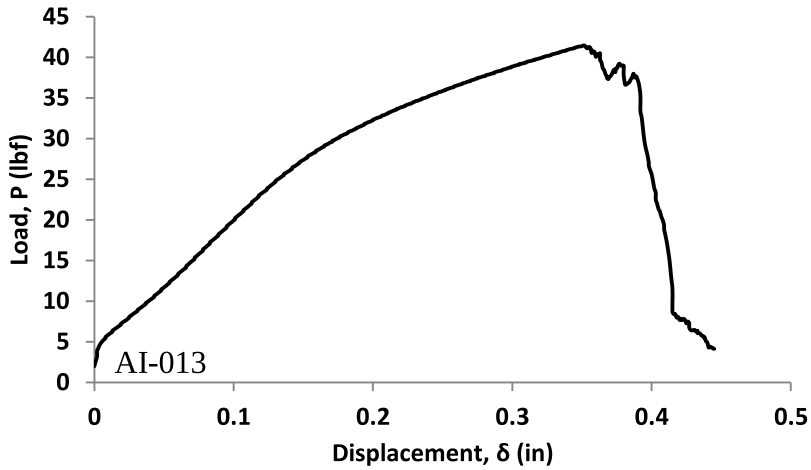

AI-013 Tensile Test Results

Stiffness (*lbf/in*)	607.6
Yield Load (*lbf*)	4.9
Ultimate Load (*lbf*)	42.0

Specimen Details (AI-013)

Gauge Width, W_g (in)	Orientation, θ (°)	Pre-treatment Temperature, *T (°F)*	Heating Duration, *t* (s)	Cooling Environment	Fracture Location	Type	Process Zone
0.74	45	N/A	N/A	N/A	Into Grips / At shoulder	Side, 2 Places	narrow

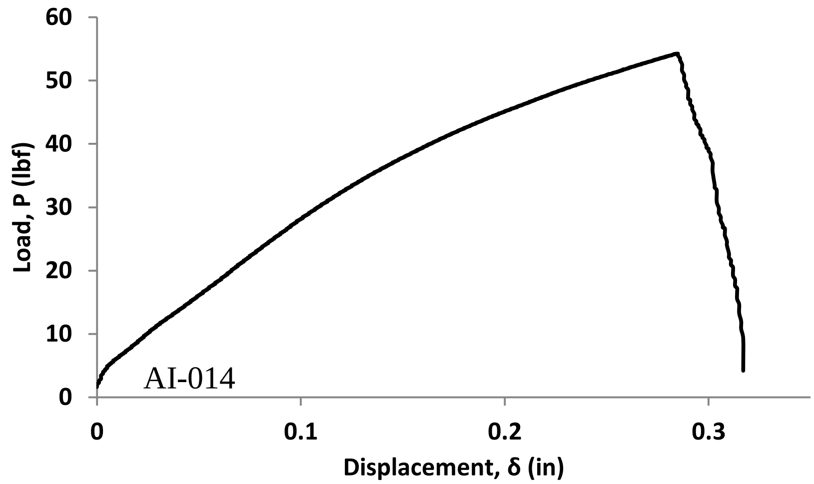

AI-014 Tensile Test Results

Stiffness (*lbf/in*)	245.5
Yield Load (*lbf*)	29.8
Ultimate Load (*lbf*)	53.0

Specimen Details (AI-014)

Gauge Width, W_g (in)	Orientation, θ (°)	Pre-treatment Temperature, *T (°F)*	Heating Duration, *t* (s)	Cooling Environment	Fracture Location	Type	Process Zone
0.73	60	N/A	N/A	N/A	Inside Gage	Side, 1 place	narrow

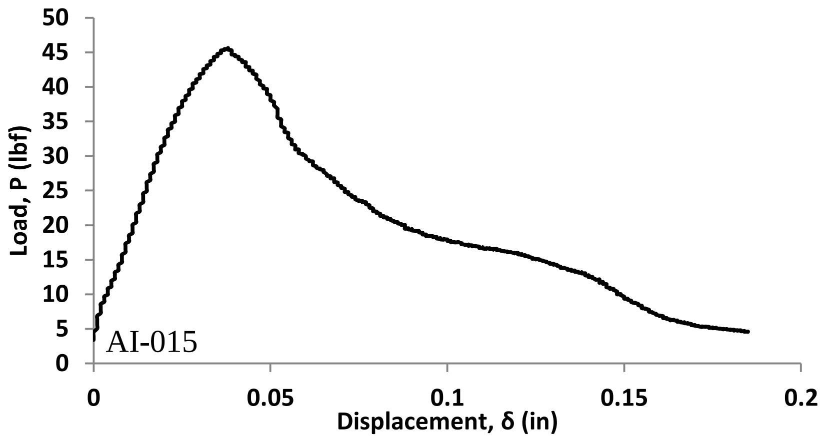

AI-015 Tensile Test Results

Stiffness (*lbf/in*)	1367.5
Yield Load (*lbf*)	34.8
Ultimate Load (*lbf*)	45.0

Specimen Details (AI-015)

Gauge Width, W_g (in)	Orientation, θ (°)	Pre-treatment Temperature, *T (°F)*	Heating Duration, *t* (s)	Cooling Environment	Fracture Location	Type	Process Zone
0.73	75	N/A	N/A	N/A	At Shoulder / Into Grips	Side, 2 places	narrow

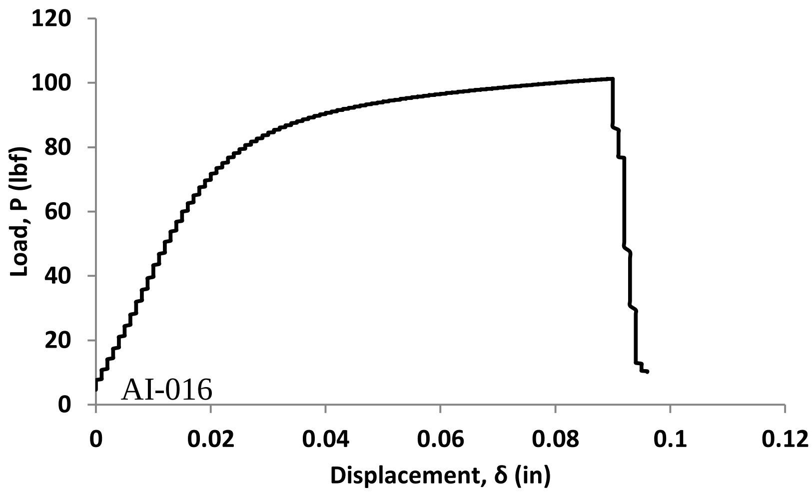

AI-016 Tensile Test Results

Stiffness (*lbf/in*)	3490
Yield Load (*lbf*)	65.2
Ultimate Load (*lbf*)	100.3

Specimen Details (AI-016)

Gauge Width, W_g (in)	Orientation, θ (°)	Pre-treatment Temperature, *T (°F)*	Heating Duration, *t* (s)	Cooling Environment	Fracture Location	Type	Process Zone
0.75	90 (weft)	N/A	N/A	N/A	Inside Gage	Side, 2 places	narrow

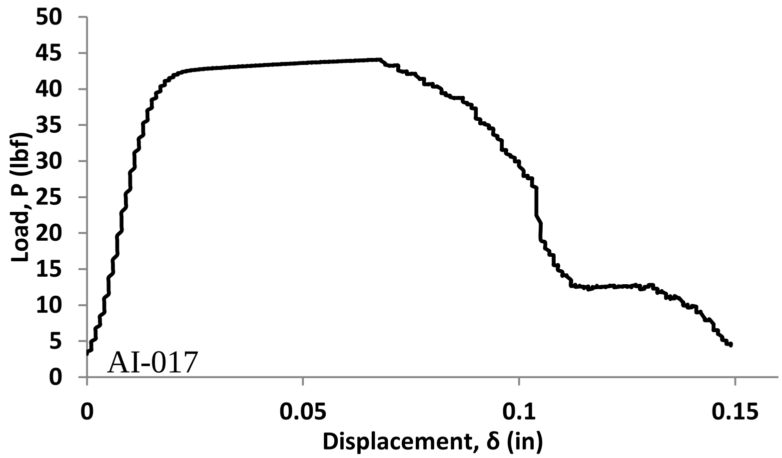

AI-017 Tensile Test Results	
Stiffness (*lbf/in*)	2530
Yield Load (*lbf*)	38.3
Ultimate Load (*lbf*)	43.7

Specimen Details (AI-017)

Gauge Width, W_g (in)	Orientation, θ (°)	Pre-treatment Temperature, *T (°F)*	Heating Duration, *t* (s)	Cooling Environment	Fracture Location	Type	Process Zone
0.75	0 (warp)	600	100	Room Air	Inside Gage	Side, 2 places	wide

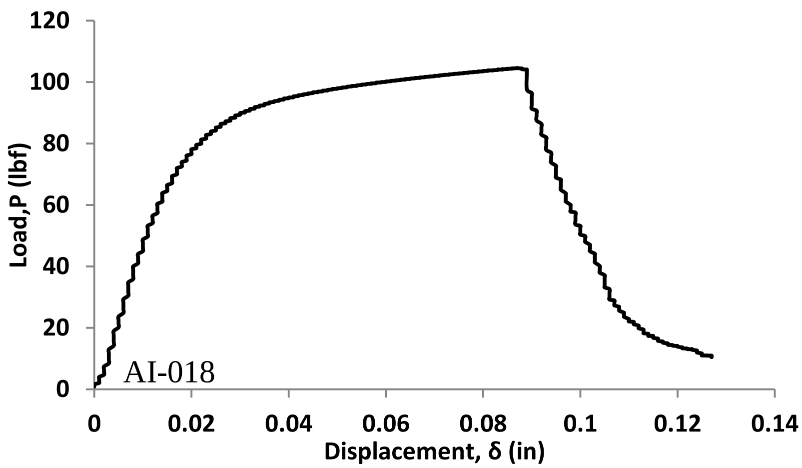

AI-018 Tensile Test Results

Stiffness (*lbf/in*)	4679
Yield Load (*lbf*)	64.0
Ultimate Load (*lbf*)	103.7

Specimen Details (AI-018)

Gauge Width, W_g (in)	Orientation, θ (°)	Pre-treatment Temperature, *T (°F)*	Heating Duration, *t* (s)	Cooling Environment	Fracture Location	Type	Process Zone
0.72	90 (weft)	600	100	Room Air	Inside Gage / At Shoulder	Side, 2 places	narrow

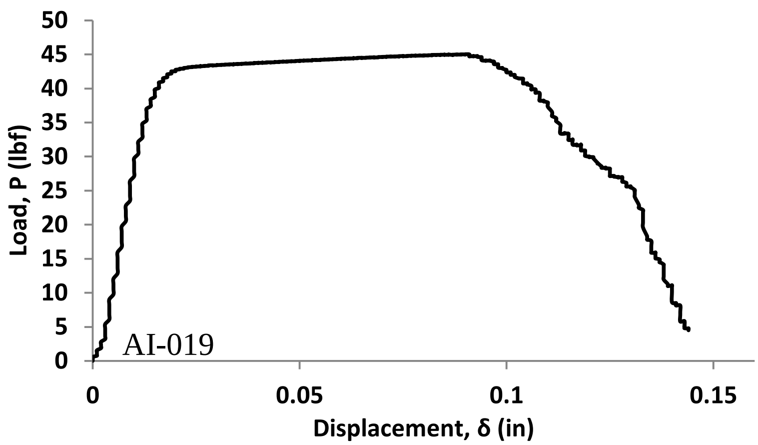

AI-019 Tensile Test Results

Stiffness (*lbf/in*)	3022
Yield Load (*lbf*)	36.6
Ultimate Load (*lbf*)	44.6

Specimen Details (AI-019)

Gauge Width, W_g (in)	Orientation, θ (°)	Pre-treatment Temperature, *T (°F)*	Heating Duration, *t* (s)	Cooling Environment	Fracture Location	Type	Process Zone
0.75	0 (warp)	600	200	Room Air	Inside Gage	Side and center, 3 places	wide

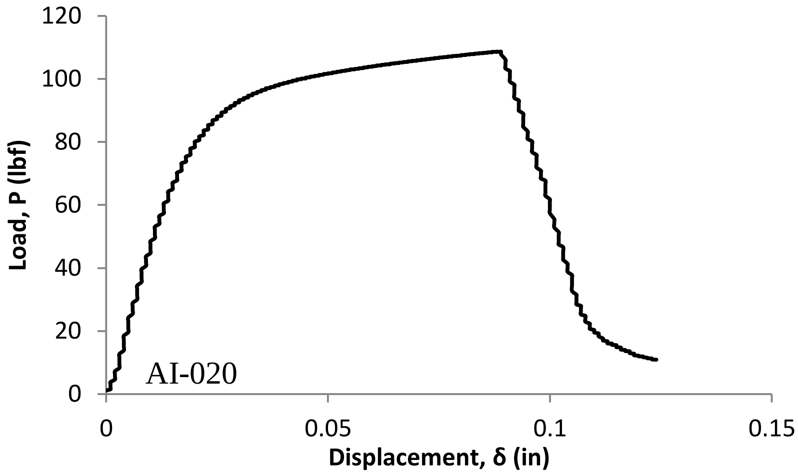

AI-020 Tensile Test Results

Stiffness (*lbf/in*)	4754
Yield Load (*lbf*)	75.0
Ultimate Load (*lbf*)	108.5

Specimen Details (AI-020)

Gauge Width, W_g (in)	Orientation, θ (°)	Pre-treatment Temperature, *T (°F)*	Heating Duration, *t* (s)	Cooling Environment	Fracture Location	Type	Process Zone
0.75	90 (weft)	600	200	Room Air	Inside Gage / At Shoulder	side, 2 places	narrow

Appendix C: BL Tensile Test Results

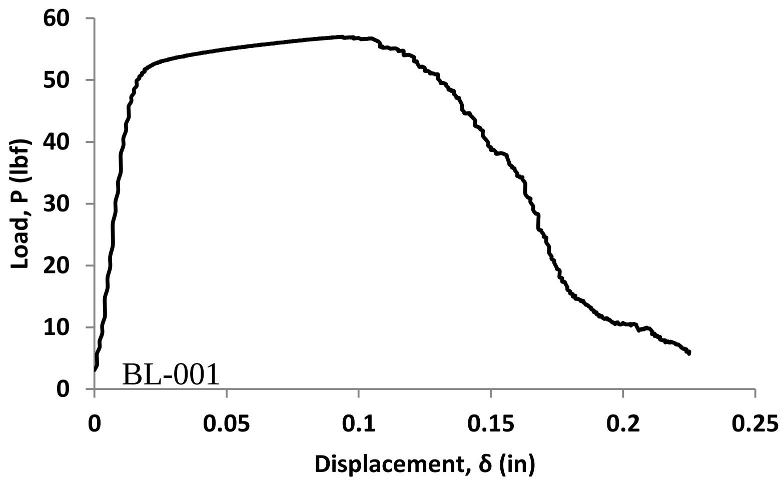

BL-001 Tensile Test Results

Stiffness (*lbf/in*)	3459
Yield Load (*lbf*)	46.1
Ultimate Load (*lbf*)	57.2

Specimen Details (BL-001)

Gauge Width, W_g (in)	Orientation, θ (°)	Pre-treatment Temperature, *T (°F)*	Heating Duration, *t* (s)	Cooling Environment	Fracture Location	Type	Process Zone
0.78	0 (warp)	N/A	N/A	N/A	Inside Gage	side, 2 places	wide

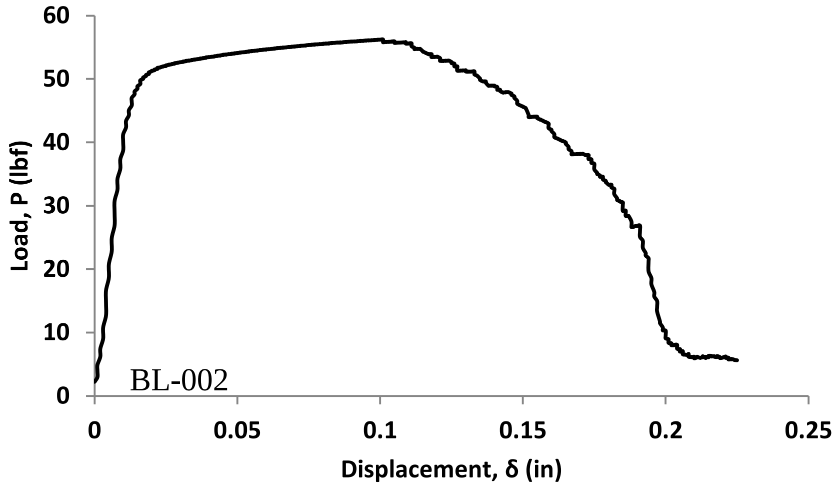

BL-002 Tensile Test Results

Stiffness (*lbf/in*)	3861.7
Yield Load (*lbf*)	45.1
Ultimate Load (*lbf*)	55.3

Specimen Details (BL-002)

Gauge Width, W_g (in)	Orientation, θ (°)	Pre-treatment Temperature, *T (°F)*	Heating Duration, *t* (s)	Cooling Environment	Fracture Location	Type	Process Zone
0.76	0 (warp)	N/A	N/A	N/A	Inside Gage	side, 2 places	wide

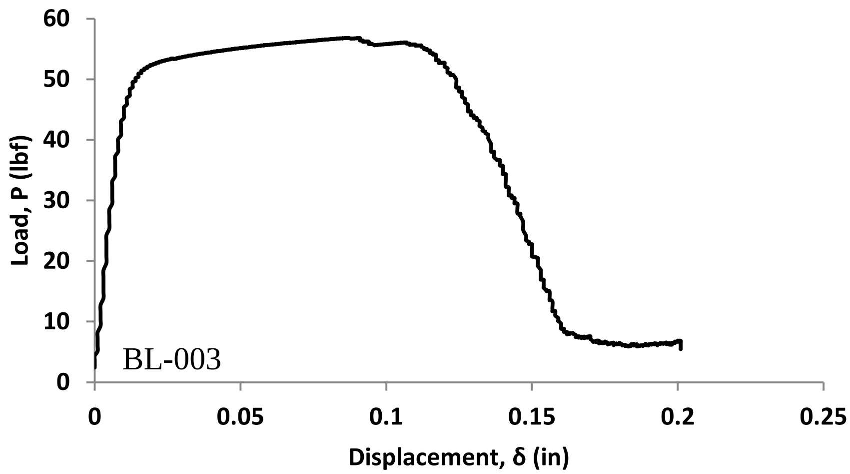

BL-003 Tensile Test Results

Stiffness (*lbf/in*)	4285
Yield Load (*lbf*)	45.6
Ultimate Load (*lbf*)	55.9

Specimen Details (BL-003)

Gauge Width, W_g (in)	Orientation, θ (°)	Pre-treatment Temperature, *T (°F)*	Heating Duration, *t* (s)	Cooling Environment	Fracture Location	Type	Process Zone
0.78	0 (warp)	N/A	N/A	N/A	Inside Gage / At Shoulder	Side and center, 3 places	wide

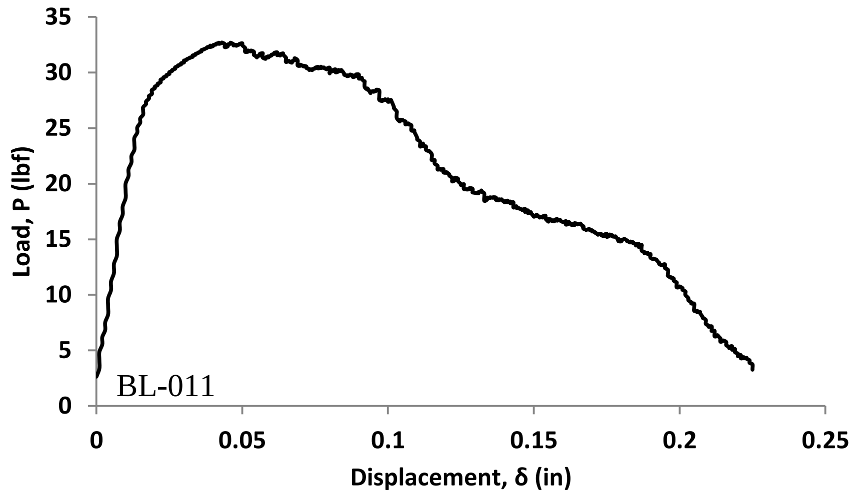

BL-011 Tensile Test Results

Stiffness (*lbf/in*)	1582
Yield Load (*lbf*)	25.8
Ultimate Load (*lbf*)	32.3

Specimen Details (BL-011)

Gauge Width, $\boldsymbol{W_g}$ (in)	Orientation, θ (°)	Pre-treatment Temperature, *T (°F)*	Heating Duration, *t* (s)	Cooling Environment	Fracture Location	Type	Process Zone
0.73	15	N/A	N/A	N/A	At Shoulder	side, 2 places	wide

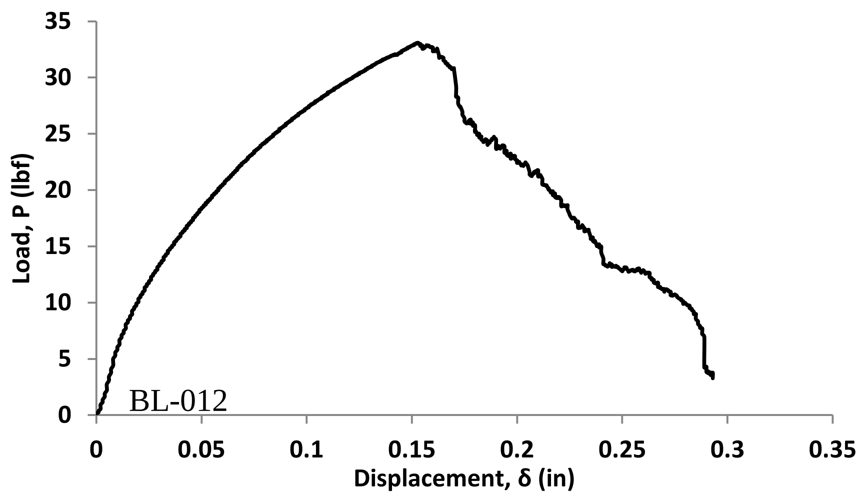

BL-012 Tensile Test Results

Stiffness (*lbf/in*)	283.5
Yield Load (*lbf*)	20.5
Ultimate Load (*lbf*)	33.0

Specimen Details (BL-012)

Gauge Width, W_g (in)	Orientation, θ (°)	Pre-treatment Temperature, *T (°F)*	Heating Duration, *t* (s)	Cooling Environment	Fracture Location	Type	Process Zone
0.73	30	N/A	N/A	N/A	Into Grips	side, 1 place	narrow

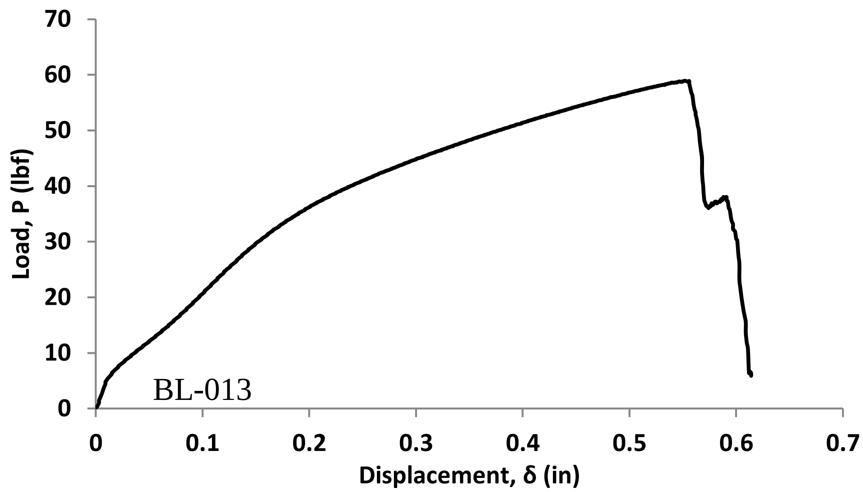

BL-013 Tensile Test Results

Stiffness (*lbf/in*)	517
Yield Load (*lbf*)	4.8
Ultimate Load (*lbf*)	59.0

Specimen Details (BL-013)

Gauge Width, W_g (in)	Orientation, θ (°)	Pre-treatment Temperature, *T (°F)*	Heating Duration, *t* (s)	Cooling Environment	Fracture Location	Type	Process Zone
0.73	45	N/A	N/A	N/A	At Shoulder / Into Grips	side, 2 places	narrow

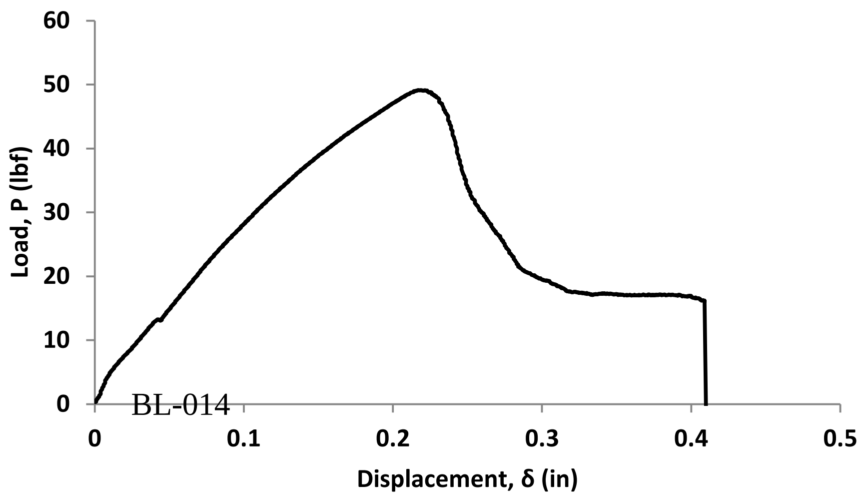

BL-014 Tensile Test Results

Stiffness (*lbf/in*)	268.6
Yield Load (*lbf*)	26.0
Ultimate Load (*lbf*)	49.5

Specimen Details (BL-014)

Gauge Width, W_g (in)	Orientation, θ (°)	Pre-treatment Temperature, *T (°F)*	Heating Duration, *t* (s)	Cooling Environment	Fracture Location	Type	Process Zone
0.71	60	N/A	N/A	N/A	At Shoulder / Into Grips	side, 2 places	narrow

Note Fracture Orientation Transition

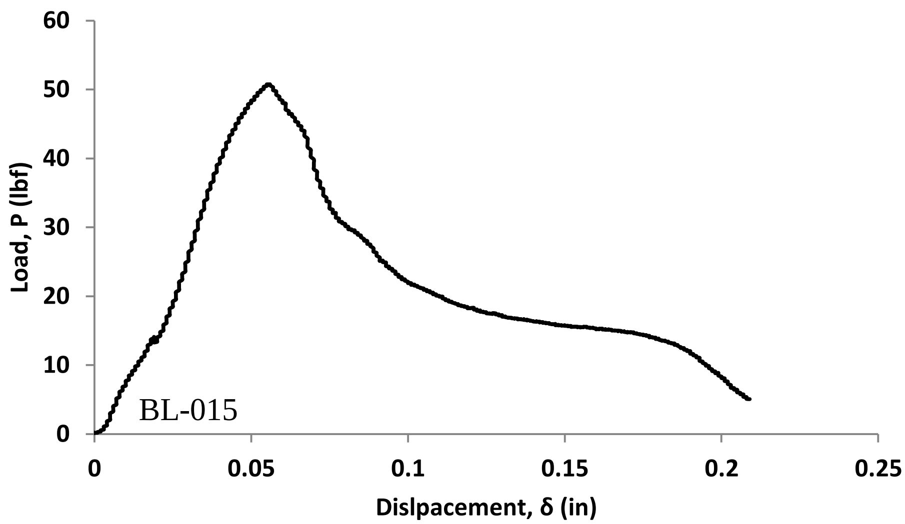

BL-015 Tensile Test Results

Stiffness (*lbf/in*)	978.0
Yield Load (*lbf*)	39.2
Ultimate Load (*lbf*)	51.0

Specimen Details (BL-015)

Gauge Width, W_g (in)	Orientation, θ (°)	Pre-treatment Temperature, *T (°F)*	Heating Duration, *t* (s)	Cooling Environment	Fracture Location	Type	Process Zone
0.75	75	N/A	N/A	N/A	At Shoulder	side, 2 places	narrow

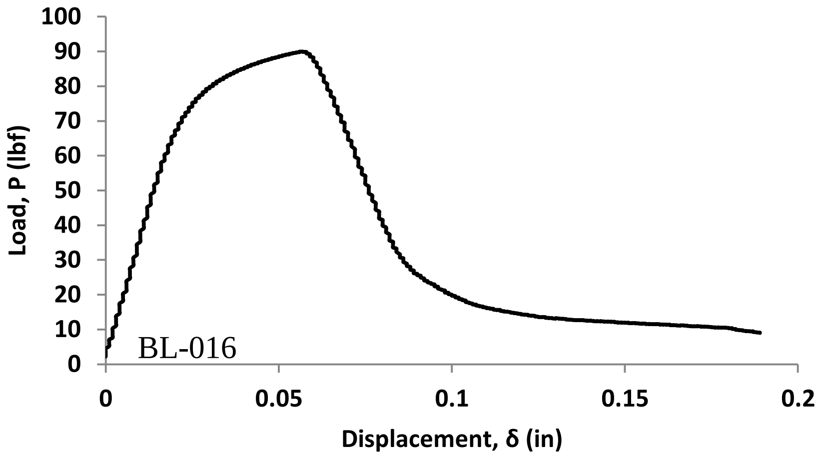

BL-016 Tensile Test Results

Stiffness (*lbf/in*)	3345
Yield Load (*lbf*)	71.0
Ultimate Load (*lbf*)	90.0

Specimen Details (BL-016)

Gauge Width, W_g (in)	Orientation, θ (°)	Pre-treatment Temperature, *T (°F)*	Heating Duration, *t* (s)	Cooling Environment	Fracture Location	Type	Process Zone
0.77	90 (weft)	N/A	N/A	N/A	At Shoulder / Inside Gage	side, 2 places	narrow

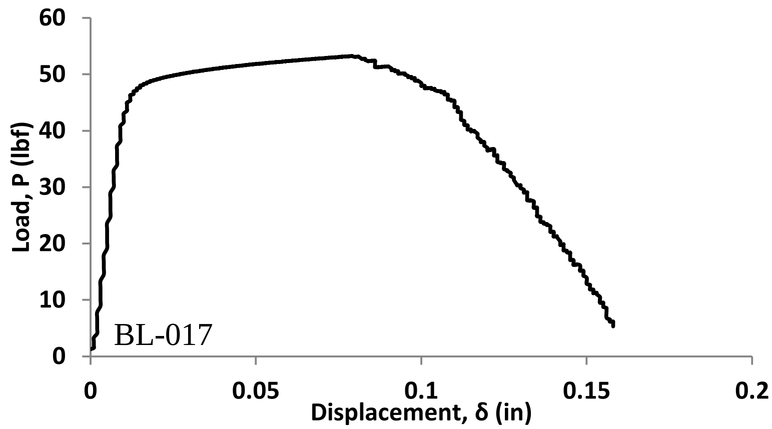

BL-017 Tensile Test Results

Stiffness (*lbf/in*)	4476
Yield Load (*lbf*)	44.2
Ultimate Load (*lbf*)	53.0

Specimen Details (BL-017)

Gauge Width, W_g (in)	Orientation, θ (°)	Pre-treatment Temperature, *T (°F)*	Heating Duration, *t* (s)	Cooling Environment	Fracture Location	Type	Process Zone
0.72	0 (warp)	600	100	Room Air	Inside Gage / At Shoulder	side, 2 places	wide

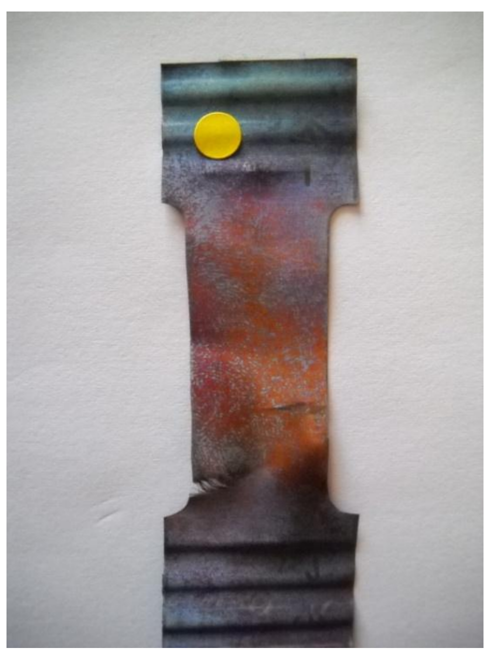

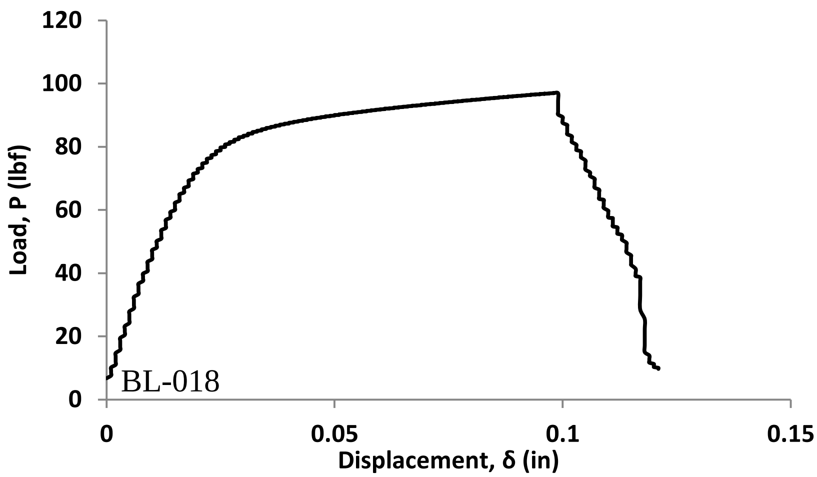

BL-018 Tensile Test Results

Stiffness (*lbf/in*)	3704
Yield Load (*lbf*)	64.3
Ultimate Load (*lbf*)	96.6

Specimen Details (BL-018)

Gauge Width, W_g (in)	Orientation, θ (°)	Pre-treatment Temperature, *T (°F)*	Heating Duration, *t* (s)	Cooling Environment	Fracture Location	Type	Process Zone
0.71	90 (weft)	600	100	Room Air	Inside Gage	side, 2 places	Narrow - Jagged

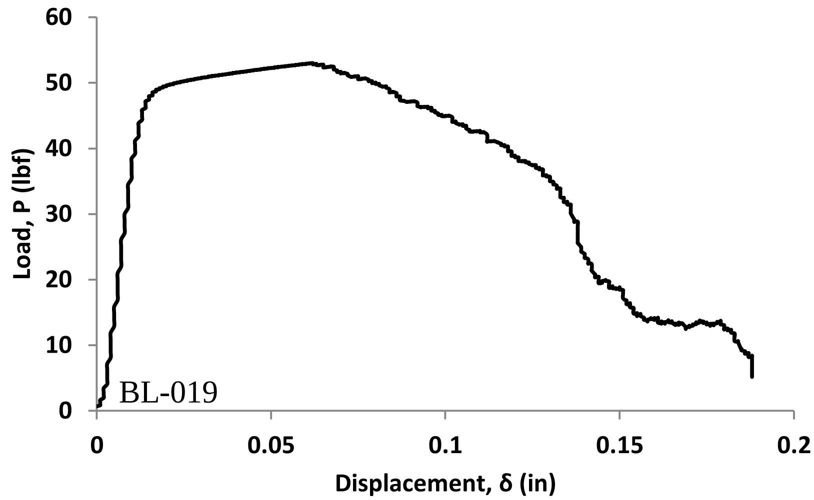

BL-019 Tensile Test Results

Stiffness (*lbf/in*)	4056
Yield Load (*lbf*)	43.0
Ultimate Load (*lbf*)	52.3

Specimen Details (BL-019)

Gauge Width, W_g (in)	Orientation, θ (°)	Pre-treatment Temperature, *T (°F)*	Heating Duration, *t* (s)	Cooling Environment	Fracture Location	Type	Process Zone
0.73	0 (warp)	600	200	Room Air	Inside Gage	side, 2 places	wide

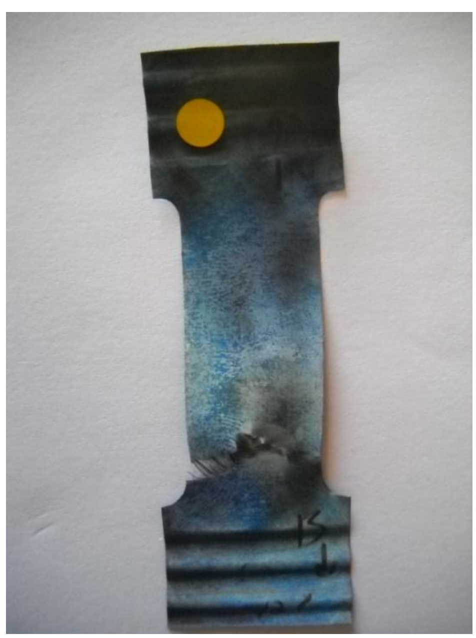

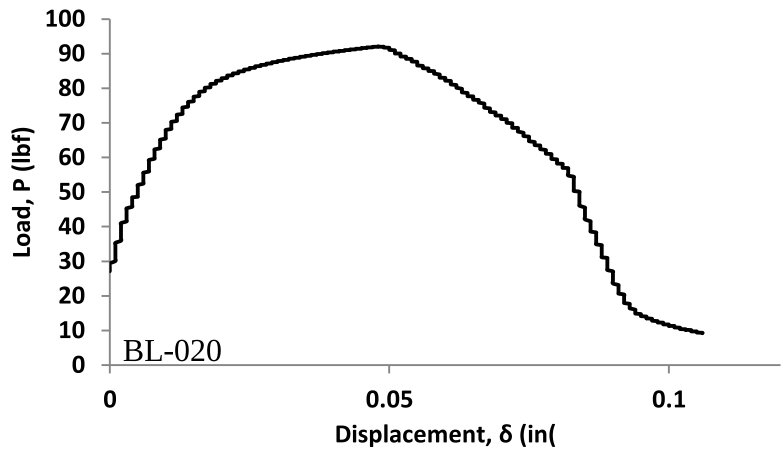

BL-020 Tensile Test Results

Stiffness (*lbf/in*)	3589
Yield Load (*lbf*)	70.6
Ultimate Load (*lbf*)	92.0

Specimen Details (BL-020)

Gauge Width, W_g (in)	Orientation, θ (°)	Pre-treatment Temperature, *T (°F)*	Heating Duration, *t* (s)	Cooling Environment	Fracture Location	Type	Process Zone
0.73	90 (weft)	600	200	Room Air	Inside Gage / At Shoulder	side, 2 places	narrow

Appendix D: B3 Tensile Test Results

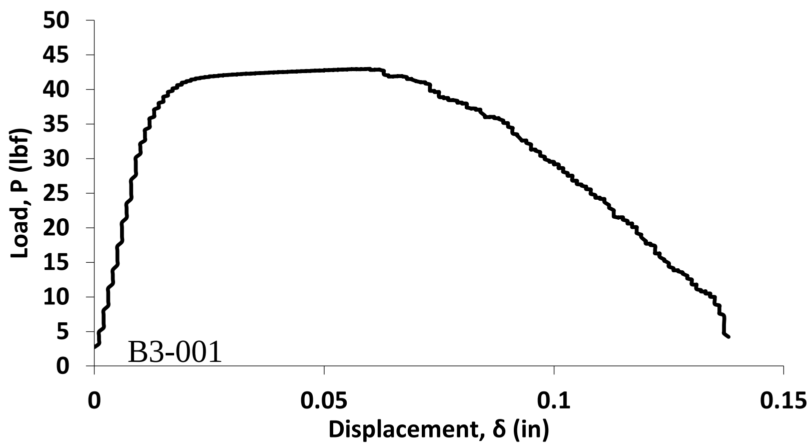

B3-001 Tensile Test Results	
Stiffness (*lbf/in*)	2612
Yield Load (*lbf*)	38.8
Ultimate Load (*lbf*)	43.1

Specimen Details (B3-001)

Gauge Width, W_g (in)	Orientation, θ (°)	Pre-treatment Temperature, *T (°F)*	Heating Duration, *t* (s)	Cooling Environment	Fracture Location	Type	Process Zone
0.76	0 (warp)	N/A	N/A	N/A	Inside Gage	side, 2 places	wide

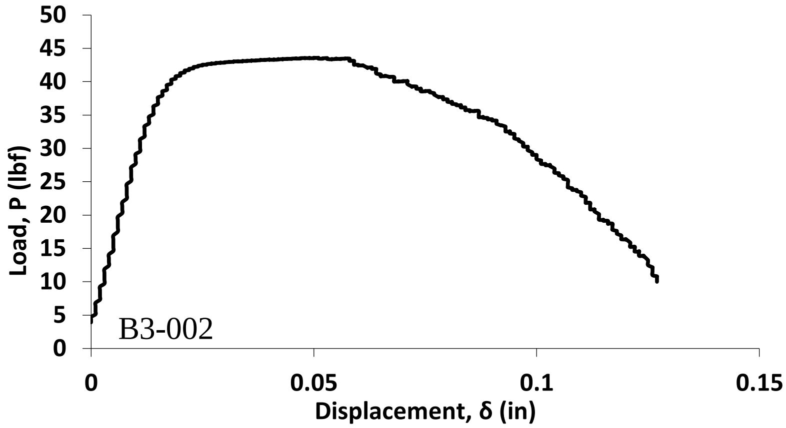

B3-002 Tensile Test Results

Stiffness (*lbf/in*)	2254
Yield Load (*lbf*)	38.6
Ultimate Load (*lbf*)	43.7

Specimen Details (B3-002)

Gauge Width, W_g (in)	Orientation, θ (°)	Pre-treatment Temperature, *T (°F)*	Heating Duration, *t* (s)	Cooling Environment	Fracture Location	Type	Process Zone
0.77	0 (warp)	N/A	N/A	N/A	Inside Gage	Side and Center, 3 places	wide

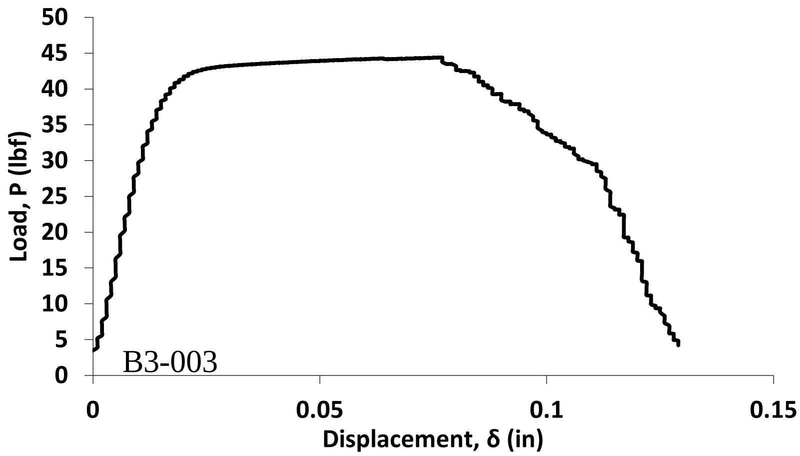

B3-003 Tensile Test Results

Stiffness (*lbf/in*)	2431
Yield Load (*lbf*)	38.5
Ultimate Load (*lbf*)	44.0

Specimen Details (B3-003)

Gauge Width, W_g (in)	Orientation, θ (°)	Pre-treatment Temperature, *T (°F)*	Heating Duration, *t* (s)	Cooling Environment	Fracture Location	Type	Process Zone
0.75	0 (warp)	N/A	N/A	N/A	Inside Gage	Side and Center, 2 places	wide

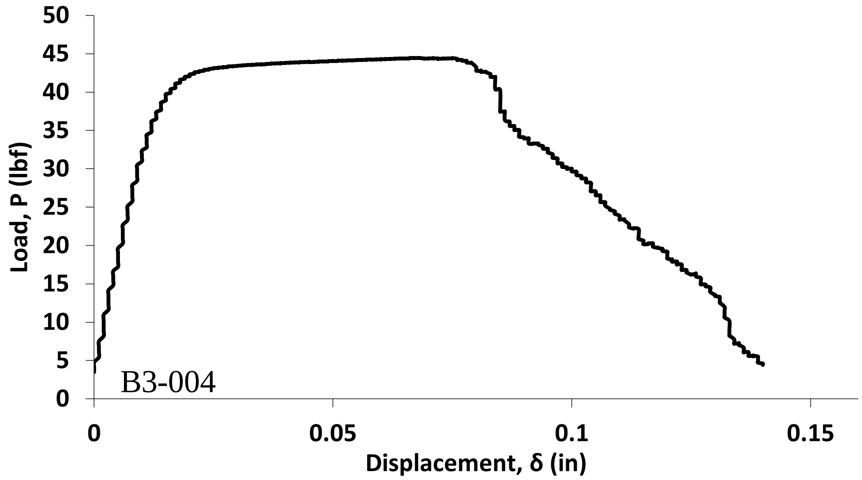

B3-004 Tensile Test Results

Stiffness (*lbf/in*)	2218
Yield Load (*lbf*)	35.5
Ultimate Load (*lbf*)	40.5

Specimen Details (B3-004)

Gauge Width, W_g (in)	Orientation, θ (°)	Pre-treatment Temperature, *T (°F)*	Heating Duration, *t* (s)	Cooling Environment	Fracture Location	Type	Process Zone
0.76	0 (warp)	N/A	N/A	N/A	Inside Gage	Side, 2 places	wide

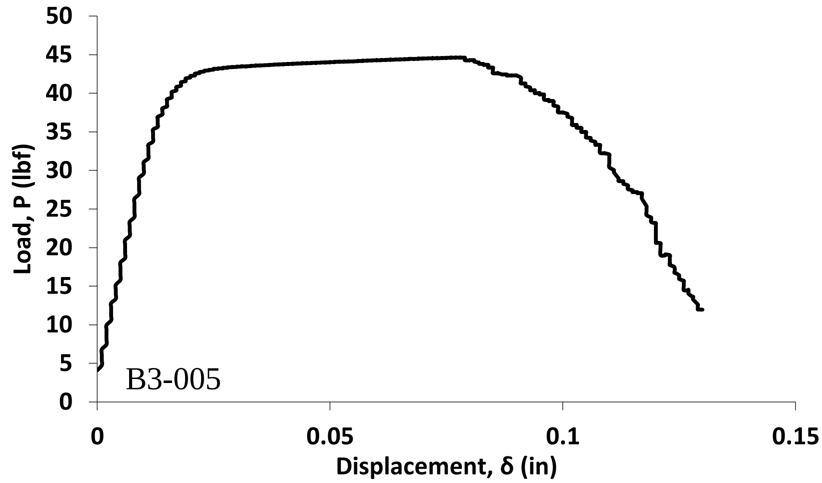

B3-005 Tensile Test Results

Stiffness (*lbf/in*)	2374
Yield Load (*lbf*)	39.8
Ultimate Load (*lbf*)	44.7

Specimen Details (B3-005)

Gauge Width, W_g (in)	Orientation, θ (°)	Pre-treatment Temperature, *T (°F)*	Heating Duration, *t* (s)	Cooling Environment	Fracture Location	Type	Process Zone
0.77	0 (warp)	N/A	N/A	N/A	Inside Gage / Into Grips	Side, 2 places	wide

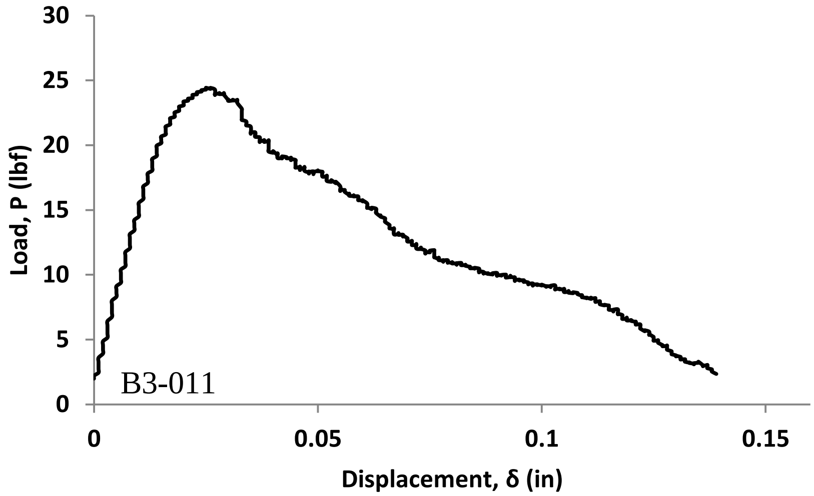

B3-011 Tensile Test Results

Stiffness (*lbf/in*)	1268
Yield Load (*lbf*)	20.4
Ultimate Load (*lbf*)	24.5

Specimen Details (B3-011)

Gauge Width, $\boldsymbol{W_g}$ (in)	Orientation, θ (°)	Pre-treatment Temperature, *T (°F)*	Heating Duration, *t* (s)	Cooling Environment	Fracture Location	Type	Process Zone
0.71	15	N/A	N/A	N/A	At Shoulder	Side, 2 places	narrow

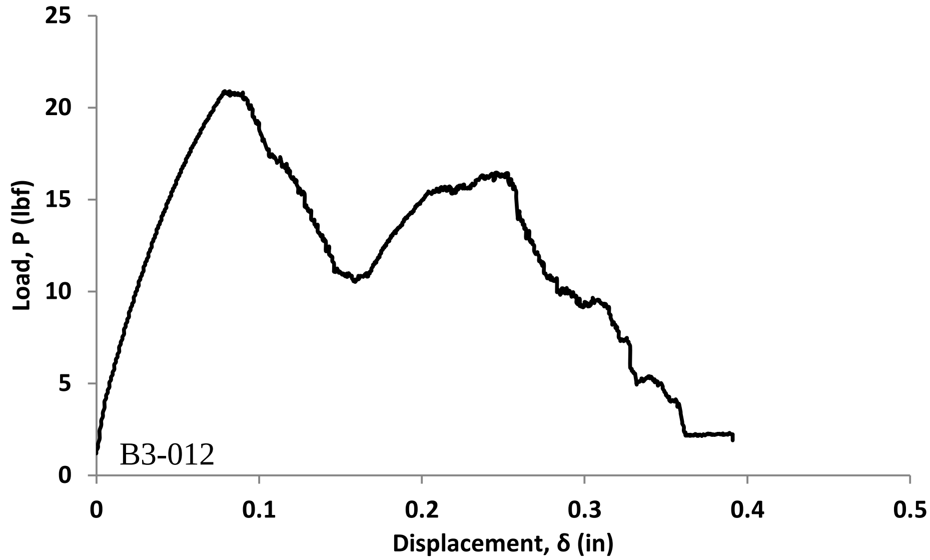

B3-012 Tensile Test Results

Stiffness (*lbf/in*)	290.3
Yield Load (*lbf*)	15.8
Ultimate Load (*lbf*)	21.0

Specimen Details (B3-012)

Gauge Width, W_g (in)	Orientation, θ (°)	Pre-treatment Temperature, *T (°F)*	Heating Duration, *t* (s)	Cooling Environment	Fracture Location	Type	Process Zone
0.71	30	N/A	N/A	N/A	Into Grips	Side, 1 place	narrow

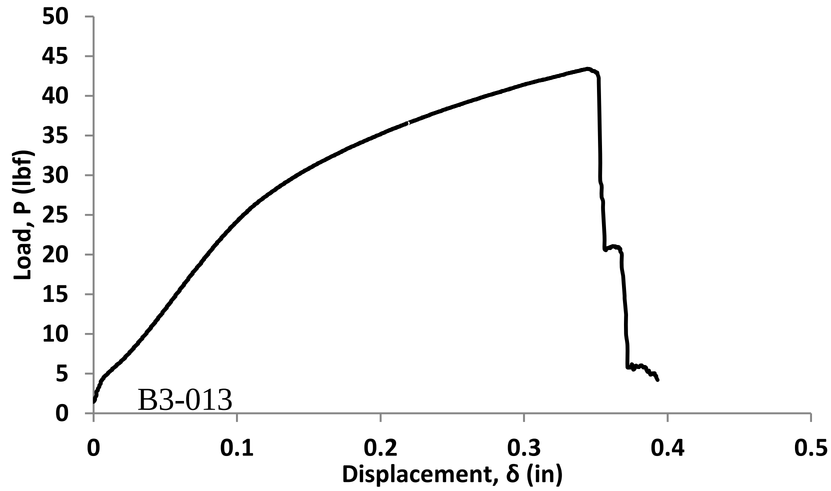

B3-013 Tensile Test Results

Stiffness (*lbf/in*)	278.2
Yield Load (*lbf*)	4.80
Ultimate Load (*lbf*)	43.4

Specimen Details (B3-013)

Gauge Width, W_g (in)	Orientation, θ (°)	Pre-treatment Temperature, *T (°F)*	Heating Duration, *t* (s)	Cooling Environment	Fracture Location	Type	Process Zone
0.73	45	N/A	N/A	N/A	At Shoulder	Side, 1 place	narrow

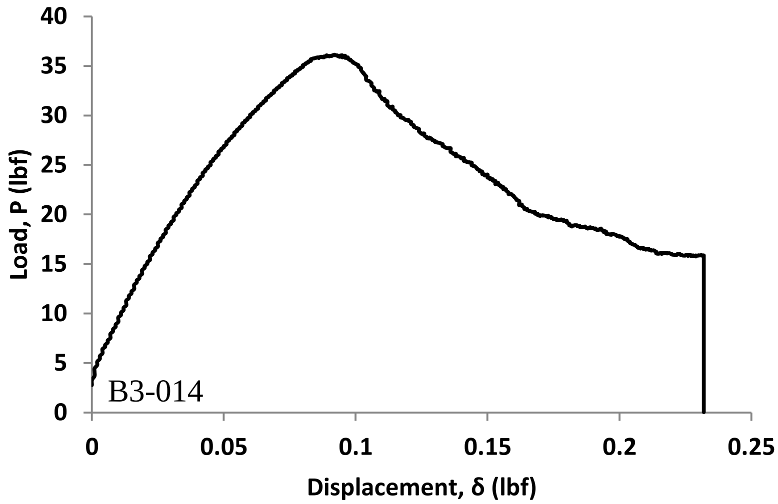

B3-014 Tensile Test Results

Stiffness (*lbf/in*)	500.1
Yield Load (*lbf*)	21.9
Ultimate Load (*lbf*)	36.1

Specimen Details (B3-014)

Gauge Width, W_g (in)	Orientation, θ (°)	Pre-treatment Temperature, *T (°F)*	Heating Duration, *t* (s)	Cooling Environment	Fracture Location	Type	Process Zone
0.70	60	N/A	N/A	N/A	Into Gage	Side, 1 place	narrow

Note Transition of Fracture Orientation

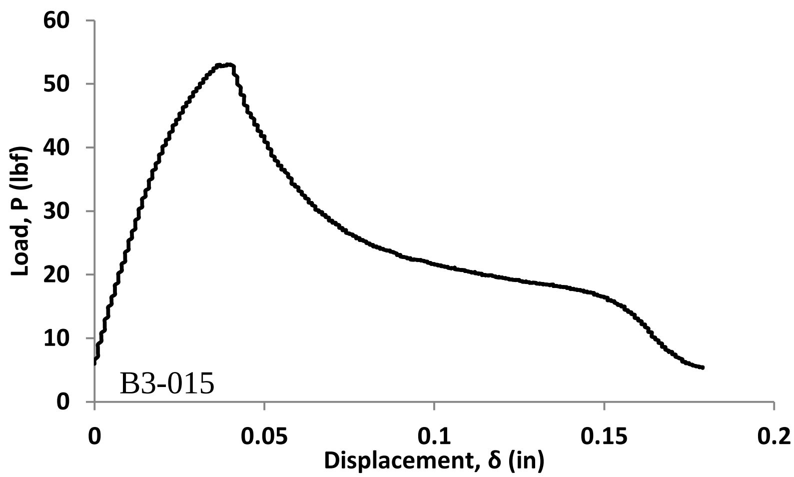

B3-015 Tensile Test Results

Stiffness (*lbf/in*)	1692
Yield Load (*lbf*)	38.3
Ultimate Load (*lbf*)	52.6

Specimen Details (B3-015)

Gauge Width, W_g (in)	Orientation, θ (°)	Pre-treatment Temperature, *T (°F)*	Heating Duration, *t* (s)	Cooling Environment	Fracture Location	Type	Process Zone
0.72	75	N/A	N/A	N/A	At Shoulder	Side, 2 place	narrow

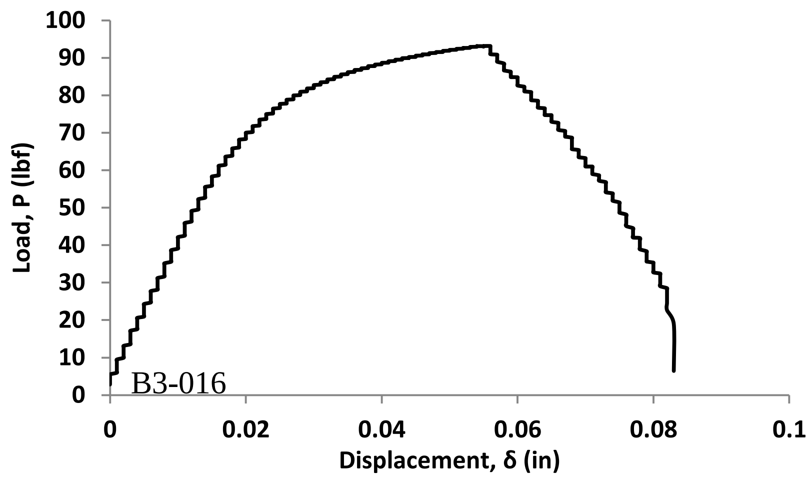

B3-016 Tensile Test Results

Stiffness (*lbf/in*)	3522
Yield Load (*lbf*)	61.1
Ultimate Load (*lbf*)	92.8

Specimen Details (B3-016)

Gauge Width, W_g (in)	Orientation, θ (°)	Pre-treatment Temperature, *T (°F)*	Heating Duration, *t* (s)	Cooling Environment	Fracture Location	Type	Process Zone
0.75	90 (weft)	N/A	N/A	N/A	At Shoulder	Side, 1 place	narrow

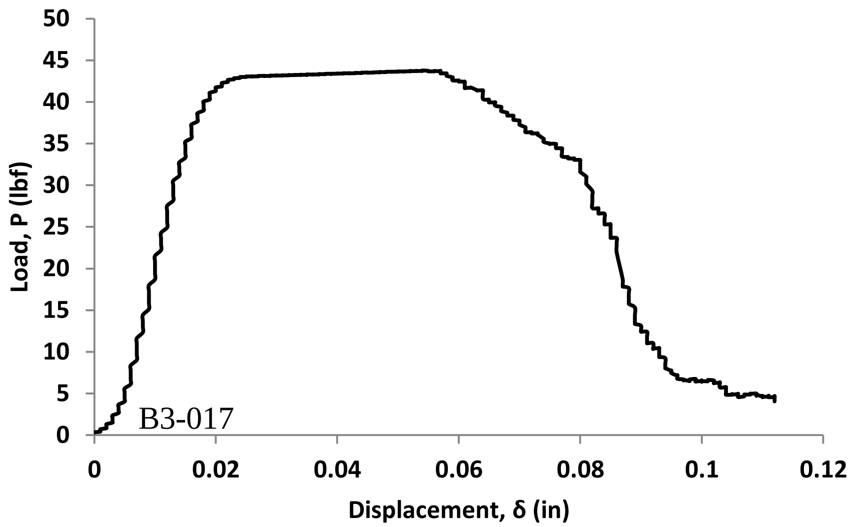

B3-017 Tensile Test Results	
Stiffness (*lbf/in*)	2590
Yield Load (*lbf*)	37.6
Ultimate Load (*lbf*)	43.7

Specimen Details (B3-017)

Gauge Width, W_g (in)	Orientation, θ (°)	Pre-treatment Temperature, *T (°F)*	Heating Duration, *t* (s)	Cooling Environment	Fracture Location	Type	Process Zone
0.74	0 (warp)	600	100	Room Air	Inside Gage / At Shoulder	Side, 2 place	wide

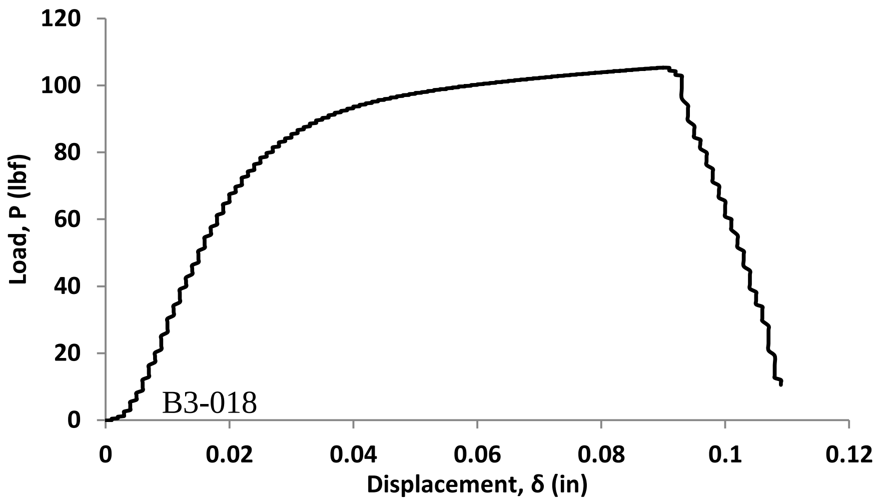

B3-018 Tensile Test Results

Stiffness (*lbf/in*)	3770
Yield Load (*lbf*)	65.0
Ultimate Load (*lbf*)	105.0

Specimen Details (B3-018)

Gauge Width, W_g (in)	Orientation, θ (°)	Pre-treatment Temperature, *T (°F)*	Heating Duration, *t* (s)	Cooling Environment	Fracture Location	Type	Process Zone
0.75	90 (weft)	600	100	Room Air	Inside Gage	Side, 2 place	Narrow - Jagged

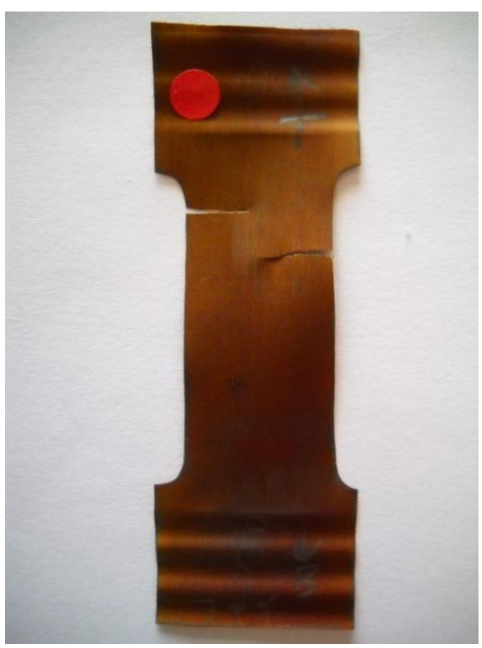

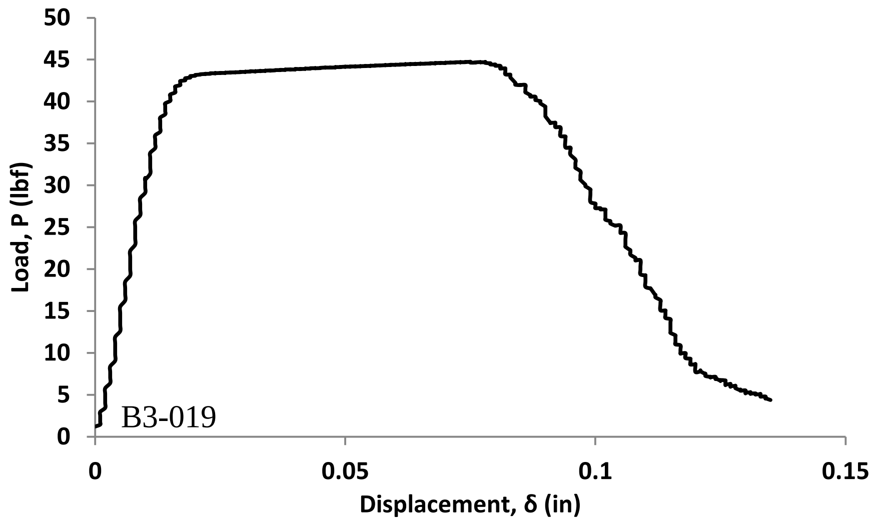

B3-019 Tensile Test Results

Stiffness (*lbf/in*)	2990
Yield Load (*lbf*)	39.3
Ultimate Load (*lbf*)	45.0

Specimen Details (B3-019)

Gauge Width, W_g (in)	Orientation, θ (°)	Pre-treatment Temperature, *T (°F)*	Heating Duration, *t* (s)	Cooling Environment	Fracture Location	Type	Process Zone
0.74	0 (warp)	600	200	Room Air	Inside Gage / At Shoulder	Side, 2 place	Narrow

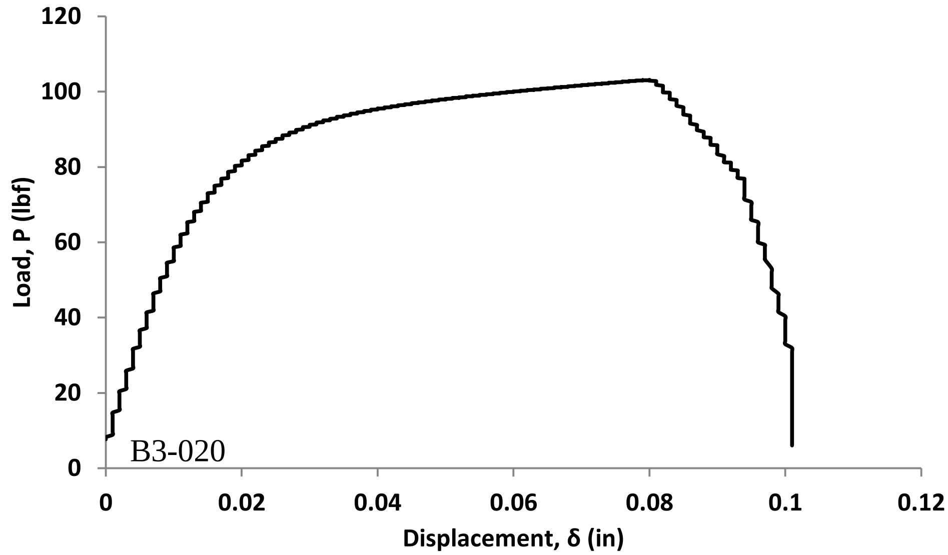

B3-020 Tensile Test Results	
Stiffness (*lbf/in*)	4754
Yield Load (*lbf*)	65.0
Ultimate Load (*lbf*)	103.2

Specimen Details (B3-020)

Gauge Width, W_g (in)	Orientation, θ (°)	Pre-treatment Temperature, *T (°F)*	Heating Duration, *t* (s)	Cooling Environment	Fracture Location	Type	Process Zone
0.73	90 (weft)	600	200	Room Air	*	*	*

**specimen lost*

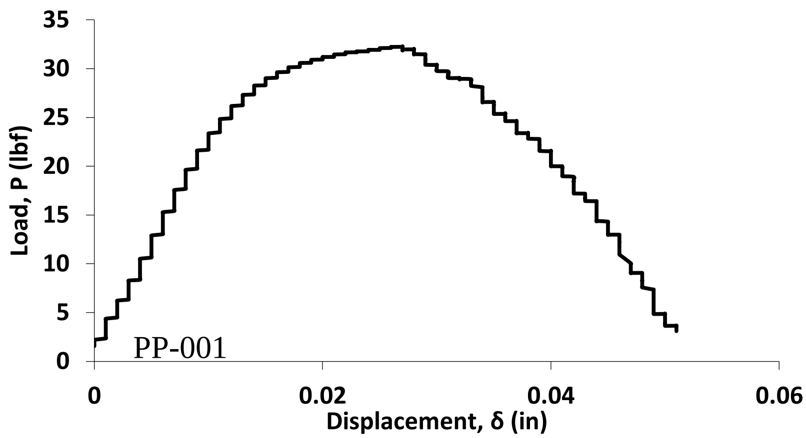

PP-001 Tensile Test Results

Stiffness (*lbf/in*)	1970
Yield Load (*lbf*)	28.3
Ultimate Load (*lbf*)	32.3

Specimen Details (PP-001)

Gauge Width, W_g (in)	Orientation, θ (°)	Pre-treatment Temperature, *T (°F)*	Heating Duration, *t* (s)	Cooling Environment	Fracture Location	Type	Process Zone
0.73	0 (warp)	N/A	N/A	N/A	Inside Gage / At Shoulder	Side, 2 Places	narrow

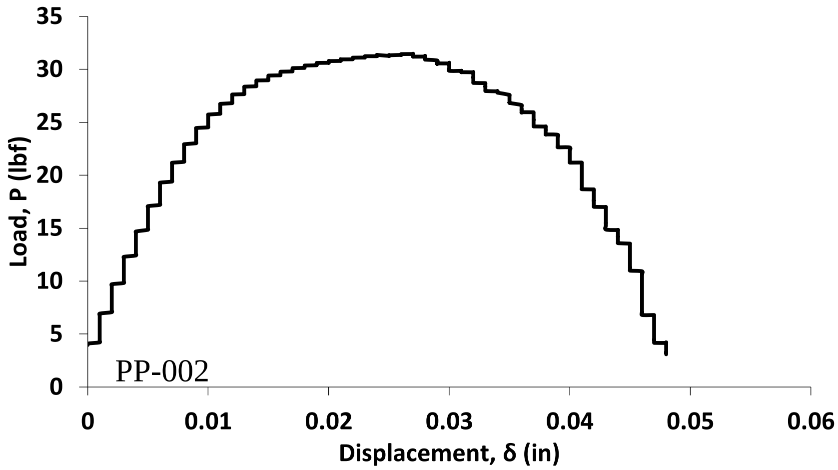

PP-002 Tensile Test Results

Stiffness (*lbf/in*)	1900
Yield Load (*lbf*)	28.3
Ultimate Load (*lbf*)	31.5

Specimen Details (PP-002)

Gauge Width, W_g (in)	Orientation, θ (°)	Pre-treatment Temperature, *T (°F)*	Heating Duration, *t* (s)	Cooling Environment	Fracture Location	Type	Process Zone
0.72	0 (warp)	N/A	N/A	N/A	Inside Gage / At Shoulder	Side, 2 Places	narrow

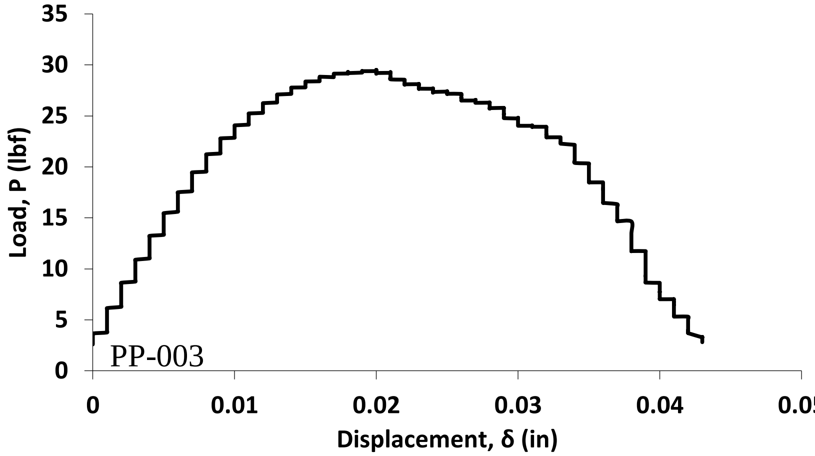

PP-003 Tensile Test Results

Stiffness (*lbf/in*)	1789
Yield Load (*lbf*)	27.7
Ultimate Load (*lbf*)	29.5

Specimen Details (PP-003)

Gauge Width, W_g (in)	Orientation, θ (°)	Pre-treatment Temperature, *T (°F)*	Heating Duration, *t* (s)	Cooling Environment	Fracture Location	Type	Process Zone
0.72	0 (warp)	N/A	N/A	N/A	Inside Gage / At Shoulder	Side, 2 Places	narrow

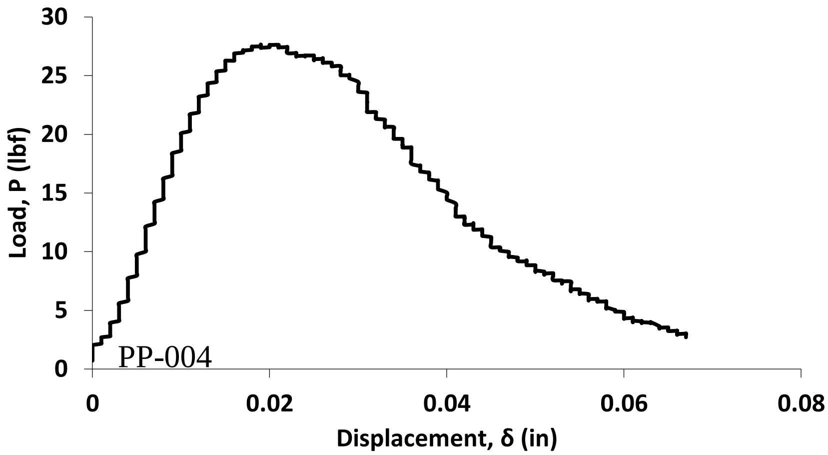

PP-004 Tensile Test Results

Stiffness (*lbf/in*)	1745
Yield Load (*lbf*)	26.9
Ultimate Load (*lbf*)	27.6

Specimen Details (PP-004)

Gauge Width, $\boldsymbol{W_g}$ (in)	Orientation, θ (°)	Pre-treatment Temperature, *T (°F)*	Heating Duration, *t* (s)	Cooling Environment	Fracture Location	Type	Process Zone
0.73	0 (warp)	N/A	N/A	N/A	At Shoulder	Side, 2 Places	narrow

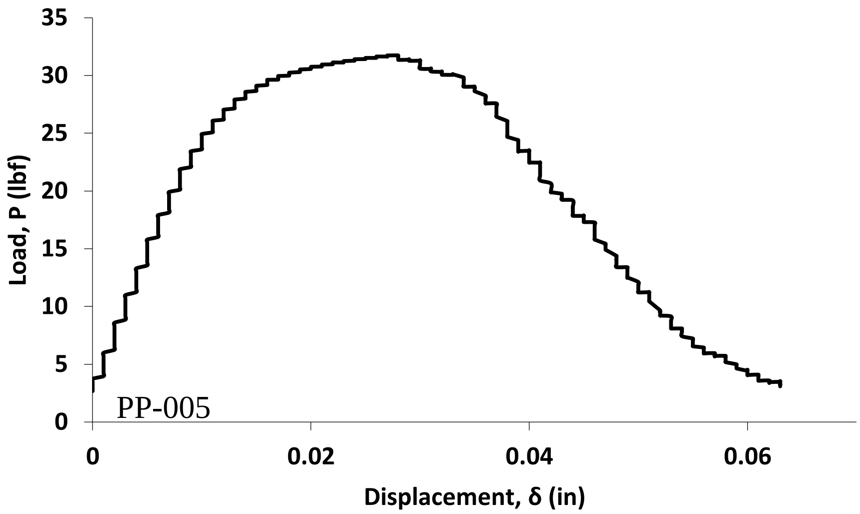

PP-005 Tensile Test Results

Stiffness (*lbf/in*)	1943
Yield Load (*lbf*)	27.9
Ultimate Load (*lbf*)	30.2

Specimen Details (PP-005)

Gauge Width, W_g (in)	Orientation, θ (°)	Pre-treatment Temperature, *T (°F)*	Heating Duration, *t* (s)	Cooling Environment	Fracture Location	Type	Process Zone
0.73	0 (warp)	N/A	N/A	N/A	Inside Gage / At Shoulder	Side, 2 Places	narrow

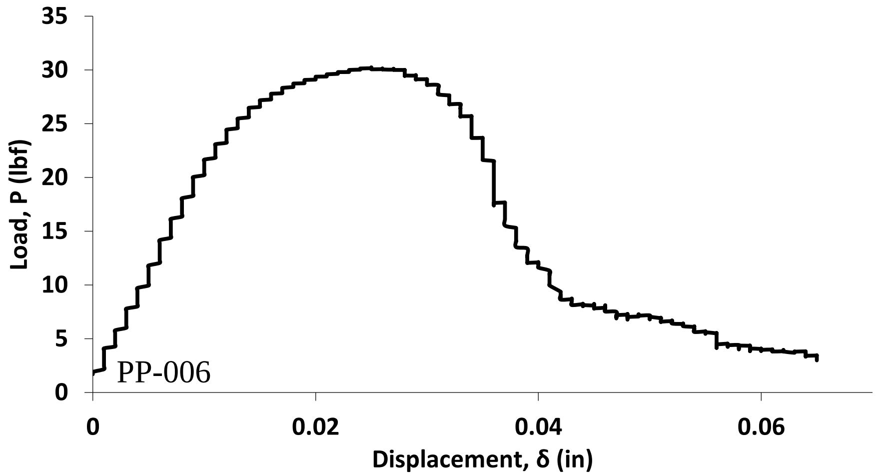

PP-006 Tensile Test Results

Stiffness (*lbf/in*)	1716
Yield Load (*lbf*)	27.8
Ultimate Load (*lbf*)	30.2

Specimen Details (PP-006)

Gauge Width, W_g (in)	Orientation, θ (°)	Pre-treatment Temperature, *T (°F)*	Heating Duration, *t* (s)	Cooling Environment	Fracture Location	Type	Process Zone
0.73	0 (warp)	N/A	N/A	N/A	At Shoulder / Into Grip	Side and Center, 3 Places	wide

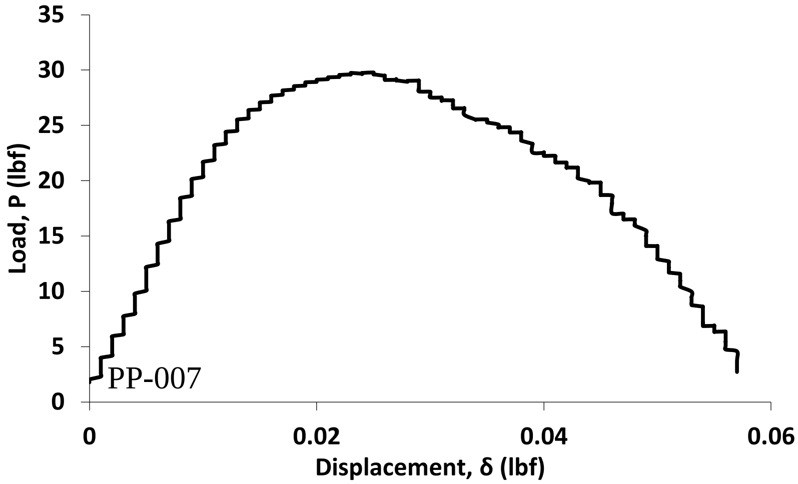

PP-007 Tensile Test Results

Stiffness (*lbf/in*)	1834
Yield Load (*lbf*)	26.4
Ultimate Load (*lbf*)	29.8

Specimen Details (PP-007)

Gauge Width, W_g (in)	Orientation, θ (°)	Pre-treatment Temperature, *T (°F)*	Heating Duration, *t* (s)	Cooling Environment	Fracture Location	Type	Process Zone
0.70	0 (warp)	N/A	N/A	N/A	Inside Gage / At Shoulder	Side, 2 Places	wide

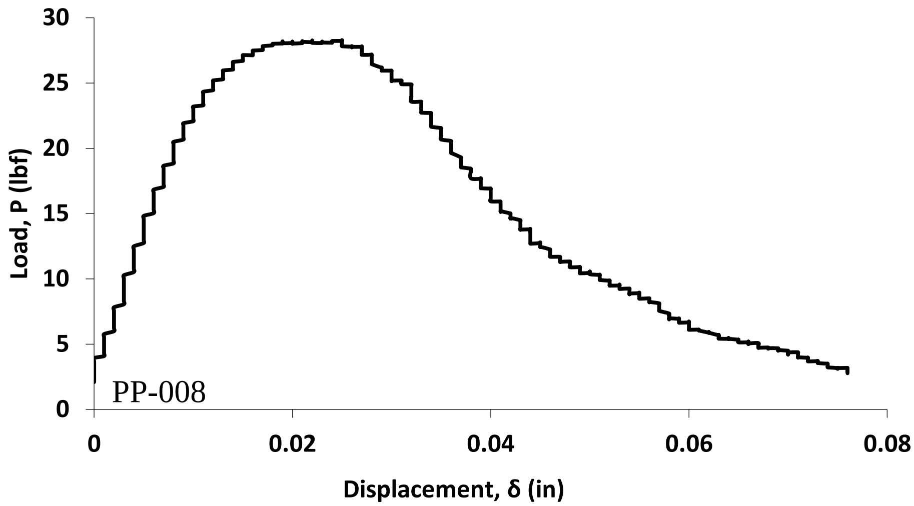

PP-008 Tensile Test Results

Stiffness (*lbf/in*)	1775
Yield Load (*lbf*)	26.2
Ultimate Load (*lbf*)	28.3

Specimen Details (PP-008)

Gauge Width, W_g (in)	Orientation, θ (°)	Pre-treatment Temperature, *T (°F)*	Heating Duration, *t* (s)	Cooling Environment	Fracture Location	Type	Process Zone
0.71	0 (warp)	N/A	N/A	N/A	Inside Gage / At Shoulder	Side and center, 2 Places	narrow

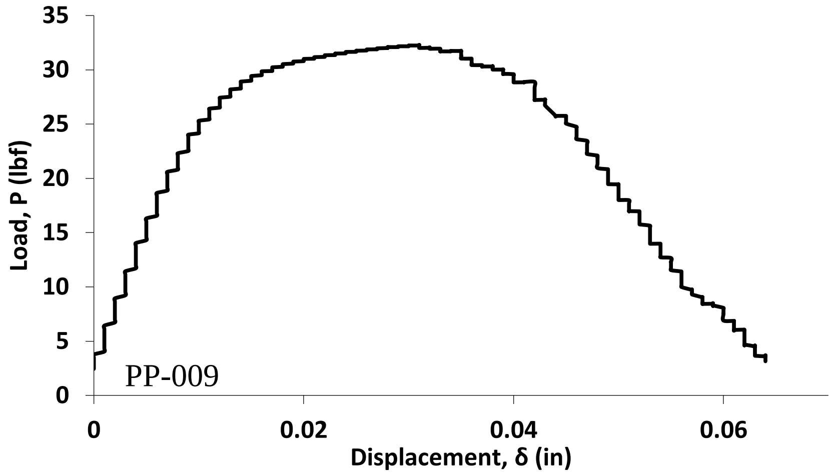

PP-009 Tensile Test Results

Stiffness (*lbf/in*)	1698
Yield Load (*lbf*)	29.8
Ultimate Load (*lbf*)	32.3

Specimen Details (PP-009)

Gauge Width, W_g (in)	Orientation, θ (°)	Pre-treatment Temperature, *T (°F)*	Heating Duration, *t* (s)	Cooling Environment	Fracture Location	Type	Process Zone
0.73	0 (warp)	N/A	N/A	N/A	Inside Gage	Side, 2 Places	wide

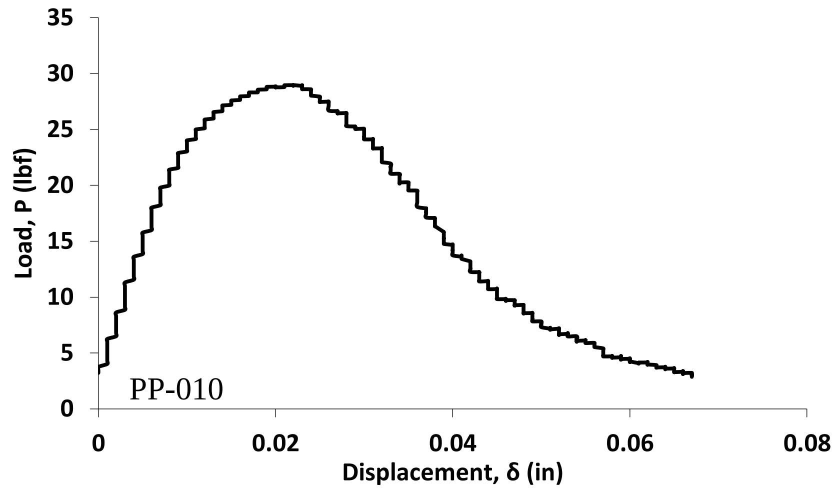

PP-010 Tensile Test Results	
Stiffness (*lbf/in*)	1900
Yield Load (*lbf*)	25.9
Ultimate Load (*lbf*)	29.0

Specimen Details (PP-010)

Gauge Width, W_g (in)	Orientation, θ (°)	Pre-treatment Temperature, *T (°F)*	Heating Duration, *t* (s)	Cooling Environment	Fracture Location	Type	Process Zone
0.70	0 (warp)	N/A	N/A	N/A	At Shoulder	Side, 2 Places	narrow

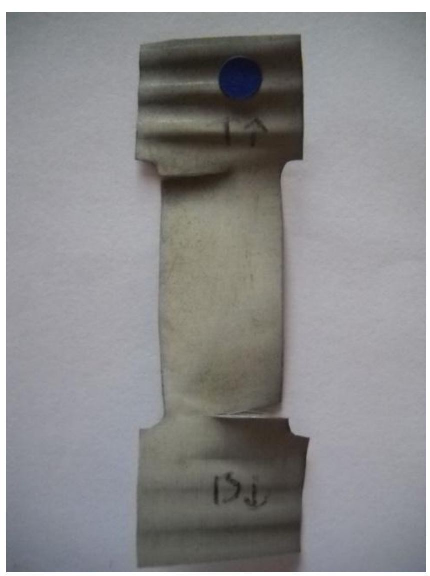

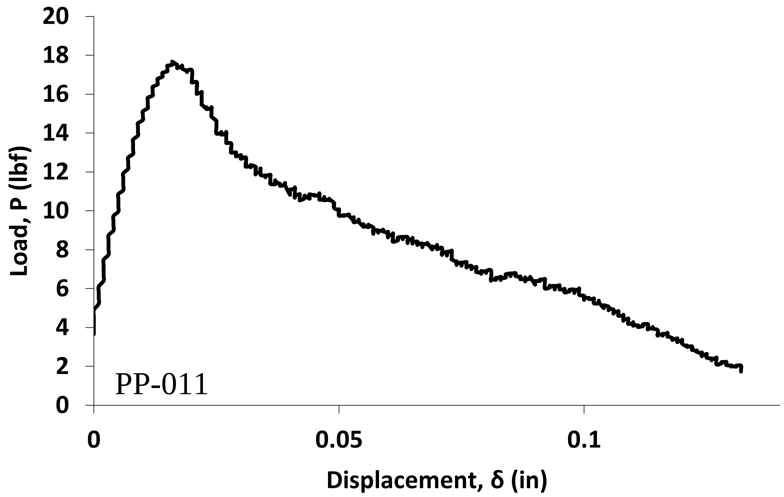

PP-011 Tensile Test Results

Stiffness (*lbf/in*)	1065
Yield Load (*lbf*)	15.1
Ultimate Load (*lbf*)	17.7

Specimen Details (PP-011)

Gauge Width, W_g (in)	Orientation, θ (°)	Pre-treatment Temperature, *T (°F)*	Heating Duration, *t* (s)	Cooling Environment	Fracture Location	Type	Process Zone
0.70	15	N/A	N/A	N/A	At Shoulder	Side, 2 Places	narrow

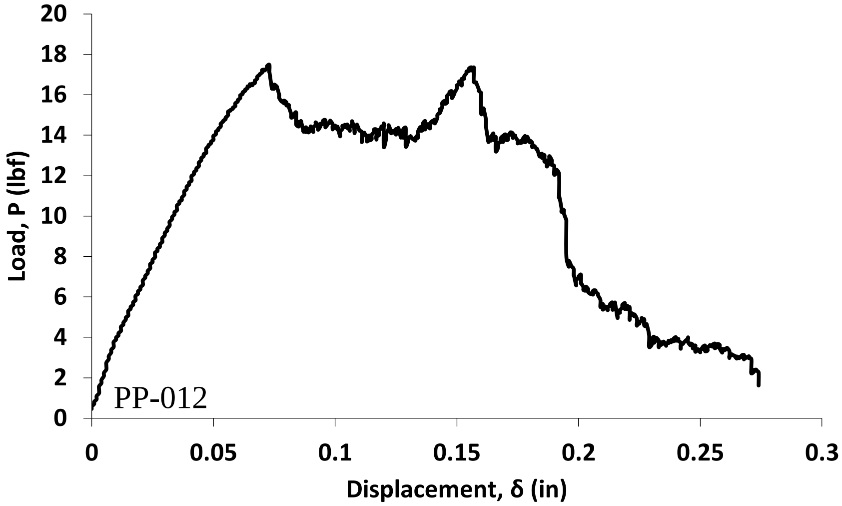

PP-012 Tensile Test Results

Stiffness (*lbf/in*)	257.6
Yield Load (*lbf*)	15.2
Ultimate Load (*lbf*)	17.5

Specimen Details (PP-012)

Gauge Width, W_g (in)	Orientation, θ (°)	Pre-treatment Temperature, *T (°F)*	Heating Duration, *t* (s)	Cooling Environment	Fracture Location	Type	Process Zone
0.71	30	N/A	N/A	N/A	Into Grip	Side, 1 Place	wide

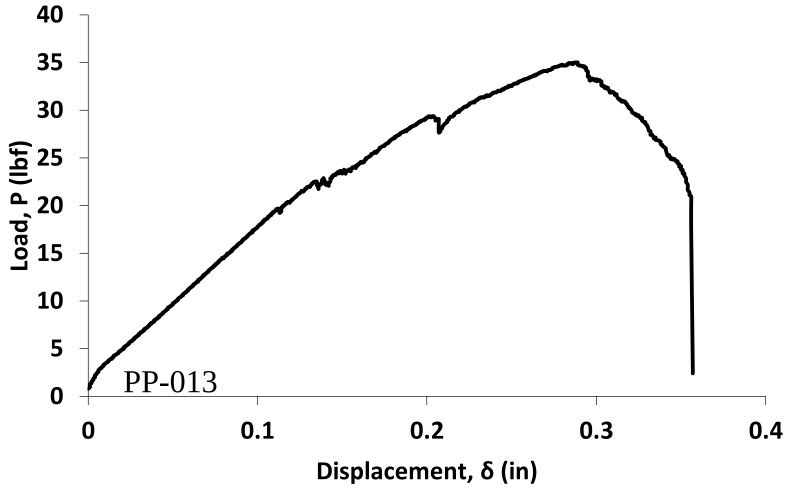

PP-013 Tensile Test Results

Stiffness (*lbf/in*)	189.1
Yield Load (*lbf*)	3.6
Ultimate Load (*lbf*)	35.1

Specimen Details (PP-013)

Gauge Width, W_g (in)	Orientation, θ (°)	Pre-treatment Temperature, *T (°F)*	Heating Duration, *t* (s)	Cooling Environment	Fracture Location	Type	Process Zone
0.73	45	N/A	N/A	N/A	Into Grip	Side, 2 Places	wide

Note Transition of Fracture Orientation

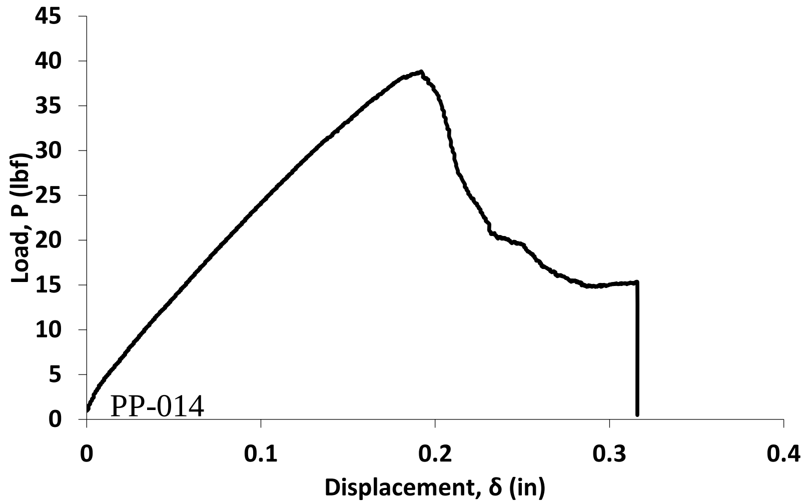

PP-014 Tensile Test Results

Stiffness (*lbf/in*)	213.0
Yield Load (*lbf*)	31.5
Ultimate Load (*lbf*)	38.8

Specimen Details (PP-014)

Gauge Width, W_g (in)	Orientation, θ (°)	Pre-treatment Temperature, *T (°F)*	Heating Duration, *t* (s)	Cooling Environment	Fracture Location	Type	Process Zone
0.70	60	N/A	N/A	N/A	Into Grip	Side, 2 Places	narrow

Note Transition of Fracture Orientation

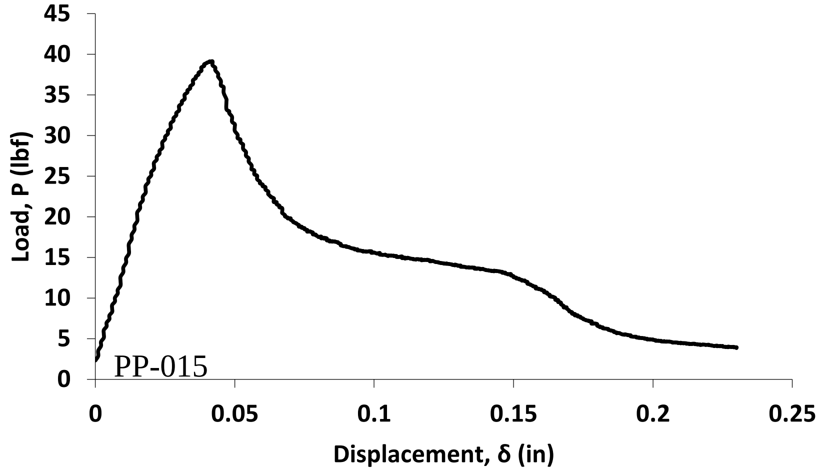

PP-015 Tensile Test Results

Stiffness (*lbf/in*)	1083
Yield Load (*lbf*)	33.4
Ultimate Load (*lbf*)	39.1

Specimen Details (PP-015)

Gauge Width, W_g (in)	Orientation, θ (°)	Pre-treatment Temperature, *T (°F)*	Heating Duration, *t* (s)	Cooling Environment	Fracture Location	Type	Process Zone
0.73	75	N/A	N/A	N/A	At Shoulder / Into Grip	Side, 2 Places	narrow

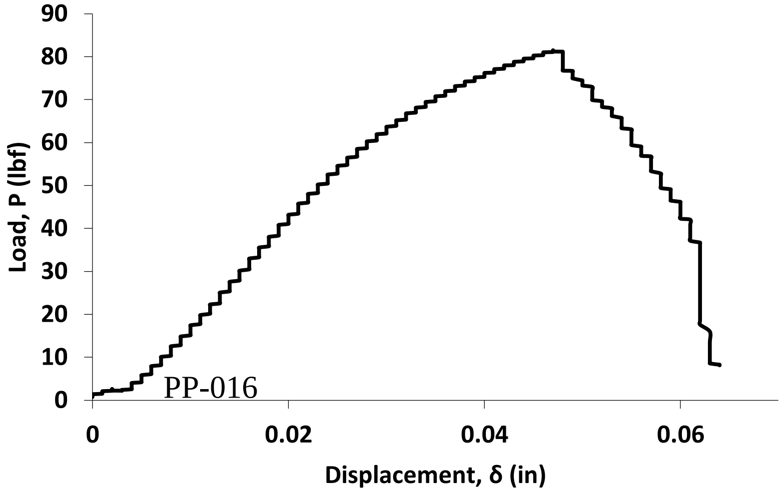

PP-016 Tensile Test Results

Stiffness (*lbf/in*)	2296
Yield Load (*lbf*)	58.7
Ultimate Load (*lbf*)	81.5

Specimen Details (PP-016)

Gauge Width, W_g (in)	Orientation, θ (°)	Pre-treatment Temperature, *T (°F)*	Heating Duration, *t* (s)	Cooling Environment	Fracture Location	Type	Process Zone
0.74	90 (weft)	N/A	N/A	N/A	Inside Gage / At Shoulder	Side, 2 Places	narrow

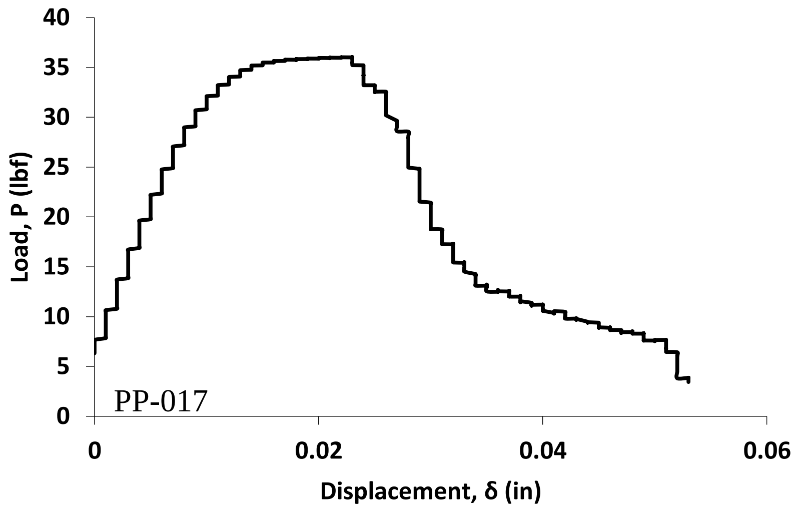

PP-017 Tensile Test Results

Stiffness (*lbf/in*)	2463
Yield Load (*lbf*)	32.6
Ultimate Load (*lbf*)	36.0

Specimen Details (PP-017)

Gauge Width, W_g (in)	Orientation, θ (°)	Pre-treatment Temperature, *T (°F)*	Heating Duration, *t* (s)	Cooling Environment	Fracture Location	Type	Process Zone
0.75	0 (warp)	600	100	Room Air	Inside Gage / At Shoulder	Side and center, 2 Places	narrow

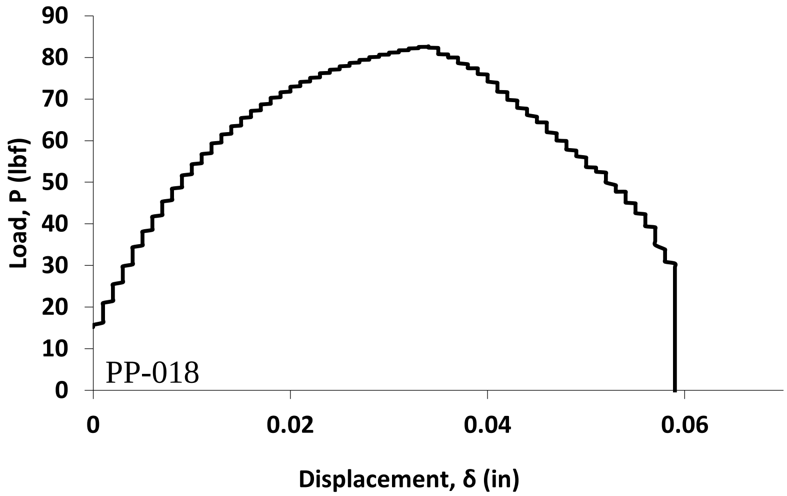

PP-018 Tensile Test Results

Stiffness (*lbf/in*)	3373
Yield Load (*lbf*)	63.6
Ultimate Load (*lbf*)	82.7

Specimen Details (PP-018)

Gauge Width, W_g (in)	Orientation, θ (°)	Pre-treatment Temperature, *T (°F)*	Heating Duration, *t* (s)	Cooling Environment	Fracture Location	Type	Process Zone
0.75	90 (weft)	600	100	Room Air	Inside Gage	Side 1 Place	Narrow - Jagged

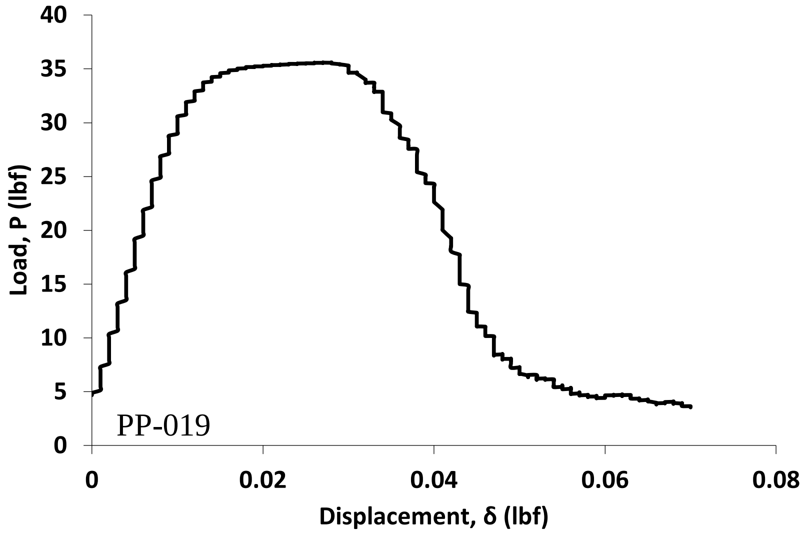

PP-019 Tensile Test Results	
Stiffness (*lbf/in*)	2592
Yield Load (*lbf*)	31.8
Ultimate Load (*lbf*)	35.6

Specimen Details (PP-019)

Gauge Width, W_g (in)	Orientation, θ (°)	Pre-treatment Temperature, *T (°F)*	Heating Duration, *t* (s)	Cooling Environment	Fracture Location	Type	Process Zone
0.75	0 (warp)	600	200	Room Air	Inside Gage / At Shoulder	Side, 2 Place	Narrow

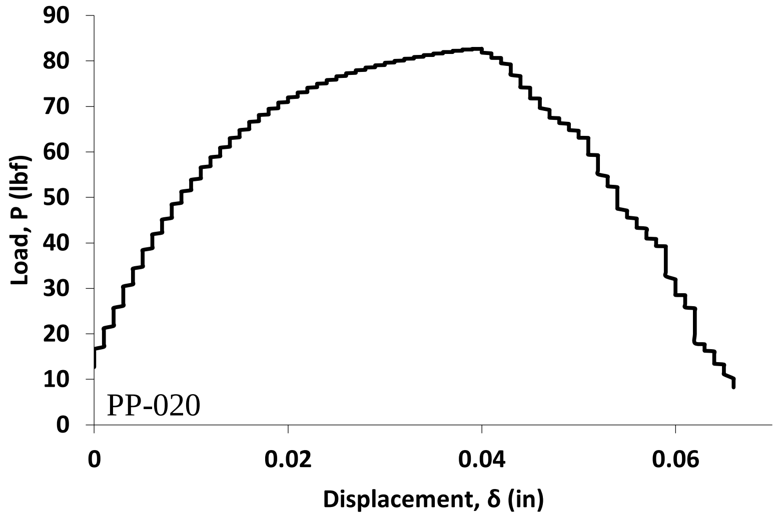

PP-020 Tensile Test Results

Stiffness (*lbf/in*)	3423
Yield Load (*lbf*)	61.8
Ultimate Load (*lbf*)	82.7

Specimen Details (PP-020)

Gauge Width, W_g (in)	Orientation, θ (°)	Pre-treatment Temperature, *T (°F)*	Heating Duration, *t* (s)	Cooling Environment	Fracture Location	Type	Process Zone
0.72	90 (weft)	600	200	Room Air	Inside Gage	Side, 1 Place	Narrow

References

[1] King, M., Jearanaisilawong, P., and Socrate, S., “A Continuum Constitutive Model for the Mechanical Behavior of Woven Fabrics,” *International Journal of Solids and Structures.* Vol. 42, pp. 3867-3896, 2005.

[2] Hamila, N., Boisse, P., Sabourin, F., and Brunet M., “A Semi-discrete Shell Finite Element for Textile Composite Reinforcement Simulation,” *International Journal for Numerical Methods in Engineering*. Vol. 79, No. 12, pp. 1443-1466, 2009.

[3] Cavallaro, P., Sadegh, A., and Quigley, C., “Decrimping Behavior of Uncoated Plain-woven Fabrics Subjected to Combined Biaxial Tension and Shear Stresses,” *Textile Research Journal.* Vol. 77, No. 6, pp. 404-416, 2007.

[4] Tarfaoui, M., and Drean, J. Y., “Predicting the Stress-Strain Behavior of Woven Fabrics Using the Finite Element Method,” *Textile Research Journal.* Vol. 71, No. 9, pp. 790-795, 2001.

[5] Nicolleto, G., and Riva, E., “Failure Mechanisms in Twill-weave Laminates: FEM Predictions vs. Experiments.” *Composites Part: A.* Vol. 35, pp. 787-795, 2004.

[6] Barbero E.J., Trovillion, J., Mayugo, J.A., and Sikkil, K.K., “Finite Element Modeling of Plain Weave Fabrics from Photomicrograph Measurements,” *Composite Structures.* Vol. 73, pp. 41-52, 2006.

[7] Pierce, F.T., “The Geometry of Cloth Structure,” *Journal of the Textile Institute.* Vol. 28, pp. 45-96, 1936.

[8] Kawabata, S., Niwa, M., and Kawai, H., “The Finite Deformation Theories of Plain Weave Fabric, Part 1: The Biaxial-deformation Theory,” *Journal of the Textile Institute.* Vol. 64, pp. 21-46, 1964.

[9] Sun, F., Seyam, A., and Gupta, B., “A Generalized Model for Predicting Load-Extension Properties of Woven Fabrics,” *Textile Research Journal.* Vol. 67, No. 12, pp. 866-874, 1997.

[10] Kumazawa, H., Susuki, I., Morita, and Kuwabara, T., “Mechanical Properties of Coated Plain Weave Fabrics Under Biaxial Loads,” *Transactions of the Japan Society for Aeronautical and Space Sciences.* Vol. 48, No. 160, pp. 117-123, 2005.

[11] Zheng, J., Takatera, M., Inui, S., and Shimizu, Y., “Measuring Technology of the Anisotropic Tensile Properties of Woven Fabrics,” *Textile Research Journal.* Vol. 78, No. 12, pp. 1116-1123, 2008.

[12] Voce, E., “True Stress-Strain Curves and Their Application to Cold-Working Processes,” *Metal Treatment*, Vol. 15. No. 54, pp. 53-66, 1948.

[13] Antoun, B.R., and Song, B., “Interaction of Hydrogen and Deformation in 316L Stainless Steel,” *Proceedings of the SEM Annual Conference*, 2009.

[14] Gibson, R.F., 2007. *Principles of Composite Material Mechanics*, CRC Press, Boca Raton. pp. 47-81.

[15] Pagano, N.J., and Halpin, J.C., “Influence of End Constraint in the Testing of Anisotropic Bodies” *Journal of Composite Materials*, Vol. 2, pp. 18-31, 1968.

[16] Jones, R.M., 1975. *Mechanics of Composite Materials.* Hemisphere Publishing Co., New York.

[17] Hill, R., 1956. *The Mathematical Theory of Plasticity*, Oxford University Press, London. pp. 318-325.

[18] Liu, P., He, G., and Wu, L., “Structure Deformation and Failure of Sintered Steel Wire Mesh Under Torsion Loading” *Materials and Design*, Vol. 30, pp. 2264-2268, 2009.